Chemical Bonding at Surface and Interface Studied by X-ray Absorption Fine Structure

（表面、界面における化学結合のXAFSによる研究）

木口学

Acknowledgements

The present study has been carried out under the supervision of Professor Toshiaki Ohta (the University of Tokyo). I would like to express my sincere gratitude to his valuable suggestions and supports.

I would like to thank Dr. Toshihiko Yokoyama (the University of Tokyo) for his helpful discussions, suggestions and continual encouragement. Without his special supports, I could not have accomplished the present work.

I wish to express my gratitude to Professor Koichiro Saiki for his valuable suggestions and generous support.

I am deeply grateful to Mr. Yoshinori Kitajima (Photon Factory in Institute of Materials Structure Science, High Energy Accelerator Research Organization) for his fruitful discussions and collaborations.

I am deeply grateful to Professor Haruo Kuroda (The Science University of Tokyo) for his valuable suggestions and helpful discussion for the study of the Cl/Cu(100) system.

Most of these works have been performed at Photon Factory in Institute of Materials Structure Science, High Energy Accelerator Research Organization, under the approval of the Photon Factory Program Advisory Committee (PF-PAC Nos. 95G379, 97G315, 98G101 and 98G314). I thank all the in-house staff of Photon Factory, too.

Many thanks go to all members of Ohta Laboratory (the University of Tokyo), especially Dr. Hiroshi Kondoh, Dr. Shigeru Terada, Mr. Mitsuru Sakano, Mr. Yuuichi Okamoto, Mr. Takehisa Tsuduki, Mr. Osamu Endo, Mr. Kenji Kohdate, and Mr. Daiju Matsumura.

Finally, many thanks to my family for never-ending support and encouragement.

Contents

1 General introduction

1-1 Surface and interface

An interface is a field where two different materials are in contact with each other. Unexpected phenomena are sometimes observed, different from uniform systems. Furthermore the interface plays an important role to transfer and/or exchange particles, energy and electrons between two materials. Many chemists, physicists, as well as biologists have studied the interface extensively, and the fields related to the interface have been widespread, in solid state physics, electrical chemistry, catalysis, electronics, and so on.

There are several kinds of interfaces, such as solid-liquid, solid-gas, solid-solid interfaces. One typical example of the liquid-solid interface is an electrode. Electrode reactions and the structures of electronic double layer are still at hot issue. The solid-liquid interface is also important in industry as the phenomena, such as washing, jointing, dyeing, lubrication. Gas adsorption and catalytic reactions are main topics for the gas-solid interface. When a molecule adsorbs on a metal or a metal oxide surface, it often dissociates into atoms or ionic species. The adsorbed molecule is thus very reactive, and various chemical reactions can occur easily. It is clear that the reaction at the gas-solid interface is important and specific to the interface. One of the typical examples is the Haber-Bosch's reaction (the ammonia synthesis reaction). Furthermore, fruits of the investigation of the gas-solid interface are applied to gas sensors. The solid-solid interface is the most advanced field and the current topic. The variety and utility of the solid-solid interface is apparent, because it plays an important role in electronic devices like amplifiers and rectifiers.

A surface can also be regarded as an interface between vacuum and a solid. Therefore many specific and interesting phenomena can be observed on the surface, such as surface plasmon, surface polariton, two-dimensional ordering, surface melting.

As described in the above, we have shown the various properties specific to the

surface and interface, and shown that the results are applied in many fields. For further understanding of such unexpected phenomena at the surface and interface, it is necessary to study the chemical bonding. With regard to the solid-solid interface, the chemical bonds are in the different surroundings from those of bulk, because one material contacts with the other material which has a different lattice constant and even different crystal structure. Surface bonds are also affected by the reduction of the coordination number to one-half its bulk value. It is thus important to make clear the change in the chemical bond in such a special environment for not only the understanding of the interface specific phenomena but also the general understanding of chemical bonding.

In the following, we discuss the change in chemical bonding at the surface and interface by comparing with the chemical bonds in the bulk.

1-2 Chemical bonding at the interface

In order to study the chemical bonding at the interface, it is important to fabricate well-defined flat films. The growth mode of a thin film is classified into three modes; the layer-by-layer mode, the layer growth and nucleation mode, and the three-dimensional island growth mode. Here, we consider the ideal layer-by-layer growth and the structure of the film in the following.

First, the interface structures of Fe, Cu, Ni/Cu(100) are discussed as typical examples of metal-metal bonds at the interface. The crystal structures of Fe, Co, and Ni are bcc, hcp, and fcc, respectively. They are ferromagnetic materials and these systems are of particular interest in relation to the giant magnetic resistance [1-4]. Quantitative low energy electron diffraction (LEED) measurements have revealed that these metals grow on Cu(100) surface in the layer-by-layer mode. In Fe/Cu(100), S. Müller *et al.* [5, 6] have revealed that the initial five layers have distorted fcc structures, next five layers have fcc structures, and the further thick film has a bcc structure. The distance of the Fe-Fe bond at the interface is the same as that of the Cu-Cu bond. In Co/Cu(100), initial 10 layers were determined to have fcc structure by the EXAFS analysis [7, 8]. These results indicate that the metal-metal bond connects with the substrate by changing its crystal

structure. Müller *et al.* have done a detailed structural analysis of the hetero junction of Ni and Cu, which have a same crystal structure, and found that the lattice constant of the first Ni layer is equal to that of the Cu(100) surface [9-12]. These facts indicate that the metal bond is soft, and the structure and the lattice constant of the first layer are the same as those of the substrate.

The interface structure of semiconductors has a typical covalent bonding. In a semiconductor, the lattice matching condition is very strict, and the layer-by-layer growth is not observed for the materials which have different crystal structures or lattice constants. As the limited combination, the structure of the AlAs/GaAs interface has been studied [13-16], where both materials have the same zinc blende structure and the same lattice constant. Ichinose *et al.* [14] observed the interface of (100) and (110) oriented films by transmission electron microscope (TEM), and found that the interface is steep and the inter-diffusion does not occur. The strict lattice matching condition of semiconductors means that the covalent bond is so strong that it tends to retain its original bond structure regardless of the change of surroundings.

The interface structures of ionic materials are discussed for hetero interfaces of alkali halides because the chemical bonding of alkali halide is almost ionic. The ionic bond is much softer than the other bonds, since it is based on a coulomb interaction. The alkali halide films thus grow in a layer-by-layer mode even for the case of large lattice mismatching; furthermore CsCl is known to grow on foreign alkali halide by changing its structure from the CsCl structure to the rocksalt structure [17]. Unfortunately a quantitative LEED analysis has not been done for alkali halide thin films because of the substrate charging, though the crystal structure and growth mode have been studied by x-ray diffraction (XRD) and reflection high-energy electron diffraction (RHEED). Saiki *et al.* [18, 19] studied various hetero epitaxial alkali halide thin films by RHEED. They found that the growth mode can be classified to three types, I, II, and III, where the type I, II and III denote the systems for the mismatch smaller than about 10 %, 10-20 %, and larger than 20 %, respectively. In the type I, the two-dimensional layer-by-layer growth occurs and the lattice constant of the film exhibits a gradual change with the film

thickness, that is, the film and substrate are bonded coherently at the interface. In type II, two-dimensional layer growth occurs, and the lattice constant of the film is almost the same as that of the bulk crystal. In the case of type III, three-dimensional island growth occurs. Recently Natori *et al.* [20] studied the KCl/KBr(100) interface (type I) by computer simulations to reveal that the coherent bonding is formed at the interface, being consistent with the Saiki's results [18, 19]. The above results indicate that the coherent bonding is formed at the interface of ionic materials regardless of the difference in the crystal structure and/or the lattice constant.

1-3 Chemical bonding at the surface

At the surface of an ionic compound, ionic bonds are extended to the surface normal direction due to the loss of upper ions, while it is stabilized by electrostatic forces of positively or negatively charged ions situated at the upper and lower sites. Since positively charged ions (smaller ionic radius and polarization) are more mobile than negatively charged ions, surface ions are no longer on the same plane and the surface is rumpled.

On a semiconductor surface, a chemical bond undergoes a drastic change, including the recombination of chemical bonds, due to the appearance of dangling bonds on the surface. Because dangling bonds are so unstable that each two of them ties together to form dimers in many cases and a peculiar surface structure appears. For example, 2×1 [21] and 7×7 [22, 23] structures are formed on Si(100) and Si(111) surfaces, respectively.

In case of the metal bonding at a surface, we can discuss not only the structures but also the thermal properties such as interatomic potential. This is because many experimental methods can be applied to the metal surfaces and the surface structures are simpler than those of other materials.

In order to discuss the metal bonding at the surface, the results of metal small clusters are of great value for reference, because a ratio of a surface vs. bulk is larger for smaller clusters. G. Apai *et al.* [24] studied the Cu, Ni clusters deposited on a carbon

sheet by extended x-ray absorption fine structure (EXAFS). They found that the interatomic bond distance decreases by as large as 9 %, in proportion to the inverse of the particle size, that is, surface ratio (surface/volume). Furthermore, they considered that at the surface the number of nearest-neighbor atoms is significantly less than that in the bulk, which leads to a contraction of the bond distance due to the reduction in repulsive interactions between nonbonded electron pairs. This bond contraction corresponds to the surface relaxation which is often observed for single crystal metal surfaces. Montano *et al.* [25, 26] studied the structures of Cu clusters (7 to 10 Å mean diameter) in a solid Ar matrix to prevent interference of a strongly interacting substrate. They showed that the crystallographic structure of the cluster is consistent with a fcc lattice and the Cu-Cu bond distance decreases by 13 % in the dimer.

Thermal vibrations and thermal expansions at the metal surfaces have also been studied. Harada *et al.* [27] found that thermal vibration of Au particles increases monotonously with the decrease in particle size from the analysis of the Debye-Scherrer lines of the particles deposited on a glass substrate. The particle size dependence of thermal vibration can be explained by introducing two components on the assumption that the particles are composed of a core and a shell with one atomic layer thickness. A. Balerna *et al.* [28, 29] studied thermal vibration of Au clusters by means of temperature dependent EXAFS. They determined the Debye temperatures of clusters using the correlated Debye model to find the decrease in Debye temperature with decreasing in the cluster diameter. It should keep in mind that Harada *et al.* [27] discussed thermal vibration of metal atoms by diffraction, while Balerna *et al.* [29] discussed thermal vibration of metal bonds by EXAFS. Yokoyama *et al.* [30] measured temperature dependence EXAFS spectra of SiO_2 supported Ag, Pd metal clusters to study anharmonic vibration of metal bonds. They found that the thermal expansion coefficient of the cluster is seven times as large as those of the bulk metals, in other words, the effective interatomic potential of surface metal-metal bonds is shallower and more anharmonic.

Since information on anisotropy of chemical bonding cannot directly be obtained

from small clusters, studies concerning single crystals are still essential. The LEED experiments [31, 32] have clarified significant anisotropy between surface normal and parallel directions. Surface melting is also predicted by the Lindemann empirical theory (The melting transition occurs when the amplitude of thermal vibration is as large as 10-20 % of the lattice constant). J. F. Van der Veen *et al.* [33-35] studied the surface melting on Pb(110) and Al(110) surfaces by using MEIS (Medium energy Ion Scattering) and found that surface melting point of Pb(110) is approximately 40 K lower than the bulk melting point.

1-4 Scope of this thesis

It was revealed that the chemical bonding at the surface and interface is different from that in the bulk by demonstrating many examples in the above sections. In my doctoral works, the difference of the chemical bonding between in the bulk and at the surface or interface has been especially focussed. Thus, I have studied the chemical bonding at the interface of alkali halide hetero-epitaxial thin films and the chemical bonding at the surface of metal thin films by using the EXAFS spectroscopy. Furthermore, I have studied the surface chemical bonding in the adsorbate-substrate systems.

For metal and covalent bonds, it is evident that two materials have the same structure and same lattice constant at the interface. The ionic bonds are also assumed to have same structure and lattice constant at the interface. However it has not been clear that the coherent bond is really formed at the interface for the system mismatched by as large as 10 %. The XAFS method enables us to examine the chemical bonds at alkali halide hetero-epitaxial thin films directly. By studying the interface structures for a largely mismatched interface, it might be possible to find new phenomena which have not been observed so far, because of the enhancement of the difference.

Many examples also indicate that chemical bonds are softer and the interatomic potential of a metal bond is more anharmonic than that in the bulk. For further understanding of the surface bond at the surface, it is necessary to discuss the anisotropy

of the interatomic potential quantitatively. I have thus tried to determine the structures and the interatomic potentials of in-plane and out-of-plane bonds separately for metal thin films grown epitaxially on highly oriented pyrolytic graphite (HOPG) by using the polarization dependent XAFS.

Many experimental methods have been applied to study the properties at the surface and interfaces. For structural analysis, XRD, LEED, RHEED and TEM are appropriate. XPS, AES, EELS and UPS are useful for studying the electronic structures, while FMR, XMCD, SMOKE are applied to study the surface magnetism, and HREELS and IR are used to study surface vibrations. The best method is dependent on the system and the purpose. I have used EXAFS for the present purpose to study the chemical bond itself. Because EXAFS functions as a search light shining a specific chemical bond and it provides information on the interatomic distance, coordination numbers, species of surrounding atoms and interatomic potentials at the same time; furthermore the anisotropy can be studied by using polarized x-rays. These properties originate from the fundamental phenomena of EXAFS. That is, EXAFS is produced by the interference of photoelectrons ejected from the x-ray absorbing atoms and photoelectrons that are back-scattered by the surrounding atoms.

The present thesis is organized in the following manner. Chapter 2 deals with the theory of EXAFS and the EXAFS measurements including a newly constructed system. Chapter 3 and 4 deal with the interface structures of alkali halide hetero-epitaxial films of KCl, NaCl/KBr, NaBr. Though the in-plane bond distances of the films are varied at the interface, they are rather close to the bulk bond distances. This contradicts with the previous model of coherent bonding at the interface. Such a discrepancy implies that the short-range order (bond distance) does not always reflect the long-range order (lattice constant). Chapter 6 deals with the thermal vibrations of metal thin films by means of temperature dependent EXAFS. Surface bonds were found to be much softer and anharmonic especially for the surface normal direction than those of the corresponding bulk metals. Chapter 7 and 8 deal with the surface chemical bonds on adsorbate-substrate systems. Anisotropic vibrations are discussed for S, Cl/Ni(100) systems by

using the molecular dynamics simulations in Chapter 7. Chapter 8 deals with the coverage dependence of surface Cl-Cu bonds in Cl/Cu(100) comparing with the Cl/Ni(100). The experimental results demonstrate that the Cl-Cu bond is tightened with the increase of the Cl coverage, while the Cl-Ni bond is softened with the Cl coverage. This different coverage dependence is discussed by using density-functional calculations.

References

[1] D. L, M. Freitag, J. Pearson, Z. Q. Qui and S. D. Bader, Phys. Rev. Lett. **72**, 3112 (1994).

[2] R Allenspach and A. Bischof, Phys. Rev. Lett. **69**, 3385 (1992).

[3] J. Thomassen, F. May, B. Feldmann, M. Wuttig and H. Ibach, Phys. Rev. Lett. **60**, 3831 (1992).

[4] M. Zharnikov, A. Dittschar, W. Kuch, M. Schneider, and J. Kirschner, Phys. Rev. Lett. **76**, 4620 (1996).

[5] S. Müller, P. Bayer, C. Reischl, K. Heinz, B. Feldmann, H. Zillgen and M. Wuttig, Phys. Rev. Lett. **74**, 765 (1995).

[6] K. Heinz, P. Bayer, and S. Muller, Surf. Rev. and Lett. **2**, 89 (1995).

[7] A. Clarke, G. Jennings, R. F. Willis, P. J. Rous and J. B. Pendry, Surf. Sci. **187**, 327 (1987).

[8] P. L. Ferve, H. Magnan, and D. Chandesris, Surf. Sci. **352-354**, 923 (1996).

[9] S. Müller, A. Kinne, M. Kottscke, R. Metzler, P. Bayer, L. Hammer and K. Heinz, Phys. Rev. Lett. **75**, 2859 (1995).

[10] N. Schultz and K. Baberschke, Phys. Rev. B **50**, 13467 (1994).

[11] S. Müller, B. Schulz, G. Koska, M. Farle, K. Heinz, and K. Beberschke, Surf. Sci. **364**, 235 (1996).

[12] B. Schirmer and M. Wuttig, Surf. Sci. **399**, 70 (1998).

[13] A. Ourmazd, D. W. Taylar and J. Cunninghand and C. W. Tu, Phys. Rev. Lett. **62**, 933 (1989).

[14] H. Ichinose, Y. Ishida, T. Furuta and H. Sasaki, J. Electron Microsc. **36**, 82 (1987).

[15] P. M. Petoff, A. C. Gossard, W. Wiegman and A. Savage, J Crys. Growth, **44**, 5 (1978).

[16] C. J. D. Hetherington, J. Barry, J. M. Bni, C. J. Humphreys, J. Grange and C. Wood, Mete, Res. Soc. Symp. Proc. **37**, 41 (1985).

[17] H. Dabringhaus and M. Haag, Surf. Sci. **268**, 351 (1992).

[18] K. Saiki, Y. Nakamura and A. Koma, Surf. Sci. **250**, 27 (1991).

[19] K. Saiki, Appl. Surf. Sci. **113/114**, 9 (1997).

[20] A. Natori, A. Tanaka and H. Yasunaga, Thin Sol. Films **281/282**, 39 (1996).

[21] R. J. Hamers. R. M. Thomp. D. E. Demuth, Phys. Rev. B **34**, 5343 (1983).

[22] K. Takayanagi and S. Nakatani, Surf. Sci. **164**, 367 (1985).

[23] G. Binnig. H. Rohrer, C. Gerber and E. Weidel, Phys. Rev. **50**, 120 (1983).

[24] G. Apai, J. F. Hamilton, J. Stöhr and A. Thompson, Phys. Rev. Lett. **43**, 165 (1979).

[25] P. A. Montano, G. K. Shenoy, E. E. Alp, W. Schulze and J. Urban, Phys. Rev. Lett. **56**, 2076 (1986).

[26] P. A. Montano and G. K. Shenoy, Sol. Sta. Com. **35**, 53 (1980).

[27] J. Harada and K. Ohshima, Surf. Sci. **106**, 51 (1981).

[28] A. Balerna, E. Bernieri, P. Picozzi, A. Reale, S. Santucci, E. Burattini and S. Mobilio, Phys. Rev. B **31**, 5058 (1985).

[29] A. Balerna and S. Mobilio, Phys. Rev. B **34**, 2293 (1986).

[30] T. Yokoyama and T. Ohta, Jpn. J. Appl. Phys. **29**, 2052 (1990).

[31] A. U. MacRae, Surf. Sci. **2**, 52 (1964).

[32] K. Pohl, J. H. Cho, K. Terakura, M. Schefler and E. W. Plummer, Phys. Rev. Lett. **80**, 2853 (1998).

[33] W. M. Frenken, and J. F. Van der Veen, Phys. Rev. Lett. **54**, 134 (1984).

[34] B. Pluis, A. W. Denier van der Gon, J. W. M. Frenken, and a. J. F. van der Veen, Phys. Rev. Lett. **59**, 2678 (1987).

[35] A. W. Denier van der Gon, D. J. O'connor and J. F. Van der Veen, Surf. Sci. **227**, 143 (1990).

2 X-ray absorption fine structure

2-1 EXAFS theory [1-6]

2-1-1 Fundamental EXAFS equation

In this section the fundamental EXAFS equation is deviated in semiclassically. Consider the evolution of the system under the Hamiltonian

$$H = \frac{1}{2m}\{p - (e/c)A\}^2 \qquad (1.1)$$

here ***p***, ***m***, ***A*** is the momentum and the mass of electron, and the vector potential, respectively. In x-ray absorption, only the first term of ***A*** comes into operation (one photon approximation); the second term only enters into higher-order processes such as x-ray scattering. The Hamiltonian can thus be separated into two basic parts.

$$H = H_0 + H_1 \qquad (1.2)$$

$$H_0 = -\frac{p^2}{2m} \qquad (1.3)$$

$$H_1 = -\frac{e}{mc}A \cdot p \qquad (1.4)$$

where H_0 describes the system in the absence of any applied radiation fields, while the Hamiltonian H_1 is the electron-photon interaction. We can evaluate the transition rate ***W*** of the electron excitation caused by this interaction within first-order perturbation theory, because H_1 is very small.

$$W = \frac{2\pi}{\hbar}\left|\langle i|H_1|f\rangle\right|^2 \delta(E_f - E_i) \qquad (1.5)$$

The eq. (1.5) means that a core electron ($E_i = E_c$) is excited to the final state (E_f) by absorbing a photon ($h\nu$). Here we use the independent electron approximation, that is, the final state includes a excited electron located at the continuum state (E_k) and the other electrons located at the same ground state as the initial state. The E_f and E_i thus become

$$E_i = -E_c + \hbar\omega, \quad E_f = E_k \qquad (1.6)$$

Here we consider the photon with polarization λ and wave vector q

$$A = A_q \varepsilon_q(\lambda)\exp(iqr) \quad (1.7)$$

where $\varepsilon_q(\lambda)$ is the unit vector in the r direction. The relation between a photon flux $I(\omega)$ and A_q is

$$|A_q|^2 = (2\pi c/\omega^2) I(\omega) d\omega \quad (1.8)$$

Thus, the probability that an electron is excited to the final state is obtained by ω integral.

$$W = \frac{4\pi^2 e^2}{\hbar^2 c m^2 \omega^2} I(\omega) \left| \langle i | \exp(iqr)\varepsilon_q(\lambda) p | f \rangle \right|^2 \qquad E_f + E_c - \hbar\omega = 0 \quad (1.9)$$

Because $i>$ is the wave function of core electron at the ground state, it spreads as large as the wave function of the core electron. Thus the approximation exp(iqr)=1 is fairly good one (dipole approximation), when the energy of photoelectron is larger than 50 eV (qr<<1). The dipole approximation is assumed where the electric field of the electromagnetic wave assumed to be constant over the dimension of the core electron. Therefore W is given by,

$$W = \frac{4\pi^2 e^2}{\hbar^2 c} I(\omega) \left| \langle i | er | f \rangle \right|^2 \qquad E_f + E_c - \hbar\omega = 0 \quad (1.10)$$

In obtaining eq (1.10) we used the relation $[r, H_0] = (i\hbar/m)p$.

In order to deviate the EXAFS equation, it is necessary to calculate the matrix element (1.10). Here we consider the excitation of K shell of an atom. In such a case, the dipole selection rule of Δl=1 permits only a single final state of l=1 with p symmetry. This final state is generally written with T matrix.

$$f >= k > + G_0^- T^- |k > \quad (1.11)$$

$$T^- = \sum t_u + \sum t_u G_0^- t_v + \cdots \quad (1.12)$$

In eq. (1.11), the first term means the incident wave and the second term means the scattered wave. This represent is valid only if the interatomic distance is much larger than the range where the atomic potential is effective. Here A is supposed the x-ray-

absorbing atom and B is the scattered atom. The main term of eq. (1.10) is given

$$\langle f|er|i\rangle = \{\langle k| + \langle k|t_B^+ G_o^+ + \langle k|t_A^+ G_o^+ t_B^+ G_o^+ \}\varepsilon r|i\rangle \qquad (1.13)$$

here G_0^+ is the out-going Green function. The first term means to the process that an electron is ejected from the x-ray-absorbing atom and the second and third terms mean the single and double scattering process. The first term of eq. (1.13) can be rewritten by using spherical harmonics.

$$\begin{aligned}\langle k|\varepsilon r|i\rangle &= (16\pi^2/3)\sum(-i)^l Y_1^m(\varepsilon)Y_l^m(k)\int d\Omega Y_l^m(\Omega)Y_1^m(\Omega)\int drr^3 j_l(kr)\phi_A \\ &= (\varepsilon k)M\end{aligned} \qquad (1.14)$$

here $M = -i(4\pi)\int drr^3 j_1(kr)\phi_A(r)$ (1.15)

and j is a spherical Bessel function. The second term of eq. (1.13) is calculated in a similar manner

$$I_a = \int dr_B' dr_B'' dr \exp(-ikr_B')t_B^+(r_B', r_B'')G_0^+(r_B'', r)\varepsilon r\phi_A(r) \qquad (1.16)$$

Here Green function is given by

$$G_0^+(r, r') = -2k\sum j_l(kr')h_l^+(kr)Y_l^m(r')Y_l^m(r) \qquad (1.17)$$

and h^+_1 is the l-st order spherical Hankel function; furthermore f_b is defined by

$$f_B(r_B', r_B'') = -\frac{1}{2\pi}t_B^+(r_B', r_B'') \qquad (1.18)$$

With eq. (1.17), we can obtain the second term of eq. (1.14) by integrating Ia with respect to r in a similar manner of eq. (1.14).

$$I_a = ikM\int dr_B' dr_B'' \exp(-ikr_B')f_B(r_B', r_B'')h_1^+(kr'')\varepsilon r'' \qquad (1.19)$$

The potential in the sample are treated in the so-called muffin-tin approximation, where within a sphere centered about each atom the core potential is spherically symmetric and outside the spheres the potential is averaged and set to a constant value. Within this approximation, the h becomes

$$h_1^+(kr') = -\frac{i}{kr'}\exp(ikr)(1+\frac{i}{kr_B'})$$

$$\approx -\frac{i}{kr_B'}\exp(ikr_B') \qquad (1.20)$$

$$\approx -\frac{i}{kR_{AB}}\exp(ikR_{AB} + ik_{AB}x_B')$$

$$R_{AB} = R_B - R_A \qquad R_{AB} = |R_{AB}| \qquad (1.21)$$

$$k_{AB} = \overline{R}_{AB} \qquad x_B' = r_B' - R_{AB} \quad (1.22)$$

In obtaining eq. (1.20), we used the relation that $x_B << R_{AB}$, $kR_{AB} >> 1$. Within these approximations, we obtain the single scattering term (I_a)

$$I_a = (\varepsilon \overline{R}_{AB})\frac{M}{R_{AB}} f_B(k, k_{AB})\exp(ikR_{AB} + ikR_{BA}) \qquad (1.23)$$

and $f_B(k, k_{AB}) = \sum f_{Bl}(k) P_l(\overline{kk}_{AB}) \qquad (1.24)$

$$f_{Bl} = \frac{1}{i2k}(2l+1)\{\exp(i2\delta_{Bl} - 1) \qquad (1.25)$$

here $P_l(\overline{kk}_{AB})$ is the Legendre polynomial.

The double scattering process is calculated in a similar manner as a single scattering term.

$$I_b = (\varepsilon \overline{R}_{AB})\frac{M}{R_{BA}R_{AB}} f_A(k, k_{BA}) f_B(k_{BA}, k_{AB})\exp(ikR_{BA} + ikR_{AB}) \quad (1.26)$$

In the above derivation, the following approximations are used to obtain the standard EXAFS expression.

One photon absorption

Dipole approximation

One electron scattering

Muff-tin approximation

Only main term is considered in each scattering process.

Substituting eqs. (1.14), (1.23), (1.26) into eq. (1.10), the transition probability W is

$$W(k) = CM^2 P(k)$$

$$P(k) = \left| \varepsilon\bar{k} + (\varepsilon\bar{R}_{AB}) \frac{1}{R_{AB}} f_B(\theta) \exp\{ikR_{AB}(1-\cos\theta)\} + (\varepsilon\bar{R}_{AB}) \frac{1}{R_{AB}^2} f_A(\pi - \vartheta) f_B(\pi) \exp(ikR_{AB}) \right|^2$$

(1.27)

where $\boldsymbol{\theta}$ is the angle between wave vector $\boldsymbol{k}$ and $\boldsymbol{R}$. The main terms of eq. (1.27) are given by

$$\langle K \cdot K \rangle = 1/3 \quad (1.28)$$

$$\mathrm{Re}\langle 2K \cdot I_a \rangle = (\varepsilon\bar{R}_{AB})^2 \, \mathrm{Re} \frac{i}{kR_{AB}^2} \{ f_B(\pi) \exp(i2kR_{AB}) + f_B(0) \} \qquad (1.29)$$

$$\langle I_a \cdot I_a \rangle = (\varepsilon\bar{R}_{AB})^2 \, \mathrm{Re} \frac{-i}{kR_{AB}^2} f_B(0) \qquad (1.30)$$

$$\mathrm{Re}\langle 2K \cdot I_b \rangle = (\varepsilon\bar{R}_{AB})^2 \, \mathrm{Re} \frac{i}{kR_{AB}^2} f_B(\pi) \exp(i2kR_{AB}) \{ \exp(i2\delta_{A,1}) - 1 \} \qquad (1.31)$$

where $K = \varepsilon\bar{k}$ and $< >$ is the angle average. Though eq. (1.27) consists of six terms, the terms as ***IaIb***, ***IbIb*** are negligible.

The expression for the basic EXAFS then becomes

$$\chi(k) = \frac{P(K) - \langle K \cdot K \rangle}{\langle K \cdot K \rangle} = (\varepsilon\bar{R}_{AB})^2 \, \mathrm{Im} \frac{-3}{kR_{AB}^2} f_B(k,\pi) \exp\{ i(2kR_{AB} + 2\delta_{A,1}) \} \quad (1.32)$$

Equation (1.32) means that EXAFS is produced by the interference between the double scattering wave (***Ib*** term) and the outgoing wave (***K*** term), and ***Ia*** and the second term of ***Ib*** is cancelled out.

The lifetime of the state $f>$ has been neglected in this derivation. There are two contributions to the lifetime. The hole of atom, left behind after the excitation of the photoelectron, is filled in a time of the order of 10^{-15} s. The photoelectron itself has a finite lifetime because of scattering from the surrounding electrons and atoms. The lifetime effect is added phenomenologically in terms of a mean free path $\boldsymbol{\lambda}$, which adds the term $\exp(-2\boldsymbol{R}/\boldsymbol{\lambda})$ to $\boldsymbol{\chi}(\boldsymbol{k})$, giving

$$\chi(k) = (\varepsilon\bar{R}_{AB})^2 \, \mathrm{Im} \frac{-3}{kR_{AB}} f_B(k,\pi) \exp\{ i(2kR_{AB} + 2\delta_{A,1}) \} \exp\left(\frac{-2R_{AB}}{\lambda(k)} \right) \qquad (1.33)$$

2-1-2 Disorder [7-13]

The eq. (1.33) is the fundamental EXAFS equation regarding the radial distribution of atoms as a discrete delta type function. In the practical materials, however, it is finite-width radial distribution function. If factors other than the sine function in $\chi(k)$ are assumed to have negligible variation with R, the main effect is represented by the function $F(R)$.

$$F(R_{AB}) = \left\langle\left\langle \frac{1}{R_{AB}^{\,2}} \exp(i2\alpha R_{AB}) \right\rangle\right\rangle \qquad \alpha = k + \frac{i}{\lambda} \qquad (2.1)$$

where << >> implies the static and thermal averages. In performing this calculation only the case of small variations is considered. Here we define the displacement u from the equilibrium position

$$u_{AB} = u_B - u_A = R_{AB} - R_{AB}^{\,0} \qquad (2.2)$$

And if we also define the δu as the following

$$\begin{aligned} R_{AB} &= \langle R_{AB} \rangle + \delta u \\ \langle R_{AB} \rangle &= R_{AB}^{\,0} + \langle\langle u_{AB} \rangle\rangle \qquad (2.3) \\ \delta u &= u_{AB} - \langle\langle u_{AB} \rangle\rangle \end{aligned}$$

then $\langle\langle \delta u \rangle\rangle = 0 \quad (2.4)$

Since δu <<1, the eq. (2.1) can be expressed in power δu.

$$F(R_{AB}) = \frac{1}{R^2} \exp(i2\alpha R) \exp(Q); \qquad R = |\langle R_{AB} \rangle| \qquad (2.5)$$

$$Q = \sum \frac{(i2\alpha R)^m}{2^m m!} (-1)^n \left\langle\left\langle (1 - \frac{1}{2^2}\delta + \frac{1}{2^3}\delta^2 + ...)^m \delta^{m+n} \right\rangle\right\rangle \qquad (2.6)$$

where δ is small value defined as the following.

$$\begin{aligned} R_{AB} &= R(1+\delta)^{1/2} \\ \delta &= \frac{2\bar{R}\delta u}{R} + \frac{(\delta u)^2}{R^2} \qquad R = \langle R_{AB} \rangle \qquad (2.7) \end{aligned}$$

To obtain the eq. (2.5), the following cumulant expansion is utilized.

$$\langle \exp(x) \rangle = \exp\left(\sum \frac{\langle x^n \rangle}{n!} \right) \qquad (2.8)$$

With the additional approximation, $kR>>1$, $k\lambda<<1$, and $\frac{\delta u}{R}<<1\,\frac{\delta u}{\lambda}<<1$, the basic EXAFS equation (1.33) becomes

$$\chi(k) = \mathrm{Im}\sum -\frac{k}{R^2} f_b(\pi)\exp(i2kR + i2\delta_A)\exp(-\frac{2R}{\lambda})\exp(-2W)$$
$$\exp(-2W) = \exp\left(\sum \frac{(i2k)^n}{n!} C_n \right) \qquad (2.9)$$

where C_n is the n-th order cumulant average. In terms of ordinary averages, the leading cumulants are

$C_1=0$ (2.10)

$$C_2 = \left\langle\left\langle (\bar{R}\delta u)^2 \right\rangle\right\rangle + i\frac{2}{kR}(1+\frac{R}{\lambda})\left\langle\left\langle (\bar{R}\delta u)^2 \right\rangle\right\rangle + i\frac{1}{2kR}\left\{\left\langle\left\langle (\bar{R}\delta u)^2 \right\rangle\right\rangle - \left\langle\left\langle (\delta u)^2 \right\rangle\right\rangle\right\} \quad (2.11)$$

$$C_3 = \left\langle\left\langle (\bar{R}\delta u)^3 \right\rangle\right\rangle \qquad (2.12)$$

$$C_4 = \left\langle\left\langle (\bar{R}\delta u)^4 \right\rangle\right\rangle - 3\left\langle\left\langle (\bar{R}\delta u)^2 \right\rangle\right\rangle^2 \qquad (2.13)$$

The disorder is generally expressed by a simple Debye-Waller formula ($\exp(-2C_2k^2)$) in EXAFS equation. It means that only k^2 term is considered on expanding $\exp(-2W)$.

a) Structural disorder

When the structural disorder is present, the distribution function is a convolution of thermal and radial distribution functions. The thermal disorder means the atomic displacement from the equilibrium position caused by thermal vibration, while the static disorder means the geometrical displacement from the regular lattice position. Temperature dependent EXAFS measurements are carried out to extract the dynamical contribution by assuming that only thermal disorder depends on temperature, while static disorder does not depend on temperature.

b) Classical harmonic oscillator

In classical harmonic oscillator, the interatomic potential can be represented as

$$V(x) = cx^2 - gx^3 - fx^4 \qquad (2.14)$$

The distribution function $p(x)$ at the finite temperature (T) is written according to the Boltzmann statistic.

$$p(x) = \frac{\exp(-\beta V(x))}{Z} \quad (2.15)$$

$$Z = \int \exp\{-\beta V(x)\}dx \quad (2.16)$$

If the anharmonicity of the potential is small comparing with the temperature, the evaluation $\exp(\beta V(x))$ lead to

$$\exp\{-\beta V(x)\} = \exp(-\beta c x^2)(1 + \beta g x^3 + \beta f x^4) \qquad (2.17)$$

and cumulant coefficients are

$$\langle C_1 \rangle = \langle x \rangle = \int xP(x)dx = \frac{3g}{4c^2} kT(1 - \frac{3f}{4c^2} kT) \qquad (2.18)$$

$$\langle C_2 \rangle = \langle x^2 \rangle = \frac{1}{2c} kT(1 + \frac{3f}{c^2} kT) \qquad (2.19)$$

$$\langle C_3 \rangle = \langle x^3 \rangle = \frac{15g}{8c^3} (kT)^2 (1 - \frac{3f}{4c^2} kT) \qquad (2.20)$$

$$\langle C_4 \rangle = \langle x^4 \rangle = \frac{3}{4c^2} (kT)^2 (1 + \frac{8f}{c^2} kT) \qquad (2.21)$$

It is worthwhile to keep in mind that C_2 and C_3 are proportional to the temperature and to square of the temperature, respectively.

d) Second order cumulant

In this section, second order cumulant (C_2) is discussed in a harmonic oscillator system.

$$C_2 = \left\langle (\bar{R}\delta u)^2 \right\rangle = \left\langle (\bar{R}_{AB} u_B)^2 \right\rangle + \left\langle (\bar{R}_{AB} u_A)^2 \right\rangle - 2\left\langle (\bar{R}_{AB} u_B)(\bar{R}_{AB} u_A) \right\rangle \qquad (2.22)$$

where $\left\langle (\bar{R}_{AB}u_B)^2 \right\rangle$ and $\left\langle (\bar{R}_{AB}u_B)(\bar{R}_{AB}u_A) \right\rangle$ are the mean square displacement [MSD] and the displacement correlation function [DCF], respectively. This shows that the Debye-Waller factor in EXAFS differ in several respects from that in x-ray diffraction, where the Debye-Waller factor is given by $\exp(-q^2u^2/2)$ and $u^2=\langle u.q\rangle^2$, q being the momentum transfer. In EXAFS, $\left\langle (\bar{R}\delta u)^2 \right\rangle$ is shell dependent, being sensitive to the DCF, which decays slowly with distance. This correlation is such that only the modes contributing to radial motion are important for $\left\langle (\bar{R}\delta u)^2 \right\rangle$; contributions from long-wavelength acoustic modes, are suppressed.

Statistically, the thermal average of $f(q)=\langle \exp(iqu) \rangle$ is given by

$$f(q)=\frac{Tr[\exp(-\beta H)\exp(iqu)]}{Tr[\exp(-\beta H]} = \exp\left[-\frac{\hbar}{2NM}\sum\frac{\left|qe(\kappa|k_j)\right|^2}{\omega(k_j)}\{n(\beta\hbar\omega(kj)+\frac{1}{2}\right] \qquad (2.23)$$

$$n(x)=\frac{1}{\exp(x)-1} \qquad (2.24)$$

where N and M_κ mean the number of atoms and the mass of atom. $n(x)$ is the Bose factor and it represents the number of phonons at finite temperature. The value 1/2 originates from the zero point vibration. Substituting eq. (2.22) into eq. (2.23) we obtain

$$C_2=\frac{\hbar}{2N\{M_\kappa M_{\kappa'}\}}\sum\frac{\coth\left\{\frac{1}{2}\beta\hbar\omega(kj)\right\}}{\omega(kj)}\left[\omega_{\kappa'/\kappa}\left|\bar{R}_{AB}e(\kappa|kj)\right|^2+\omega_{\kappa/\kappa'}\left|\bar{R}_{AB}e(\kappa'|kj)\right|^2-\right.$$
$$\left.\bar{R}_{AB}e(\kappa|kj)\bar{R}_{AB}e(\kappa'|kj)\exp(ik\bar{R}_{AB})+cc\right] \qquad (2.25)$$

$$\omega_{\kappa'/\kappa}=\left(\frac{M_{\kappa'}}{M_\kappa}\right)^{\frac{1}{2}} \qquad (2.26)$$

d-1) Einstein Model

Here we consider the system, which consists of two kinds of atoms in the Einstein approximation. The Einstein model replaces the frequency of each optical branch by a frequency ω_e that does not depend on k, thus a projected density of states is given by

$$\rho(\omega) = \delta(\omega - \omega_E) \qquad (2.27)$$

Because each atom has no relation to the other atom, the third and fourth term of eq. (4.84) are 0; further within Einstein approximation, eq. (2.25) may be simplified to

$$C_2 = \frac{\hbar}{M\omega_E} \coth\left(\frac{1}{2}\beta\hbar\omega_E\right) \qquad (2.28)$$

$$M=2u \text{ (}u\text{: reduce mass)} \qquad (2.29)$$

This Einstein model is particularly appropriate for crystals such as germanium, for which $\rho(\omega)$ is strongly peaked at the optical end of the spectrum.

d-2) Debye Model

Here we consider the harmonic oscillator of simple cubic lattice. The eq. (2.25) is simplified to

$$C_2 = \frac{\hbar}{NM}\sum \frac{\coth\left\{\frac{1}{2}\beta\hbar(kj)\right\}}{\omega(kj)} \left|\overline{R}_m e(kj)\right|^2 \{1-\cos(kR_m)\} \qquad (2.30)$$

$$R_m = R_{ab}$$

The Debye model replaces all branches of the vibrational spectrum with three branches, each with the same linear dispersion relation $\omega=ck$. In addition, the summation of eq. (2.22) over the first Brillouisn zone is replaced by an integral over a sphere of radius k_d. As a results of these simplifications eq. (2.30) reduces to

$$C_2 = \frac{\hbar}{M}\int d\omega\rho(\omega)\frac{\coth\left(\frac{1}{2}\beta\hbar\omega\right)}{\omega} \qquad (2.31)$$

$$\rho(\omega) = D(\omega)\frac{1-\dfrac{\sin\left(\dfrac{R_m\omega}{v_s}\right)}{\dfrac{R_m\omega}{v_s}}}{N} \qquad (2.32)$$

We can expend the eq. (2.31) furtehrmore.

$$C_2 = \frac{6\hbar}{M\omega_D}\left[\left\{\frac{1}{4}+\left(\frac{T}{\Theta_D}\right)^2\Phi_1\right\} - \frac{1-\cos(k_D R_m)}{2(k_D R_m)^2} - \frac{T}{k_D R_m \Theta_D}\int \frac{\sin\left\{\left(\dfrac{k_D R_m T}{\Theta_D}\right)x\right\}}{\exp(x)-1}dx\right]$$

^^^^^^^^^^^^^^^^ (2.33)

$$\Phi_n = \int dx \frac{x^n}{\exp(x)-1} \qquad \Theta_D = \frac{\hbar\omega_D}{k} \qquad (2.34)$$

The ^^^^^ term corresponds to the mean square displacement (MSD) of A and B atoms, and the other terms correspond to the displacement correlation functions (DCF). Cumulant of the usual Debye-Waller factor of X-ray diffraction is the MSD of one atom, it is thus one half of the ^^^^ term,

$$\left\langle (\vec{k}\vec{u})^2 \right\rangle = \frac{3\hbar}{M\omega_D}\left\{\frac{1}{4}+\left(\frac{T}{\Theta_D}\right)^2\Phi_1\right\} \qquad (2.35)$$

Beni *et. al* [11] calculated the DCF and MSD of fcc and bcc crystal to reveal that the contribution of DCF is important at high temperature.

2-2 XAFS measurements

2-2-1 Newly built system

a) Chamber

An UHV system for XAFS measurements was newly built for this study at first. The chamber is pumped by a turbo molecular pump (300l/sec) and the base pressure is about 7×10^{-10} torr. It is equipped with a hand-made K-cell, thickness monitor, a quadruple mass spectrometer, an ion gauge and a heater using infrared ray.

We have experimented at the soft x-ray station BL11B and hard x-ray station BL7C or 12C of the Photon Factory in the National Laboratory for High Energy Physics. Since soft x-ray is needed to go through in UHV, the chamber is connected to the storage ring without a window at soft x-ray station, while hard x-ray can pass through air, x-ray is emerged from the Be window at hard x-ray station. The Be window is, thus, needed to keep the chamber UHV and to transmit X-ray at the hard x-ray station. The fluorescence yield detection method was employed by using an UHV compatible gas-flow proportional counter at soft x-ray region, while it was employed by using solid state detector at hard x-ray region. Thus, two types of chambers have been built for XAFS measurements at soft x-ray station and hard x-ray station. In all overview is shown in Fig. 1 and Fig. 2.

b) Sample manipulator

The high-precision manipulator (SHINKUU KOGAKU) enables us to position a sample in three orthogonal axes (the z-direction is along the axis of the manipulator) in the UHV chamber. Rotation of 360° about the z-axis is provided by a differential-pumping rotation feedthrough.

A sample is mounted on a Ta sample holder and clipped by thin Ta foils softly (see

fig 3). This holder is connected to the two electric feed through and the holder is annealed up to 1200 K by passing direct current through it. A chromel and alumel thermocouple is inserted between the sample and the holder. The sample is cooled down to 120 K by liquid nitrogen poured into the cryostat. The sample is isolated electrically from the earth for the measurement of the sample current induced by the X-ray.

2-2-2 Beamline

a) BL-11B (soft x-ray beamline) [14, 15]

This beamline covers the energy range from 2000-4500 eV and it is constructed for soft x-ray XAFS measurements. This beamline mainly consists of a double crystal monochromator and focusing mirror, which is placed 17 m downstream of the source. The mirror is nickel-coated single crystal cylindrical mirror with a water-cooled holder and a variable bending mechanism was installed (see fig. 4)

The double crystal monochromator was designed based on the same principles as JUMBO at SSRL [16, 17]. The scanning and fine adjustment mechanisms are outside the vacuum. The second crystal is set to a calculated Bragg angle and is only rotated with the high precision goniometer, where a rotary encoder is directly attached to the rapture shaft. The first crystal and its whole assembly including the goniometer are mounted on a high precision cross roller linear slide and are translated. A linear encoder provides a relative position of the slide, Bragg angles from 23° to 75° are available. The essential requirement for double crystal monochromator is to maintain the relative alignment of the two crystals precisely as the Bragg angle is changed. For the present monochromator, this is achieved by using PZT, which is attached to the first crystal. Ge(111) or InSb(111) are used for double crystals, which are 20×20×3 mm. The energy resolution is from 0.8 eV in the energy range 2000-4500 eV, and at

the normal ring operation condition of 2.5 GeV and 300 mA, the photon flux is 2×10^{11} photons/s with the spot size of 5×5 mm.

b) BL-12 C (hard x-ray beamline) [18]

This beamline covers the energy range from 4000-18000 eV and it is constructed for hard x-ray XAFS measurements. This beamline also consist of mainly a double crystal monochromator and a bent cylindrical mirror (see fig. 6). A crystal monochromator was chosen as the first optical element in order to realize a high energy resolution. The monochromatic beam is focussed at 31.2 m from the source point by a bent cylindrical mirror placed at 20.8 m. A water-cooled slit system placed before the monochromator also functions a vertical beam-position monitor.

The ultra-high vacuum environment of the storage ring is separated by a pair of 0.2 mm thick beryllium window and 0.05 mm thick Kapton window separate the beamline vacuum from the atmosphere. Helium gas flows between the last beryllium window and the Kapton window in order to prevent the oxidation of the beryllium window by ozone produced by X-rays.

X-ray below 23 keV are focused by the mirror, while unfocussed X-rays above 23 keV can be used by removing the focusing mirror. The practical lower energy limit is 4 keV, which is determined by the absorption by the beryllium window and the atmosphere.

The first crystal stays on the rotation axis and the white beam hits the same position, independent of the Bragg angle. It is attached to a water-cooled nickel-coated copper block. The second crystal moves according to guides which were designed to keep the exit beam position independent of the Bragg angle. Si(111) crystals are used below 16 keV and Si(311) crystals are used above this energy.

2-2-3 Detection method

Several techniques for measuring EXAFS have been developed. The most obvious and widely used method is to measure the absorption of the sample by monitoring the incoming, I_0, and transmitted, I flux. The absorption is then given by

$$ux=\ln(I_0/I)$$

where u is the linear absorption coefficient and x is the sample thickness. In some cases it is advantageous to measure the adsorption by monitoring process that are proportional to the absorption. Two of these are to measure x-ray fluorescence and emission of Auger electrons. Monitoring such a process is useful when the EXAFS signal is only a small fraction of the total adsorption.

Auger emission and x-ray fluorescence are competing processes. Their relative strengths depend on the atomic number of the absorber. In light elements Auger emission is more probable, while for heavy elements fluorescence becomes more likely. For the same element fluorescence is more likely for K-shell holes than for L-shell holes.

The fluorescence radiation results from the filling of the core hole generated by the absorption of a x-ray photon, For the K shell this is dominated by the production of Ka radiation. The energy of this radiation is characteristic of the absorbing element and is less than the original exiting radiation. The background consists of elastically and Compton scattered radiation, both of which are at higher energies than the fluorescence line. Thus, a suitable energy dispersive detector can discriminate the background from the signal. It will be shown that the fluorescence technique gives better data than simple transmission when the absorption form the element of interest is less than a few percent of the total absorption in the sample.

Reference

[1] D. E. Sayers, E.A. Stern, F.W. Lytle, Phys.Rev.Lett. 27 (1971) 1204.

[2] E.A. Stern, Phys. Rev. B 10 (1974) 317.

[3] E.A. Stern, D.E. Sayers and F.W. Lytle, Phys. Rev. B 11 (1975) 4836.

[4] P.A. Lee and G. Beni, Phys. Rev. B 15 (1977) 2862

[5] P.A. Lee and J.B. Pendry, Phys. Rev. B 11 (1975) 2795.

[6] See, for instance, X-ray Absorption: Principles, Applications, Techniques of EXAFS, SEXAFS and XANES, edited by D. C. Koningsberger and R. Prins (Wiley, New York, 1988).

[7] E. D. Crozier, and J. A. Seary, Can, J. Phys. 58, 1388 (1980).

[8] E. D. Crozier and J. A. Seary, Can, J. Phys. 59, 876 (1981).

[9] G. Bunker, Nucl. Instrum. Method, 207, 437 (1983).

[10] J. M. Tranquada, and R. Ingalls, Phys. Rev. B. 28, 3520 (1983).

[11] G. Beni, and P. M. Platzman, Phys. Rev. B 14, 1514 (1976).

[12] E. Sevillano, H. Meuth, and J. J. Rehr, Phys. Rev. B 20, 4902 (1979).

[13] R. B. Greegor, and F. W. Lytle, Phys. Rev. B 20, 4902 (1979).

[14] T. Ohta, P. M. Stefan, M. Nomura, and H. Sekiyama, Nucl. Instr. And Meth. A246, 373 (1986).

[15] Y. Kitajima, J. Elec. Spec. Relat. Phenom. 80, 405 (1996).

[16] J. Cerino, J. Stohr, N. Hower, and R. Z. Bachrach, Nucl. Instr. And Meth. 172, 227 (1980)

[17] Z. Hussain, E. Umbach, D. A. Shirley, J. Stohr, and J. Feldhaus, Nucl. Instr. And Meth. 195, 115 (1982)

[18] M. Nomura and A. Koyama, KEK Report 95-15 (1996).

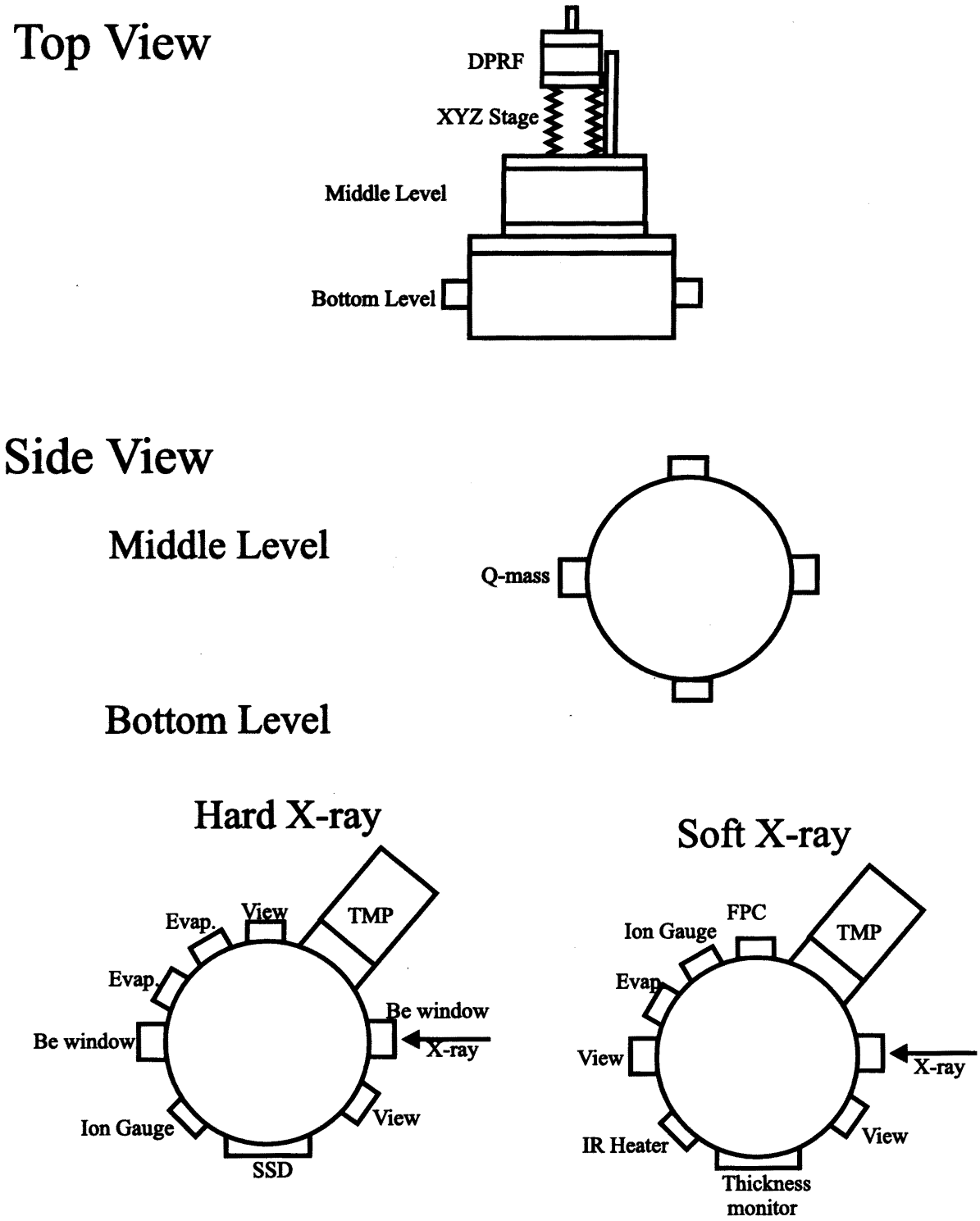

Fig. 1 The layout of the chamber for the XAFS measurement at soft X-ray beamline and that for hard x-ray beamline

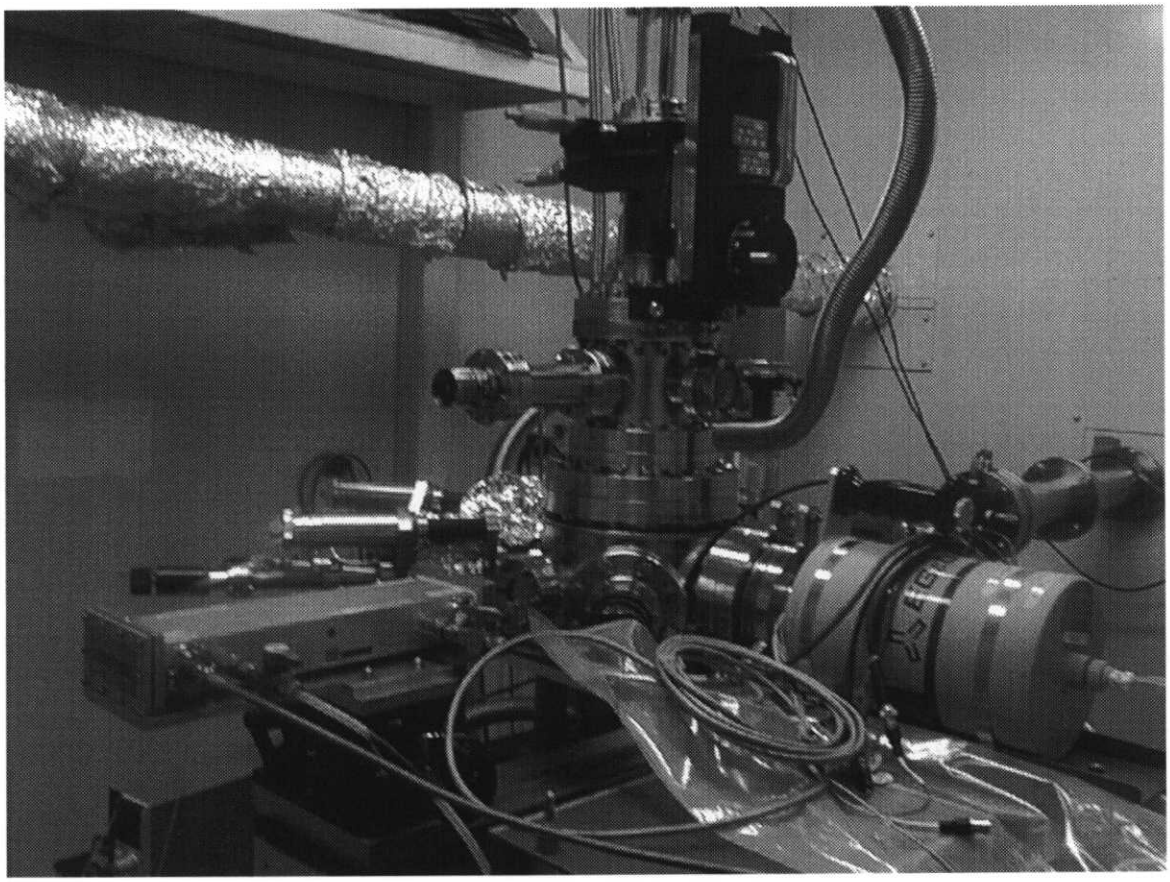

Fig. 2 The newly built chamber set at the hard X-ray beam line BL-7C.

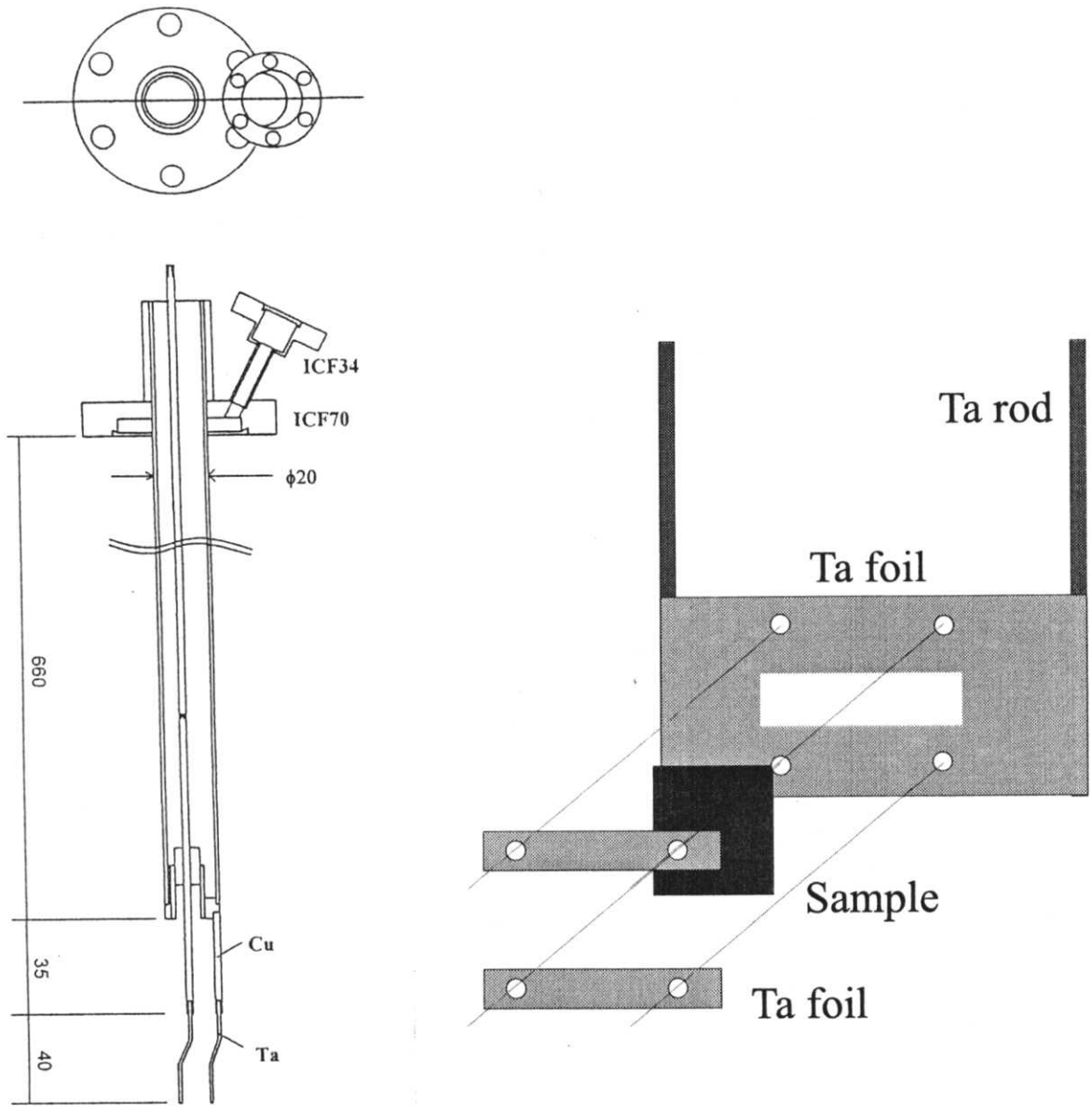

Fig. 3 Schematic drawing of liquid nitrogen cryostat (left) and sample holder (right).

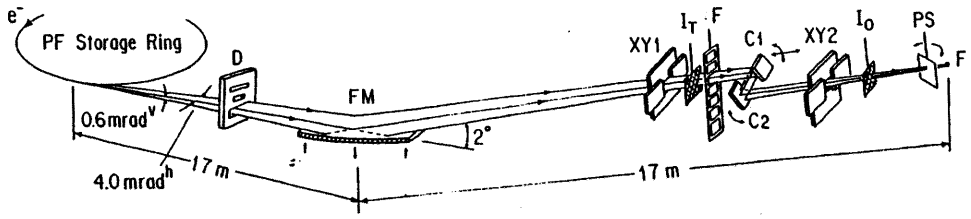

Fig. 4 Schematic view of the soft x-ray beamline optics. D: Diaphragm, FM: focusing mirror, XY1: XY slit, F: filter assembly, C1: first crystal, XY2: XY slit, Io: Io monitor, F: focal point.

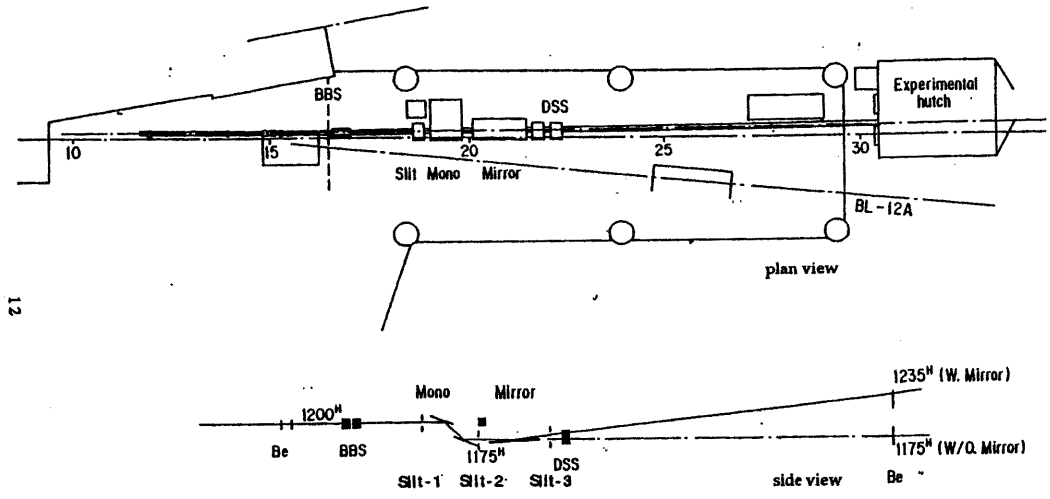

Fig. 5 Schematic drawing of the beamline 12C. The white X-rays are monochromatized by a double crystal monochromator, then focused by a Rh coated bent cylindrical mirror.

3. Heteroepitaxial growth of KCl on a cleaved (001) face of KBr studied by extended x-ray absorption fine structure

3. 1 Introduction

Vapor-phase crystal growths of ionic compounds have attracted wide attention for technological applications to microelectronics, nonlinear and ferroelectric devices [1,2]. Epitaxial growth of alkali halides on different alkali halide crystal has been studied to date [3-6]. Using RHEED, Shultz [4] revealed heteroepitaxy of alkali halides over a wide range of the lattice mismatch of -39 % to 90 %. Recently, Saiki *et al.* [5, 6] studied the initial stage of the molecular beam epitaxy of LiF and KCl on KBr(001) using RHEED, EELS and AES. In the case of KCl/KBr with the lattice mismatch of -4.7 %, it was found that KCl grows epitaxially in a layer-by-layer mode at room temperature and the in-plane lattice constant decreases continuously from the KBr one to that of KCl [5, 6].

Although the epitaxial films exhibit long-range ordered structure, the local structure could be different from that expected by the averaged lattice constant. This is well known in the cases of binary solid solutions. In order to study a growth style, it is also of great importance to know the early stage from the local structure point of view. Since EXAFS provides information on the local structure, this technique is adequate for studying the initial stage of crystal growth. We can also investigate anisotropy of surface structure for thin films by polarization-dependent EXAFS analysis. In the present study, we have examined thickness dependence of the surface structures of KCl/KBr(100) by means of Cl *K*-edge EXAFS. In this system, the K-Cl bond parallel to the surface was studied by the diffraction techniques, while the K-Cl bond normal to the surface has not been reported. For the bond normal to the surface, the influence of the substrate should be different from that for the bond parallel to the surface. The resultant local structure of the thin films is discussed by comparison with the previous diffraction studies.

3. 2 Experimental

The KCl thin film on KBr(001) was prepared according to the method described previously [5]. Growth of KCl films has been done in an UHV chamber with a base pressure of 1×10^{-9} torr. KCl was evaporated from a Knudsen cell. A cleaved KBr(001) surface was used as a substrate. No impurities of S or Cl were detected after the heat treatment of 573 K. The growth speed was monitored by a quartz crystal oscillator, and was typically 10 Å/min. Cl *K*-edge EXAFS measurements were carried out at the soft X-ray double-crystal monochromator station BL-11B of the Photon Factory at the Institute of Materials Structure Science [7, 8]. Cl *K* fluorescence yield detection was employed using an UHV-compatible gas-flow proportional counter with a P10 gas (10 % CH_4 in Ar) [9]. In order to reduce the Br-*L* fluorescence intensity, a Kapton window (50 μm thickness) was placed in front of the fluorescence detector. The EXAFS spectra of KCl/KBr(001) were taken at normal (θ=90°) and grazing (θ=20°) X-ray incidence at a temperature of 150 K. For the reference, EXAFS of bulk KCl (fine crystals) at 100 K was recorded by means of total electron yield detection.

3. 3 Results

Extraction of the EXAFS function $\chi(k)$ (k is the photoelectron wave number) was carried out according to well-established procedures: pre- and post-edge background subtraction and subsequent normalization with the atomic absorption coefficients [10, 11]. The resultant $k^2\chi(k)$ functions of the KCl/KBr systems with the KCl thickness d of 2, 6 and 25 Å are depicted in Fig. 1, and corresponding Fourier transforms are shown in Fig. 2. The k range employed in the Fourier transform was 2.8-8.7 $Å^{-1}$. In the Fourier transforms, dominant peaks at 2.5 Å are immediately ascribed to the first-nearest neighbor (NN) K coordination. The peak distance for the film d=6 Å at θ=90° is clearly shifted to a shorter distance side compared to that for d=2 Å, this being quantitatively clarified by the following curve-fitting analysis. The curve-fitting analysis of the first-NN K-Cl shells in k space (Δk_{fit}=3.1-8.4 $Å^{-1}$) was subsequently performed after Fourier filtering (ΔR_{fit}=2.2-3.1 Å), using theoretical standards given by FEFF 6 [12, 13]. Fitting

parameters employed were the effective coordination number N^*, the interatomic distance R and the mean square relative displacement C_2. The intrinsic loss factor S_0^2 was fixed to be 0.73, which was determined from the bulk KCl data.

The EXAFS results are summarized in Table 1. For the thickness dependence, the first-NN Cl-K distances given by the normal incidence (θ=90°) measurements are compared, which correspond to the in-plane KCl distances parallel to the surface. The results in Table 1 clarify that, with an increase in the film thickness, the K-Cl bond is shortened gradually and approaches a bulk value of 3.13 Å. The present finding is in good agreement with the previous results of the lattice constants [5, 6]. In the initial stage, however, they claimed the formation of the coherent bonding at the KCl/KBr interface [5, 6], this indicating that the in-plane K-Cl distance should be the bulk KBr distance of 3.28 Å. The present EXAFS analysis essentially contradicts with the previous remark, since even in the initial stage, the K-Cl bond length is not close to the K-Br distance but rater similar to the bulk KCl distance.

3. 4 Discussion

According to the previous RHEED studies [5,6], the surface in-plane lattice constant of KCl films on KBr decreases gradually and approaches the bulk value around d=20 Å. Recently, Natori *et al.* [14] have theoretically studied the initial stage of heteroepitaxy of KCl/KBr(001). It was concluded that the two-dimensional island configuration is more stable than the three-dimensional one, and the overgrown and substrate atoms are bonded coherently. To the contrary, the present EXAFS study revealed that the in-plane K-Cl bond is rather close to the bulk KCl distance, even at the interface.

Such a behavior can usually be found in binary solid solutions [15, 16]. The lattice constant and interatomic distance were studied systematically by changing x in AB_xC_{1-x}. Boyce and Mikkelsen [17] discussed the x dependence of the bond distance in ionic crystals and covalent materials. They defined a parameter α_{AB} as

$$\alpha_{AB} = \frac{R_{AB}^{0} - R_{AB}^{EXT}}{R_{AB}{}^{0} - R_{AC}{}^{0}}$$

where R^0_{AB} and R^0_{AC} are the A-B and A-C distances in pure AB and AC compounds, respectively, and R^{EXT}_{AB} is the $x \rightarrow 0$ limit of R_{AB} (x). In the virtual crystal approximation, α_{AB} should be unity, while the EXAFS studies revealed much smaller α_{AB} of $\approx$0.4 for ionic crystals and of less than $\approx$0.2 for covalent materials [15, 16].

The present study yielded $\alpha_{AB} \approx 0.27$ for d=2 Å, which is slightly smaller than the typical value of 0.4 for ionic crystals and is greatly different from that of the coherent bonding of α_{AB}=1.0 (in the heteroepitaxy film the coherent bonding at the interface corresponds to the virtual crystal approximation). In the case of the dilute limit of solid solutions, the guest ions are completely surround by different chemical species. Even in such a case, α_{AB} does not converge to unity. In the present epitaxial film, the K-Cl interactions are extended in the horizontal direction, and the resultant α_{AB} could be smaller than that of ionic solid solutions. Thus the present finding of α_{AB}=0.27 at d=2 Å might be reasonable. Conclusively, one can recognize that even in the initial stage of crystal growth, the overgrown and substrate atoms are not necessarily bonded coherently and the overgrown chemical species is likely to maintain the natural local structure. As in the case of solid solutions, the diffraction technique gives only the averaged structure and erroneous bond distance even in the presence of long-range order. Such a discrepancy may be caused by the epitaxial KCl film consisting of significantly distorted layers containing a large number of defects.

An anisotropy of the KCl bond distance was found for d=6 Å in Table 1. The in-plane K-Cl bond distance of 3.16 Å (θ=90°) is larger than the out-of-plane one of 3.13 Å (θ=20°). The out-of-plane K-Cl bond distance is essentially the same as the bulk KCl value. This means that the out-of-plane K-Cl distance completely maintains the natural K-Cl distance even in thin films, because surface tension cannot be expected in the vertical direction.

Finally, let us discuss the effective coordination number N^*. Assuming that the KCl

film of the rock-salt structure is complete and flat, N^* (90°) (in-plane contribution) should be 6.0. The experimentally obtained N^* (90°) values in Table 1 are noticeably smaller than the expected value of 6.0. This may be caused by the domain formation. Since the experimental N^* (90°) decreases with an increase in the film thickness, one can imagine that the domain size is smaller in thicker films. This is qualitatively consistent with the previous discussion, whereby the domain size shows a minimum thickness of around 20 Å [5, 6]. One can estimate the domain size from experimentally obtained N^* (90°). If the domain size is assumed to be $La \times La$ (a is the lattice constant of KBr), N^* (90°) can be written in the form of $3(2L\text{-}1)/L$. This yielded L=2.7 for d=2 Å [N^* (90°)=4.9], which corresponds to 20×20 Å^2. Note here that the domain size given by STM or AFM could be larger than that given by EXAFS. The former usually ignores defects and dislocations in the domain, while the latter is strongly influenced by the presence of imperfections in the domain crystal. On the other hand, the N^* (20°) value obtained experimentally is 3.4, which is again smaller than the expected value of 4.7 (assuming two perfect layers). This should also originate from imperfections of the flat film growth and the film surface might be somewhat roughened.

3. 5 Conclusion

We have measured and analyzed Cl K-edge EXAFS spectra of epitaxially grown KCl films on KBr(001). In the initial stage of crystal growth, the in-plane K-Cl bond distance is elongated due to the substrate effect. The K-Cl bond distance is, however, rather close to the bulk KCl distance (not to the KBr distance), this contradicting with the previous idea of coherent bonding at the interface. As film thickness increases, the K-Cl bond distance is shortened and the d=25 Å film shows the K-Cl natural distance for bulk KCl. Because there is no distortion in the normal direction, the out-of-plane K-Cl bond distance is equal to the natural distance from the beginning of the epitaxial growth. It is of great importance to investigate the local structure in epitaxial films by means of EXAFS, since the diffraction method gives only the average structure with a long-range order.

References

[1] K. Nashimoto, D. K. Fork, T. H. Geballe, Appl. Phys. Lett. 60 (1992) 1199.

[2] M. Yoshimoto, K. Shimozono, T. Maeda, T. Ohnishi, M. Kumagai, T. Chikyow, O. Ishiyama, M. Shinohara, H. Koinuma, Jpn, J. Appl. Phys. 34 (1995) L688.

[3] M. H. Yang, C. P. Flynn, Phys. Rev. Lett. 62 (1989) 2476.

[4] L. G. Shcultz, Acta. Cryst. 4 (1951) 483.

[5] K. Saiki, Y. Nakayama, A. Koma, Surf. Sci. 250 (1991) 27.

[6] K. Saiki, Appl. Surf. Sci. 113/114 (1997) 9.

[7] T. Ohta, P. M. Stefan, M. Nomura, H. Sekiyama, Nucl. Instrum. Methods A 246 (1986) 373.

[8] M. Funabashi, M. Nomura, Y. Kitajima, T. Yokoyama, T. Ohta, H. Kuroda, Rev. Sci. Instrum. 60 (1989) 1983.

[9] M. Funabashi, T. Ohta, T. Yokoyama, Y. Kitajima, H. Kuroda, Rev. Sci. Instrum. 60 (1989) 2505.

[10] D. C. Koningsberger, R. Prins (Eds.), X-Ray Absorption: Principles, Applications, Techniques of EXAFS, SEXAFS and XANES, Wiley, New York, 1988.

[11] T. Yokoyama, H. Hamamatsu, T. Ohta, EXAFS Analysis Program EXAFSH, The University of Tokyo, Tokyo, 1993.

[12] S. I. Zabinsky, J. J. Rehr, A. Ankdinov, R. C. Albers, M. J. Eller, Phys. Rev. B 52 (1995) 2995.

[13] J. J. Rehr, J. Mustre de Leon, S. I. Zabinsky, R. C. Albers, J. Am. Chem. Soc. 113 (1991) 5135.

[14] A. Natori, A. Tanaka, H. Yasunaga, Thin Solid Films 281/282 (1996) 43.

[15] H. Sato, T. Yokoyama, I. Ono, K. Kaneyuki, T. Ohta, Jpn. J. Appl. Phys. 31 (1992) 1118.

[16] J. B. Boyce, J. C. Mikkelsen Jr., Phys. Rev. B 31 (1985) 6903.

[17] L. Pauling. M. L. Huggins, Z. Kristallogr. Kristallgeom. Kristallphys. Kristallchem 87 (1934) 205.

Table 1: The result of the EXAFS analysis for the first-NN K-Cl shell in the thin KCl films on KBr at 150 K.

d(Å)	θ(°)	R(Å)	N^*	C_2 (10^{-3} Å^2)
2	90	3.17	4.9	1.10
6	90	3.16	4.2	0.84
6	20	3.13	3.4	0.55
25	90	3.13	4.1	0.64

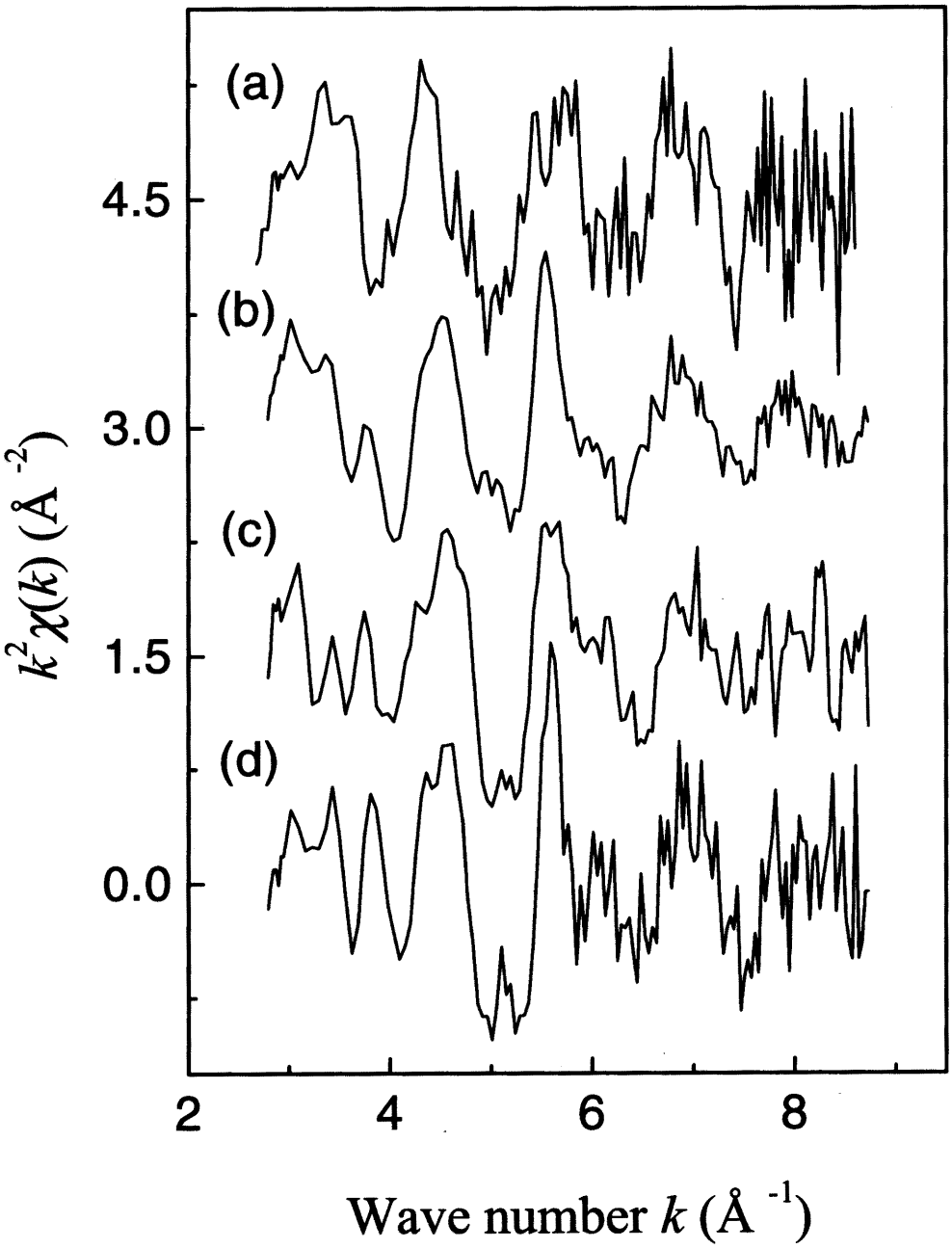

Fig. 1. Cl *K*-edge EXAFS oscillations $k^2\chi(k)$ of KCl/KBr(100) at 150 K: (a) d=2 Å θ=90°; (b) d=6 Å θ=90°; (c) d=6 Å θ=20°; (d) d=25 Å θ=90°

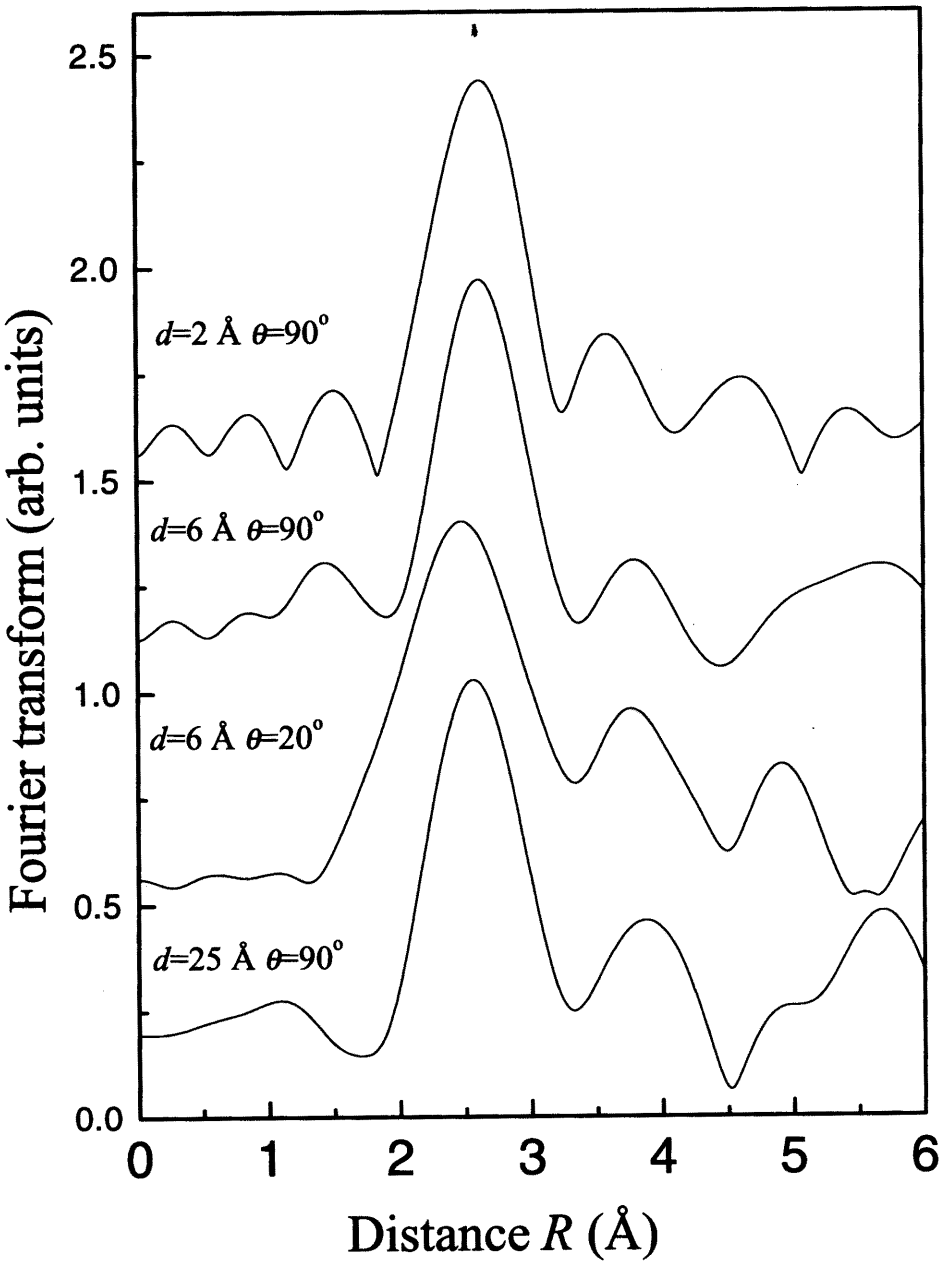

Fig. 2. Fourier transforms of Cl *K*-edge EXAFS functions $k^2\chi(k)$ of Fig. 1.

4 Interfacere structure of alkali-halide heteroepitaxial films studied by x-ray-absorption fine structure

4.1 Introduction

Recent development of the molecular beam epitaxy (MBE) technique has made it possible to produce various well-defined layered films.[1] Many interesting phenomena are observed on these films, and this technique has been extensively used in the electronic industry. In order to prepare such an ideal layered film, it is necessary to elucidate the structure at the interface between the film and substrate since the interface interaction plays an important role in the determination of the growth mode.

The interface structure has been studied by various methods such as LEED (low energy electron diffraction), TEM (transmission electron microscopy), and EXAFS (extended x-ray-absorption fine structure). Metal or semiconductor films, Ni/Cu(100) (Ref. [2]) and GaAs/AlAs(100) (Ref. [3]), are found to form coherent bonds at the interface; that is, the in-plane bond distance of the film is the same as that of the substrate. Unfortunately, since metal and semiconductor films require severe lattice matching conditions, we can study interface structures only for limited systems where the difference of the lattice constants between the film and substrate is extremely small.

On the other hand, in case of alkali halides films, which grow in a layer-by-layer mode even with the lattice matching up to as much as 10%,[4, 5, 6] the exact interface structure has not been determined by LEED because of the charging problem. Instead, the lattice constant has been measured by using RHEED (reflection high energy electron diffraction), and it was revealed that the in-plane lattice constant steadily changes from the bulk value to that of the substrate as the film thickness decreases. Because a single diffraction line was observed during the growth of the alkali-halide systems (pseudomorphic growth), a coherent bond is concluded to be formed at the interface.

EXAFS is a powerful technique for the clarification of the interface structure

of alkali halides thin films. EXAFS gives the local ordered structure around x-ray-absorbing atoms, and by using polarized x rays, the in-plane and out-of-plane bonds can be examined separately. Recently, we have studied the in-plane K–Cl bond distance at the interface in KCl/KBr(100) by EXAFS,[7] it was revealed that the in-plane K–Cl bond is elongated by 0.04 Å compared to the bulk KCl (3.13 Å), but it was not relaxed to the substrate bond distance (3.28 Å). It was supposed that the discrepancy between the results of EXAFS and RHEED originates from the fact that RHEED is less surface sensitive and gives information about only the average structure of the substrate and film, including defects. Although RHEED is a powerful tool for investigating the growth mode, it is hard to determine the local structure from a microscopic point of view. The interface structure of the alkali halides is thus an open question in contrast to some metal and semiconductor films studied by LEED.

In the present study, the local interface structures of thin NaCl and KCl films grown on a NaBr substrate has been investigated by means of EXAFS. The former NaCl (bulk lattice constant 2.80 Å) film has a smaller lattice constant than that of the substrate NaBr (2.96 Å), while the latter KCl film has a larger lattice constant (3.13 Å). The second aim of the present investigation of KCl/NaBr is to discover to what degree the deposited species are embedded in the substrate. Although Saiki *et al.*[4] have excluded the possibility of the formation of mixed crystals by means of optical measurements, there is no direct structural evidence to support this conclusion from the microscopic point of view. We have therefore attempted to solve this problem by analyzing the local structure around the Cl atoms. In addition, classical Monte Carlo (MC) calculations were carried out for the 1 ML thick KCl/KBr system. Based on the MC and EXAFS results, the bonding character at the interface is discussed.

4.2 Experimental

KCl and NaCl thin films on NaBr(100) were prepared according to the method described previously.[4, 7] Growth of the films has been done in an ultrahigh vacuum (UHV) chamber with a base pressure of 1×10^{-9} Torr (1 Torr = 133 Pa). A cleaved

NaBr(100) surface was used as a substrate. The substrate was cleaned by annealing up to 673 K. KCl and NaCl were evaporated from Knudsen cells. The growth speed was monitored by a quartz crystal oscillator. The resultant film thickness prepared was 1, 3, 6, and 20 ML. Precise thickness was determined by the chromatographic analysis after all the spectroscopic experiments.

Cl K-edge XAFS measurements were carried out at the soft x-ray double-crystal monochromator station BL-11B of the Photon Factory in the Institute of Materials Structure Science.[8, 9, 10] The factor of linear polarization was estimated to be larger than 0.97. Higher order harmonics were eliminated by Ni-coated pre- and post-focusing mirrors. The energy resolution of the present Ge(111) monochromator was about 1.5 eV around the Cl K-edge region. The absolute photon energy was calibrated with the assumption that the strong resonance of K_2SO_4 ($S1s \rightarrow t_2$) appears at 2481.7 eV. The fluorescence yield detection method was employed to obtain Cl K-edge XAFS by using an UHV-compatible proportional counter with P10 gas (10% CH_4 in Ar).[11] To reduce the Br-L fluorescence intensity, a Kapton film (50 μm thickness) was placed in front of the fluorescence detector. For the normalization of the fluorescence yield spectra with the intensity of the incident x-rays, we measured a drain current from a Cu mesh in the upstream of the sample. The XAFS spectra of KCl and NaCl on NaBr(100) were taken at normal x-ray incidence, this implying that only in-plane bonds were observed. Unfortunately, some Bragg reflections from the substrate prevented us from measuring the spectra at grazing x-ray incidence. The measurements were performed at 130 K and the temperature was monitored with a chromel-alumel thermocouple which was spot-welded on a Ta sheet attached to the sample surface. The temperature fluctuation was less than ± 3 K during XAFS measurements. For the reference spectrum in the XAFS analysis, we have also taken the Cl K-edge XAFS of bulk KCl by the total electron detection yield mode using a channeltron.

4.3 Results and discussion

4.3.1 XANES

Figure 1 shows the Cl K-edge XANES of a 1 ML thick KCl film on NaBr(100) taken at normal x-ray incidence. The normal-incidence spectra should dominantly reflect the atomic configurations in the lateral direction. For comparison, spectra of bulk KCl and NaCl crystals are displayed. Evidently, the spectra of KCl and NaCl crystals are different, while that of the 1 ML thick KCl film is rather similar to that of the KCl crystal. This finding qualitatively indicates that mixed crystals were not formed at the interface but a KCl-like film was formed. If mixed crystals were formed, the normal-incidence spectrum of the 1 ML film should differ from the bulk KCl one.

4.3.2 EXAFS

Extraction of the EXAFS functions $\chi(k)$ (k is the photoelectron wave number) was carried out according to well-established procedures: pre- and post-edge background subtractions and subsequent normalization with the atomic absorption coefficients.[12, 13] Figures 2 and 3 show the $k^2\chi(k)$ functions and corresponding Fourier transforms for KCl/NaBr(100), respectively. The k range employed in the Fourier transform was 3.1–8.7 Å^{-1}. Since the EXAFS measurements were carried out at normal x-ray incidence, in-plane K–Cl distances were measured. In the Fourier transforms, the dominant peak at ~2.5 Å is ascribed to the first-NN (nearest neighbor) K–Cl coordination. In KCl/NaBr, the lattice constant of the substrate (bulk NaBr 5.92 Å) is smaller than that of the film (bulk KCl 6.26 Å). The peak is clearly shifted to a shorter distance side with a decrease in film thickness; namely the K–Cl bond distance was contracted due to the influence of the substrate.

The curve-fitting analysis of the first-NN shells was subsequently performed in k space after Fourier filtering and inverse Fourier transformation. The backscattering amplitudes and phase shifts for the shells were obtained from the empirical references of the KCl crystal. Fitting parameters employed were N^* (effective coordination number), R (interatomic distance), and ΔC_2. ΔC_2 implies the difference of the mean-square relative displacements between the sample (KCl film) and the reference

(bulk KCl crystal). The numerical results are summarized in Table 1.

All the KCl films grown on NaBr(100) show positive ΔC_2, this indicating that the films were less ordered than the KCl bulk crystal. Because the strain is large at the interface, the ΔC_2 would be large at the initial stage. The thickness dependence of ΔC_2, however, was opposite to our expectation. This should be caused by dynamic disorder. With the assumption that the atoms remain in the same electronic state irrespective of the film thickness, the force constant between two atoms becomes larger as the bond distance is contracted. Good examples can be found in binary solid solutions like $AgBr_xCl_{1-x}$ (Ref.[14]), where the Ag–Br bond is compressed due to the surrounding AgCl and the bond shows smaller C_2 compared to the AgBr crystal. In the present KCl/NaBr case, such dynamic effects contribute to the suppression of ΔC_2 for thinner films. This argument in turn suggests that the structure disorder is rather large even for thick films.

The NaCl/NaBr system has been subsequently analyzed, where the lattice constant of the substrate (NaBr 5.92 Å) is larger than that of the film (bulk NaCl 5.60 Å). The $k^2\chi(k)$ functions of the NaCl/NaBr system are depicted in Fig. 4 and corresponding Fourier transforms are shown in Fig. 5. The EXAFS results are also summarized in Table 1. Figure 6 shows the thickness dependence of the K–Cl and Na–Cl bond distance on KBr and NaBr(100).

The thickness dependence of the bond distance in the NaCl/NaBr system is quite similar to that of KCl/KBr. With an increase in film thickness, the Na–Cl bond distance was shortened gradually and approached a bulk value of 2.80 Å. For the previous 1 ML thick KCl/KBr case, the in-plane bond distance was also elongated by 0.04 Å but was not relaxed to the substrate bond distance. The diffraction study[4, 5] claimed the formation of the coherent bonding at the initial stage, this implying that the in-plane Na–Cl distance should be identical to the bulk NaBr distance of 2.96 Å. The present EXAFS analysis contradicts the previous remark. Although the Na–Cl bond length was found to be slightly elongated at the interface, the Na–Cl distance was still closer to the bulk NaCl distance rather than to the bulk NaBr distance.

In NaCl/NaBr, large ΔC_2 values indicate that the present films have some struc-

tural disorder and larger thermal fluctuation. In contrast to the KCl/NaBr system, ΔC_2 was larger at the initial stage, and the thickness dependence of ΔC_2 shows a similar trend to the KCl/KBr system. In both NaCl/NaBr and KCl/KBr cases, the films are not compressed but slightly expanded and are thus disordered at the interface.

Next the effective coordination number N^* is discussed. Assuming that the KCl and NaCl films of rock-salt structure are complete and flat, N^* (in-plane contribution) should be 6.0. The experimentally obtained N^* values in Table 1 are noticeably smaller than the expected value. This may be caused by imperfections during film growth, as is evident from large ΔC_2. Although the experimental and analytical errors are estimated to be considerably large ($\geq$0.4), the domain size can be roughly estimated from experimentally obtained N^*. If the domain size is assumed to be $La \times La$ (a is the lattice constant of the substrate), N^* can be written in the form of $3(2L-1)/L$. This yields L $\sim$3 for both 1 ML KCl/NaBr (N^*=4.8) and 1 ML KCl/KBr (N^*=4.9), and L $\sim$4 for 1 ML NaCl/NaBr (N^*=5.3). These values correspond to $\sim$20 Å islands.

There are two possible reasons for the discrepancy between the EXAFS and RHEED results. One is the fact that RHEED is not element-specific and is less surface sensitive. The average structure of the film and substrate gives the diffraction pattern, and it is therefore difficult to investigate the interface structure without interference from the substrate. On the other hand, EXAFS is an element specific technique. The present EXAFS measurements were carried out at normal incidence, where only the in-plane bonds were examined, this implying that information only from the films was extracted.

The other reason is based on the difference between short- and long-range order. Large ΔC_2 observed experimentally indicates that there are a lot of defects in the films. Due to these defects, the short-range order obtained by EXAFS does not have to correspond to the long-range order observed in by RHEED. Although ideally RHEED can determine the atomic positions of the films, the structure of the present alkali halide thin films are difficult to solve because of large disorder due to defects. EXAFS measures only the short-range ordered bonds. Judging from large

ΔC_2 and small N^*, the films should consist of many small domains. In such a situation, EXAFS gives the averaged ordered structure in the domain, and the distance between different domains does not affect the results because it is significantly larger than that in the domain. On the contrary, RHEED gives the average for intra- and inter-domain structure.

Although it is supposed that the latter reason is more likely to explain the different results of EXAFS and RHEED, only the experimental results might not be sufficient to eliminate the former reason. In order to elucidate the correct explanation, the examples of binary solid solutions will be recalled, where the long-range order does not correspond to the short-range order. Moreover, in the next section, the results of the MC calculations are shown. In the case of the former explanation, the substrate should be relaxed to give a single diffraction pattern, while in the latter case the substrate does not have to be relaxed. Although it is difficult to distinguish between these two reasons experimentally, the MC simulations may provide some insight.

The lattice constants and interatomic distances in binary solid solution AB_xC_{1-x} systems were studied systematically by changing the composition ratio x.[14, 15, 16] The lattice constant determined by x-ray diffraction varies linearly with the composition and the diffraction line width is kept constant. Boyce *et al.*[15] have defined the parameter α_{AB} which represents flexibility of the A–B as

$$\alpha_{AB} = \frac{R^0_{AB} - R^{EXT}_{AB}}{R^0_{AB} - R^0_{AC}}, \tag{1}$$

where R^0_{AB} and R^0_{AC} are the interatomic A–B and A-C distances of pure AB and AC compounds, respectively. $R_{AB}(x)$ is the A–B distance obtained experimentally, and R^{EXT}_{AB} is the dilute ($x \rightarrow 0$) limit of $R_{AB}(x)$. α_{AB}=0 means that the bond distance is unchanged, while α_{AB}=1 implies that the bond distance is relaxed to that of the host AC. Judging from the change of the lattice constants and sharpness of the diffraction lines, it is speculated that the coherent bond might be formed at the dilute limit and α_{AB} should be unity (virtual crystal approximation). The interatomic distance given by EXAFS revealed that α_{AB} is $\sim$0.4 for ionic crystals and less than $\sim$0.2 for covalent compounds.[14, 15, 16] The bond does not relax to match the guest, but is likely to retain the natural bond distance.

The present and previous[7] works on thin films of NaCl/NaBr and KCl/KBr showed α_{AB}=0.24 and 0.26, respectively. These values were smaller than the typical value of ~0.4 for ionic crystals and were greatly different from that of the coherent bonding (α_{AB}=1.0). In the case of the dilute limit of solid solutions, the guest ions are completely surrounded by different chemical species. Even in such a case, α_{AB} does not converge to unity. In the present epitaxial film, the K–Cl interactions are extended only in the two-dimensional plane, and the resultant α_{AB} could be smaller than that of three-dimensional ionic solid solutions. Therefore, the present finding of α_{AB}~0.25 might be reasonable. The parameter α_{AB} for the NaCl/NaBr and KCl/KBr systems was found to be almost identical [the lattice matching conditions are also almost the same 5.4% for NaCl/NaBr and 4.6% for KCl/KBr)], this implying substantially equivalent interface structure for the two systems.

4.3.3 Monte Carlo simulation

Classical MC simulations for KCl/KBr(100) have been performed. The conclusions obtained for the KCl/KBr(100) system could be applied to other ionic systems such as NaCl/NaBr(100) investigated here. This is because we have discovered similar structures between NaCl/NaBr and KCl/KBr by EXAFS, and the potentials used in the MC calculations are also of the same type.

The MC simulations were based on the pair-potential approximation. With respect to the ionic interaction, the long-range Coulomb potential was calculated by the Ewald method.[18] For the short-range interactions repulsive exponential interactions and attractive London forces were taken into account. The interatomic potential $V_{ij}(r)$ (r is the interatomic distance between ions i and j) is given as

$$V_{ij}(r) = A_{ij}\exp(-\frac{r}{\rho_{ij}}) - \frac{C_{ij}}{r^6} - \frac{z_i z_j}{r}. \quad (2)$$

The assumed values of the parameters A_{ij}, ρ_{ij}, and C_{ij} for KCl and KBr were taken from reference (z_i was simply assumed to be either +1 or −1).[17] Simulations of bulk KCl and KBr were at first performed by using a cell containing 512 ions. The constant-temperature and constant-pressure (NPT) MC method was employed imposing three-dimensional periodicity. T=130 K and P=0 Pa were assumed. The resultant K–Cl and K–Br interatomic distances were 3.15 and 3.30 Å, respectively.

These values are close to the experimental distances of 3.13 and 3.28 Å, this implying high reliabilities of the present pair potentials.

The calculations for the deposited film were carried out by using the periodic slab geometry. Seven-layer KBr substrate was taken into account, and a vacuum layer whose thickness corresponds to the seven-layer KBr was added between slabs. This allows us to employ a hypothetical three-dimensional periodicity in the calculations of the long-range Coulomb forces with the Ewald method. Although lower four layers were fixed at the bulk position, the lattice constant was allowed to vary in the calculations. The area of a unit block was taken to be 7×7 in a unit of a. Here, a is the bulk lattice constant of KBr. The KBr surface might relax, as KCl grows on the substrate. We have treated this problem by considering a small 1 ML thick KCl island (3×3) on the wider substrate. Even if the lattice constant of the substrate contracts at the interface, this strain might be released at the end of the lattice. The MC calculations were based on the Metropolis algorithms. After 20000 MC steps, 10000 MC steps were done at T=130 K and P=0 Pa to get information on thermal averages.

It was revealed that a two-dimensional island was stable and was not transformed into a three-dimensional one. Recently, Natori *et al.*[19] have studied theoretically the initial stage of heteroepitaxy of the KCl/KBr system and have shown that the two-dimensional configuration is more stable than the three dimensional one, this being consistent with our present simulations. The present results also reproduced the experimental observations for the interatomic distances. The in-plane K–Cl bond was found to be 3.20 Å at the center of the islands, while it was 3.18 Å at the edge of the islands. The difference in the bond length was small. The in-plane K–Cl bond length was significantly larger than the bulk KCl distance (3.15 Å) and was smaller than the bulk KBr distance (3.30 Å). The mean square relative displacements (MSRD) of the bonds at the center and the edge of the islands were 5.5×10^{-3} Å^2 and 11×10^{-3} Å^2, respectively. The large MSRD should originate from the large strain at the edge of the KCl islands. Although the experimental results of MSRD (Table 1) are given as a difference with respect to the standard (bulk KCl), an absolute value can also be determined using a theoretical standard given by FEFF6.[20] The value

obtained was, though the error might be large, 11×10^{-3} Å^2, which is close to the calculated results of the KCl bonds at the edge. Such a large MSRD value observed experimentally may result from a small island size and/or a significant amount of defects.

In the previous section, two possible reasons are shown for the discrepancy between the results of EXAFS and RHEED. In the MC simulations, it was found that at the top layer of the substrate the K–Br distance remained unchanged from the bulk value. This suggests that the former reason of a gradual relaxation of the substrate lattice constant should be excluded. The latter reason might be more probable, which originates from a large number of defects due to significant distortion of the epitaxial films. Conclusively, one can recognize that as in the case of solid solutions, the diffraction technique gives only the averaged structure and erroneous bond distances even in the presence of long-range order.

4.4 Conclusion

Cl K-edge XAFS spectra have been measured to study thickness dependence of local structures of KCl and NaCl thin films grown on NaBr(100). It was suggested from XANES of the KCl/NaBr system that mixed crystals were not formed and but a KCl like film was formed at the interface. Thickness dependence of the bond distance was characterized by EXAFS. The thick KCl and NaCl films show the bulk distance, while in case of thin films the bond distance was slightly shortened for KCl and elongated for NaCl due to some influence of the substrate. As is the case of KCl/KBr system, however, these films did not grow coherently on the substrate. To analyze the structure of the top layer of the substrate, the MC calculation have been also carried out. The experimental results were reproduced within the simple pair-potential approximation and it was elucidated that the bond length of the substrate surface does not change. The local structure does not always correspond to long-range order. It is exemplified that the XAFS technique is useful for studying structures of thin films and interfaces formed of different chemical species.

References

[1] W. E. Mahon, T. Miller, and T. C. Chiang, Phys. Rev. B **54** (1996) 10800.

[2] J. Shen, J. Giergel, and J. Kirschener, Phys. Rev. B **52**, 8454 (1995).

[3] T. Sakamoto, H. Funabashi, K. Ohta, T. Nakagawa, N. Kawai, T. Kojima, and Y. Bando, Superlattice and Microstructures **1**, 347 (1985).

[4] K. Saiki, Y. Nakamura, and A. Koma, Surf. Sci. **250**, 27 (1991).

[5] K. Saiki, Appl. Surf. Sci. **113/114**, 9 (1997).

[6] L. G. Schulz, Acta. Cryst. **4**, 483 (1951).

[7] M. Kiguchi, T. Yokoyama, T. Tsuduki, S. Terada, Y. Kitajima, and T. Ohta, Surf. Sci. in press.

[8] T. Ohta, P. M. Stefan, M. Nomura, and H. Sekiyama, Nucl. Instrum. Methods A **246**, 373 (1986).

[9] M. Funabashi, M. Nomura, Y. Kitajima, T. Yokoyama, T. Ohta, and H. Kuroda, Rev. Sci. Instrum. **60**, 1983 (1989).

[10] Y. Kitajima, J. Elec. Spec. Relat. Phenom. **80**, 405 (1996).

[11] M. Funabashi, T. Ohta, T. Yokoyama, Y. Kitajima, and H. Kuroda, Rev. Sci. Instrum. **60**, 2505 (1989).

[12] See, for instance, *X-ray Absorption: Principles, Applications, Techniques of EXAFS, SEXAFS and XANES*, edited by D. C. Koningsberger and R. Prins (Wiley, New York, 1988).

[13] T. Yokoyama, H. Hamamatsu, and T. Ohta, EXAFSH version 2.1, The University of Tokyo, 1993.

[14] T. Yokoyama, F. Takamatsu, K. Seki, K. Miyake, T. Tani, and T. Ohta, Jpn. J. Appl. Phys. **29**, L1486 (1990).

[15] J. B. Boyce and J. C. Mikkelsen, Jr., Phys. Rev. B **31**, 6903 (1985).

[16] H. Sato, T. Yokoyama, I. Ono, K. Kaneyuki, and T. Ohta, Jpn. J. Appl. Phys. **31**, 1118 (1992).

[17] C. R. A. Catlow, K. M. Diller, and M. J. Norgett, J. Phys. C. **10**, 1395 (1977).

[18] C. Kittel, *Introduction to Solid State Physics*, (Wiley, New York 1988).

[19] A. Natori, A. Tanaka, and H. Yasunaga, Thin Solid Films **281/282**, 39 (1996).

[20] S. I. Zabinsky, J. J. Rehr, A. Ankdinov, R. C. Albers, and M. J. Eller, Phys. Rev. B **52**, 2995 (1995).

Table 1. The results of the EXAFS analysis for the K-Cl and Na-Cl shells as a function of the film thickness *T*. *N*, *R* (Å) and ΔC_2 (10^{-3} Å^2) are the parameters given by the EXAFS experiments. Values in the parameters are the estimated experimental and/or analytical errors.

System	*T*(ML)	*N**	*R*	ΔC_2	Reference
KCl/NaBr	1	4.8(5)	3.04(2)	0.5(10)	This work
	3	4.8(5)	3.07(2)	1.5(5)	
	6	5.7(6)	3.10(2)	1.6(5)	
	20	5.7(6)	3.12(2)	1.8(5)	
Bulk KCl		6	3.13	0.0	
KCl/KBr	1	4.9(5)	3.17(2)	6.4(10)	Ref. 7
	2	4.2(4)	3.16(2)	3.8(5)	
	8	3.4(4)	3.13(2)	1.6(5)	
NaCl/NaBr	1	5.3(5)	2.84(2)	3.3(10)	
	3	4.8(5)	2.83(2)	3.5(5)	
	20	5.2(5)	2.81(2)	1.9(5)	
Bulk NaCl		6	2.80	0.0	

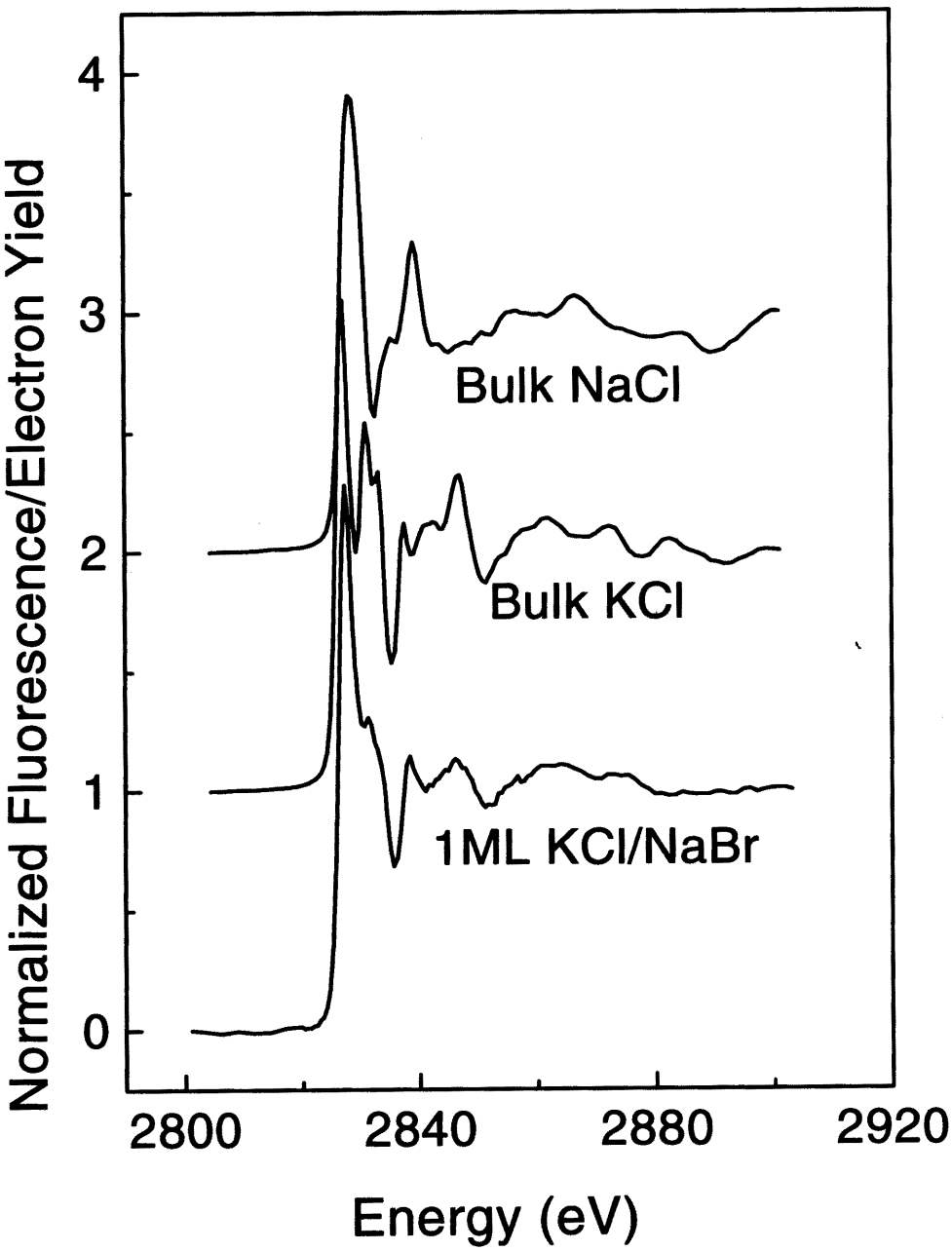

Fig. 1. Cl *K*-edge XANES spectra of bulk NaCl, KCl, and a 1 ML KCl film on NaBr(100). The one of KCl/NaBr(100) was taken at normal x-ray incidence.

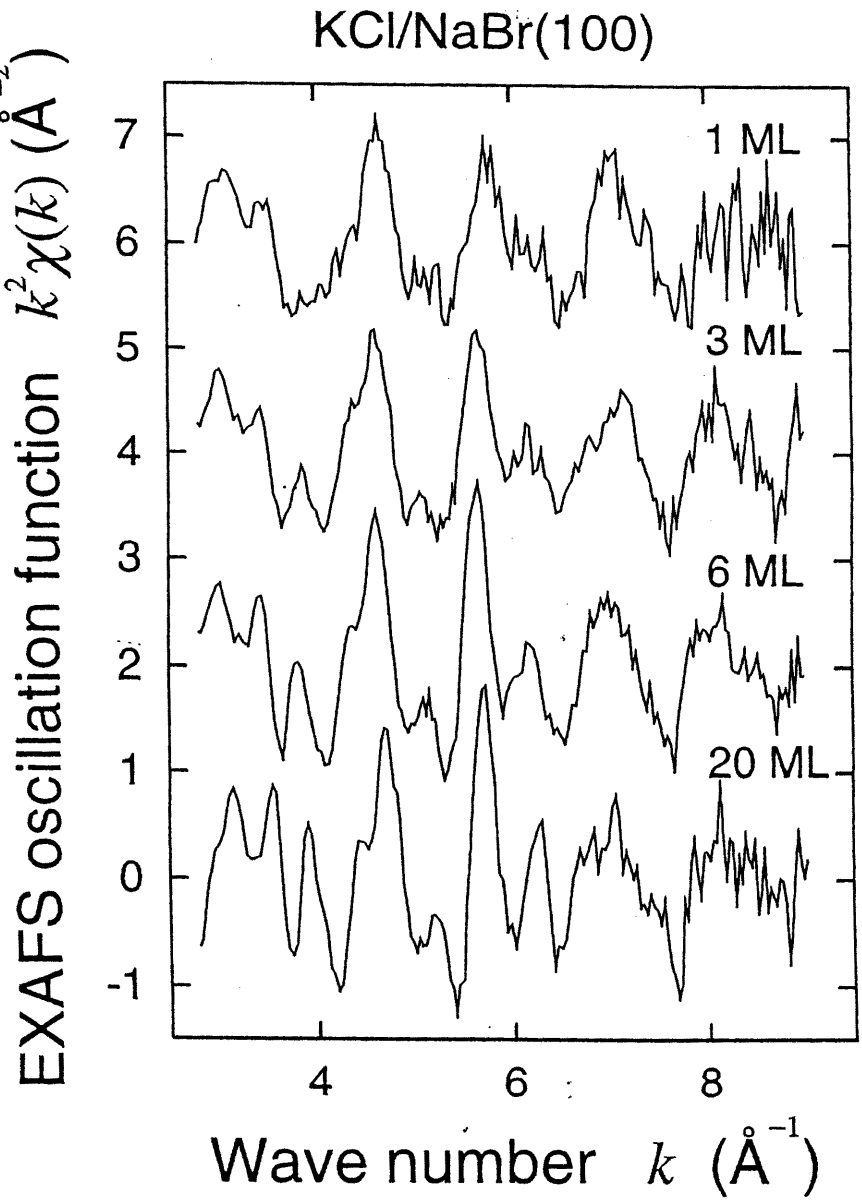

Fig. 2. Cl *K*-edge EXAFS oscillation functions $k^2\chi(k)$ of 1, 3, 6, and 20 ML KCl films on NaBr(100) taken at normal x-ray incidence.

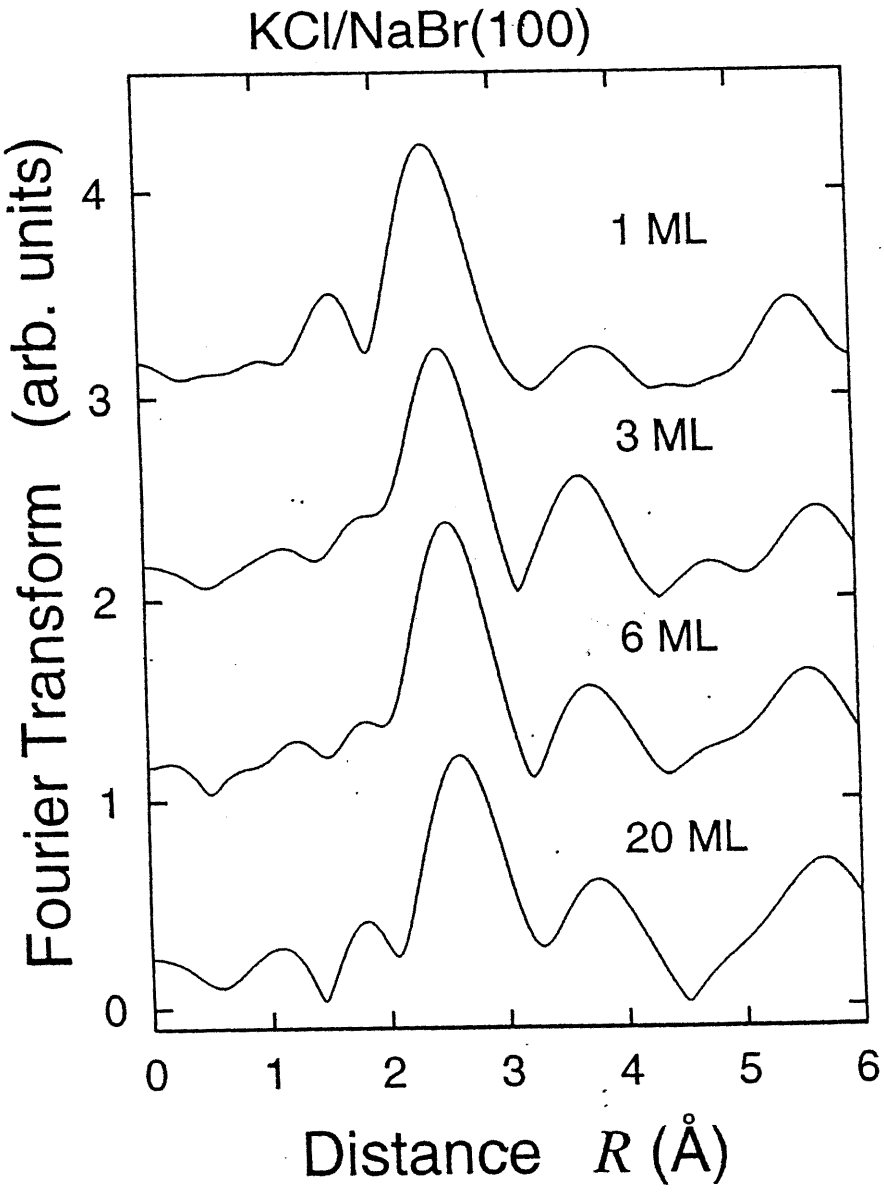

Fig. 3. Fourier transforms of $k^2\chi(k)$ of 1, 3, 6, and 20 ML KCl films on NaBr(100) given in Fig. 2.

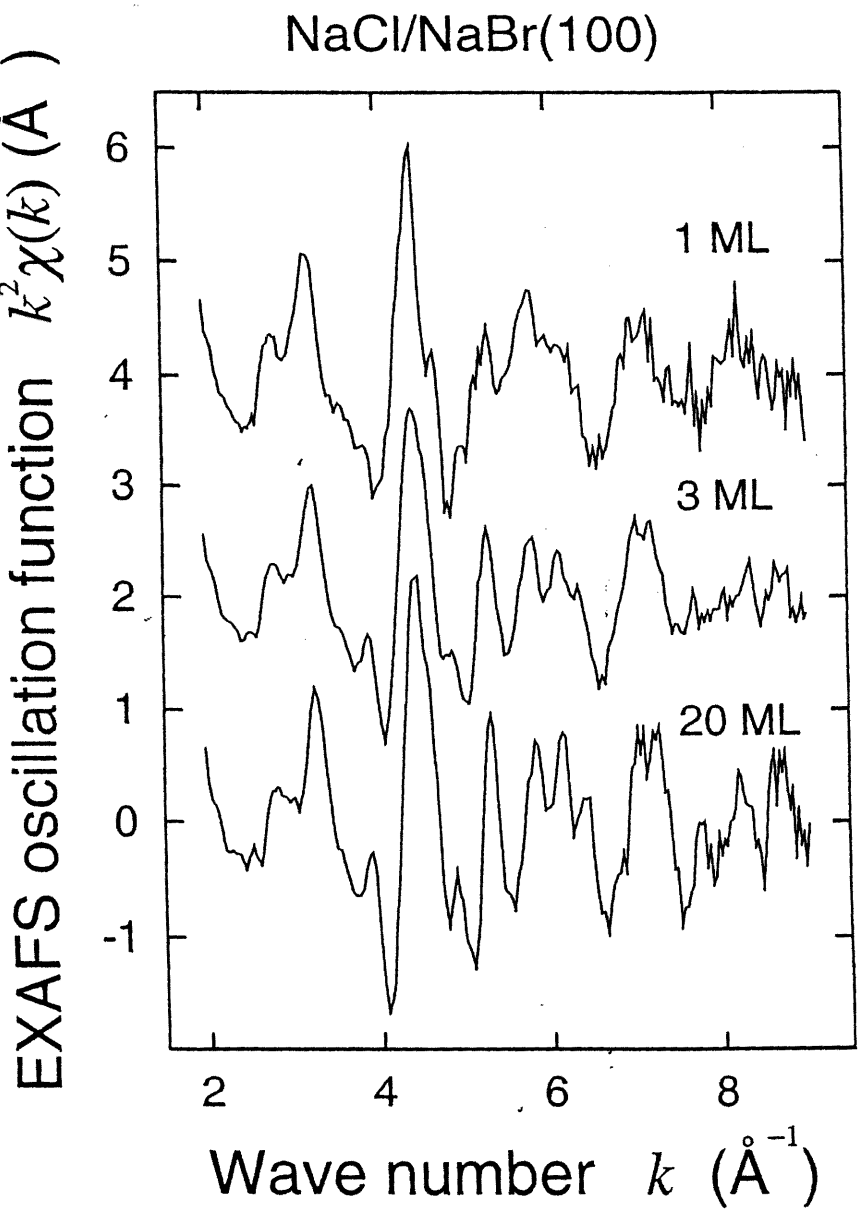

Fig. 4. Cl *K*-edge EXAFS oscillation functions $k^2\chi(k)$ of 1, 3, and 20 ML NaCl films on NaBr(100) taken at normal x-ray incidence.

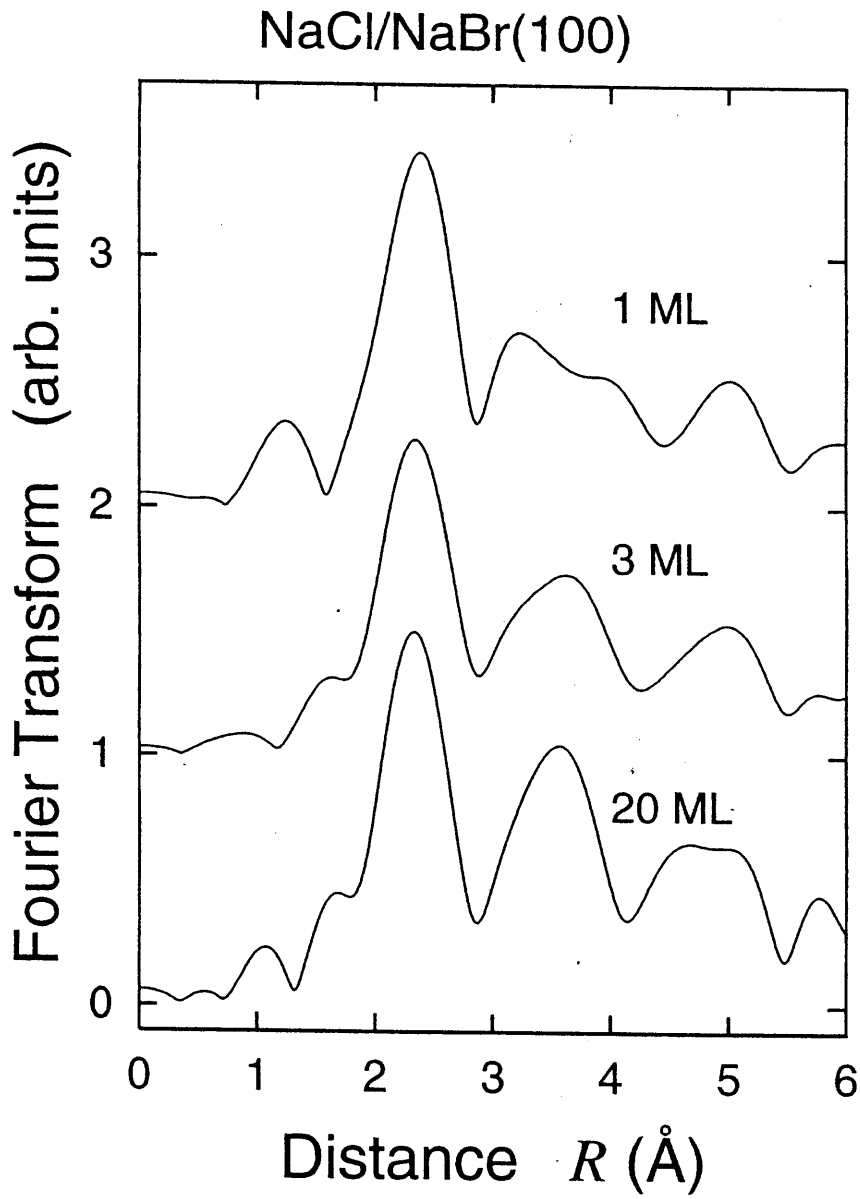

Fig. 5. Fourier transforms of $k^2\chi(k)$ of 1, 3, and 20 ML NaCl films on NaBr(100) given in Fig. 4.

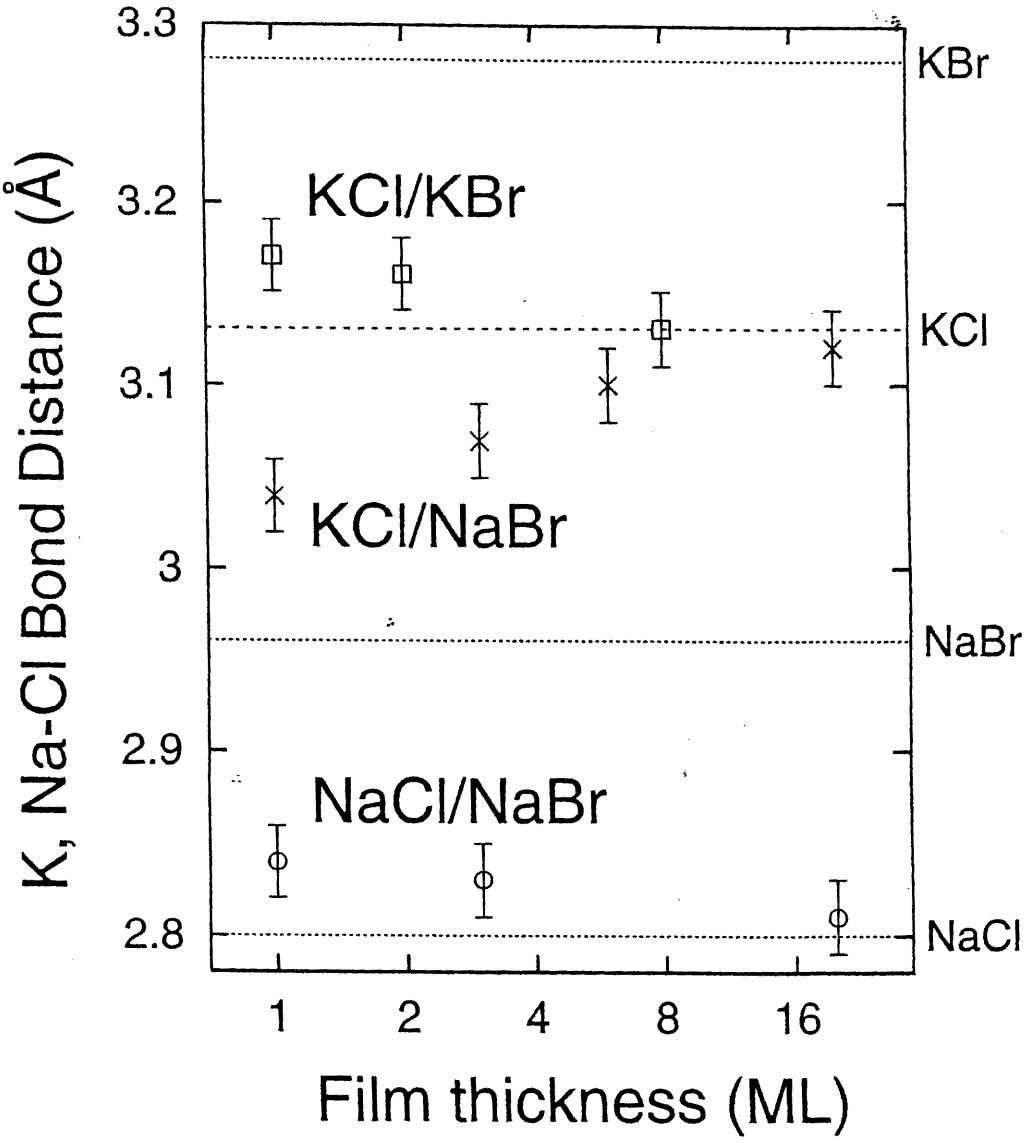

Fig. 6. The K-Cl and Na-Cl bond length as a function of film thickness [KCl/KBr(100) (□), KCl/NaBr(100) (×), and NaCl/NaBr(100) (○)]. Four horizontal lines correspond to the bulk interatomic distance.

5 Surface structures and thermal vibrations of Ni and Cu thin films studied by extended x-ray-absorption fine structure

5.1 Introduction

Enhancement of anharmonic vibration of surface atoms has been an attractive subject since it is believed to be a trigger of surface melting and consequent bulk melting. Anharmonicity is especially important because no melting should occur within harmonic interatomic potentials. In order to investigate huge enhancement of anharmonic vibration and surface melting, several sophisticated techniques such as low-energy electron diffraction (LEED)[1, 2, 3, 4] and ion scattering[5, 6] have been applied. The LEED study[1] revealed that on Ni(100) the surface thermal expansion coefficient rapidly increases between 900 and 1300 K, reaching a value nearly 20 times larger than that in the bulk. The ion-scattering works[6] clarified that the open (110) faces of *fcc* metals like Pb and Al exhibit surface melting; the surface melting point of Pb(110) is approximately 40 K lower than bulk melting point.

Although most of these works have paid attention to long-range order, local structure is also very important since melting occurs through short-range atomic mechanisms.[7] The extended x-ray-absorption fine structure (EXAFS) technique is one of the most suitable method to investigate the dynamical properties of the surface bonds since it provides local information on thermal disorder including anharmonicity. Moreover, polarization-dependent measurements allow one to study vibrational anisotropy. It is, however, rather difficult to record surface EXAFS spectra of metal single crystals because of the presence of huge contribution from bulks. Therefore, except for adsorbate-substrate systems, most previous EXAFS works on surface vibrational properties were devoted to small metal clusters.[8, 9, 10, 11]. By changing the particle size, the thermal vibration and anharmonicity of surface bonds in small metal clusters were actually found to be enhanced significantly. The other techniques such as x-ray diffraction[12] and TEM (transmission electron microscope)[13] were also used for studying thermal properties of small metal clus-

ters. The TEM experiments clarified the decrease in melting temperature for Au clusters.[13]

Since information on vibrational anisotropy cannot directly be obtained from small clusters, studies concerning single crystals are still essential to distinguish the out-of-plane bonds from the in-plane ones. The LEED experiments[1, 2, 3, 4] have clarified significant anisotropy between surface normal and parallel directions. On the other hand, Roubin *et al.*[14] have measured surface EXAFS of monolayer Co deposited on Cu(111) to eliminate the bulk contribution to the surface EXAFS spectra by changing the adsorbate element from the substrate. They have concluded that the out-of-plane Co-Cu bond is again noticeably softer than the in-plane Co-Co one.

In the present study, we have investigated vibrational anisotropy of ultrathin films grown epitaxially on a certain substrate by means of the temperature- and angle-dependent EXAFS technique. The ultrathin films allows us to obtain local information on surface metal-metal bonds without taking care of inequivalent bond natures as in the case of Co/Cu(111). There have been reported several epitaxial metal films; Ag deposited on Si(111) and HOPG (highly oriented pyrolitic graphite) is known to form flat (111) oriented islands.[15, 16, 17] In the case of Ni/HOPG, Baumer *et al.*[18] have reported that the (111) oriented islands are formed at low temperature. Marcus *et al.*[19] has also found for the Cu/HOPG system that even at room temperature Cu films grow on HOPG in a layer-by-layer fashion. In this work, we have thus chosen Cu and Ni ultrathin epitaxial films on HOPG. For further understanding of surface vibrational properties, we have also carried out classical Monte-Carlo (MC) simulations for Cu films using the embedded-atom method (EAM).

5.2 EXPERIMENTAL

A HOPG (ZYA grade) substrate was cleaved with a scotch tape in air and mounted in an ultrahigh vacuum (UHV) chamber. The HOPG was annealed at 1200 K for 1 min to remove contaminations at the surface.[18, 19] After cooling down to 120 K, Ni or Cu was deposited on the clean HOPG. The film thickness and growth rate

were monitored by a quartz crystal oscillator placed near the sample. The absolute and precise thickness was determined by inductivity-coupled plasma (ICP) emission spectrography after all the EXAFS measurements. Although the growth style of Ni or Cu could not be characterized in the present chamber for the EXAFS measurements, LEED observation was carried out in advance using a different chamber employing the same deposition condition. We verified beautiful sixfold spots which implies the growth of (111) oriented epitaxial films.

Ni and Cu K-edge XAFS (x-ray-absorption fine structure) measurements were carried out at the hard x-ray double-crystal monochromator station BL7C and BL12C of Photon Factory in Institute of Materials Structure Science.[20] The fluorescence yield detection method was employed to obtain Ni and Cu K-edge XAFS using a SSD (solid state detector). For the normalization of the fluorescence yield spectra, the intensity of the incident x rays was measured with an ionization chamber filled with pure N_2 as a detection gas. The XAFS spectra were taken at normal (θ=90°) and grazing (θ=30°) x-ray incident angles. At normal x-ray incidence, the electric field vector **E** of the x rays lies parallel to the surface plane and mainly the in-plane bonds contribute to EXAFS, while at grazing x-ray incidence, **E** lies close to surface normal, implying that dominant contribution is of the out-of-plane bonds. The measurements were done at 120, 300, and 420 K. For the measurements at 120 K, the sample crystal was cooled down using a liquid N_2 cryostat. The sample temperature was monitored with a chromel-alumel thermocouple, which was spot-welded on a Ta sheet attached to the sample surface. The temperature fluctuations were less than ±3 K during the XAFS measurements.

5.3 Experimental results

5.3.1 Characterization of Cu thin films

First, we have characterized the structures of the Cu films by LEED. The HOPG misses common orientation with respect to the crystallographic directions within the plane. Thus, the Debye-Scherrer rings were observed instead of spots. After deposition of Cu at 120 K and subsequent annealing to 300 K, clear hexagonal spots appeared. This indicates that (111) oriented Cu islands were formed on the HOPG

as in the previous case of Ag/Si(111).[17] After deposition at low temperature, the film is considered to consist of an assembly of small crystals with a majority of (111)-faced crystals. Such an initial stage may be converted into large crystals (epitaxial film) after annealing.

15 ML (monolayer) Cu was deposited at 120 K, and subsequently annealed to 300 and 420 K. In each step, the XAFS spectrum was measured. Figure 1 shows the change of Cu K-edge XANES (x-ray-absorption near-edge structure) spectra. For comparison, the spectrum of a Cu foil was also displayed in Fig. 1. For bulk *fcc* Cu, two characteristic peaks appear after the absorption edge. Theoretical calculations revealed that they correspond to fourth and higher shell atoms.[9] The absence of the two peaks in the 120 K spectrum indicates that this film does not crystallize so well. After annealing to 300 and 420 K, the characteristic peaks appear, implying the growth of well-defined films.

We will subsequently discuss the crystal growth in terms of structure by using EXAFS. Extraction of the EXAFS functions $\chi(k)$ (k is the photoelectron wave number) was carried out according to the well-established procedures:[25, 26] pre- and post-edge background subtractions and subsequent normalization with the atomic absorption coefficients. The edge energy ΔE_0 was tentatively chosen as an inflection point of the K edges in the 90° spectra. Figures 2 and 3 show, respectively, the $k^2\chi(k)$ functions and corresponding Fourier transforms for the Cu thin film after annealing at various temperature, together with corresponding bulk ones. The k range employed in the Fourier transforms was 3.0–11.0 Å^{-1}. In the Fourier transforms, the dominant peaks at 2.0 Å are ascribed to the first-nearest neighbor (NN) metal-metal coordination. A drastic change has appeared in the 120 K spectrum. A smaller EXAFS amplitude indicates smaller coordination number and larger disorder of the film. The absence of higher shells means that the film does not crystallize completely.

The curve-fitting analysis of the first-NN shells was performed in k space after Fourier filtering (ΔR=1.7–2.8 Å) and inverse Fourier transformation. The backscattering amplitudes and phase shifts for the shells were obtained from the empirical references of bulk Cu. Fitting parameters employed were N^* (effective coordination

number), R (interatomic distance), C_2(mean-square relative displacement) and C_3 (mean-cubic relative displacement). The edge-energy shift ΔE_0 was assumed to be equal to those of the bulks. The numerical results are summarized in Table 1. Although it might not be appropriate to analyze such a disorder system in an usual way, the estimated N^* was 4.7±0.3, which is much smaller than the bulk value of 12, and R was 2.52±0.01 Å, which is also shorter than that of bulk Cu 2.55 Å. The small N^* and R values are also observed for metal small clusters[8, 9, 10, 11, 12, 13]. The films can be regarded as an assembly of small clusters after deposition at low temperature. After annealing the film, N^*, R, C_2, and C_3 converged to the bulk Cu value. We could qualitatively investigate the crystal growth process from the microscopic point of view. Considering the LEED results, it is revealed that the (111) oriented large crystals (films) are formed by deposition at low temperature and subsequent annealing to room temperature.

5.3.2 Thermal vibration of Cu and Ni films

4 ML thick Ni and 4 and 8 ML thick Cu epitaxial films were prepared by deposition at low temperature and subsequent annealing to room temperature. Figures 4 and 5 show, respectively, the $k^2\chi(k)$ functions and corresponding Fourier transforms of them. The curve-fitting analysis of the first-NN shells in the 120 K data was subsequently performed in a similar manner (Δk=2–10 Å^{-1} and ΔR=1.6–2.7 Å for Ni) and the results are summarized in Table 2. C_3 is neglected because of the low-temperature analysis of the well-ordered films.

First of all, we will discuss the effective coordination number N^*. N^* is defined as

$$N^* = 3\sum_{j=1}^{N} \cos^2 \theta_j, \tag{1}$$

where θ_j is the angle between $\mathbf{E}$ and the location vector from the x-ray-absorbing atom to x-ray scattering atom j. An ideal flat 4 ML thick film oriented in the (111) direction would provide $N^*(90°)$=11.3 and $N^*(30°)$=9.2, respectively. We obtained $N^*(90°)$=10.2±0.3 and $N^*(30°)$=8.6±0.3 for the Cu 4 ML film, and $N^*(90°)$=9.2±0.7 and $N^*(30°)$=8.4±0.3 for Ni 4 ML film. Although the absolute value is a little smaller than the expected values, polarization dependence of

N^* [$N^*(90°)>N^*(30°)$] means that the flat (111) oriented films were formed on the HOPG. Slightly smaller N^* and larger C_2 of the films may suggest imperfect flatness due to island formation. Smaller N^* of the Ni film indicates more difficulty in the formation of films than Cu. This is reasonable taking account of the mobilities of Cu and Ni at room temperature (Debye temperatures of 450 K for Ni and 343 K for Cu).

Temperature dependence of the EXAFS spectra for the first-NN shells was subsequently analyzed by means of the curve-fitting method. Figure 6 shows the filtered $k^2\chi(k)$ functions for the first-NN Ni-Ni and Cu-Cu shells. It is clear that with a temperature rise the EXAFS amplitude is reduced and the phase is gradually delayed at high k regions. These phenomena can easily be understood by the third-order cumulant expansion formula of EXAFS

$$k\chi(k) = A_0(k)\exp(-2C_2k^2)\sin\Big(2kR + \phi(k) - \frac{4}{3}C_3k^3\Big), \qquad (2)$$

where $A_0(k)$ and $\phi(k)$ are the amplitude factor and the phase shift, both of which are less temperature dependent. Because of the enhancement of C_2 and C_3 with a temperature rise, the amplitude is suppressed and the phase is gradually delayed. In the present analysis, the low-temperature (120 K) data were used as references. The fitting variables were R, C_2, and C_3 for Cu, while for Ni, C_3 was neglected because it was too small to obtain quantitatively. The qualities of the curve fitting are exemplified in Fig. 7.

The results are tabulated in Table 3. In Table 3, ΔC_2 and ΔC_3 imply the differences in C_2 and C_3 between 120 K and 300 K. Large positive ΔC_2 and ΔC_3 mean large thermal vibrations and anharmonicity. Larger ΔC_2 and ΔC_3 of the films indicate that the effective interatomic potential should be shallower and more anharmonic. The present results are consistent with the results of small clusters; that is, the contraction of the bond length and the enhancement of thermal vibration and anharmonicity were also observed in small clusters.

As concerns the polarization dependence, C_2 and C_3 show larger temperature dependence for θ=30° than for θ=90°, this indicating that the surface out-of-plane bond is softer and more anharmonic than the in-plane bond. The Debye temperature was estimated according to the well-known formula given by Beni *et. al.*[28] The

Debye temperatures for all the shells are also tabulated in Table 3, together with the corresponding bulk value. Although there might be some difference between the cumulants for 30° and 90°, they are unfortunately within the errors.

Let us here argue from the statistical point of view whether the differences in the anisotropic vibration is significant. We employ the ratio of cumulants between 30° and 90°, ΔC_2 of which are 1.18±0.20, 1.14±0.15, 1.02±0.14 for Ni 4ML, Cu 4 ML, and Cu 8ML, respectively, and ΔC_3 of which are 1.23±0.42 and 1.18±0.47 for Cu 4 ML and Cu 8 ML, respectively. If the values are significantly greater than unity, the difference between 30° and 90° data becomes meaningful. The probability density function of true values (τ) can be expressed with the normal Gaussian distribution with the average value (μ) of the measured value and the standard deviation (ρ) of its error. The probability P that the true value τ is located between $\mu-\rho$ and $\mu+\rho$ is given by $P(\mu-\rho<\tau<\mu+\rho)=0.68$, and $P(\tau\leq 1)=0.18$ is thus obtained when μ=1.18 and ρ=0.20 for ΔC_2 of Ni 4 ML. Similarly, we obtain $P(\tau\leq 1)$=0.18 and 0.44 for ΔC_2 of Cu 4 and 8 ML, and $P(\tau\leq 1)$=0.29 and 0.35 for ΔC_3 of Cu 4 and 8 ML. Since each event is independent of each other, $P(\tau\leq 1)$ for all the cases is resultantly estimated to be 0.014 for ΔC_2 and 0.10 for ΔC_3, assuming the perfect correlation among the three data sets of Ni 4 ML and Cu 4 and 8 ML. Moreover, one may permit the correlation between ΔC_2 and ΔC_3 because in a normal interatomic potential anharmonicity is enhanced with the suppression of the harmonic force constant. One can thus estimate the overall $P(\tau\leq 1)$ of 0.0014. We can conclude with the accuracy of 99.86% that the out-of-planar vibration for the surface metal-metal bonds is softer and/or more anharmonic than the in-planar one.

5.4 MONTE-CARLO SIMULATIONS

Classical NPT (closed system, constant pressure, and constant temperature) MC calculations of five-layer Cu were carried out in order to understand the surface vibration more deeply. Desjonquères and Tréglia have already calculated MSRD for various bulk metals and corresponding surfaces for a similar purpose.[29] They used a lattice dynamical model involving central forces between the first- and second-

nearest neighbors and also bending interaction between triplets of first neighbors within the harmonic approximation. For the description of the thermal properties of metals, however, these approximations might sometimes not be sufficient since the metallic bond should be of many body and the anharmonic effect is important. It is worthwhile performing MC simulations to compare the results with our present experiments and their lattice dynamics calculations.

For the description of the interatomic potential, the EAM was employed. In the EAM, the total adiabatic potential energy of the system can be written as a sum of short-range pairwise core-core repulsion and embedding energy for placing an atom into the electron density.[21, 22, 23, 24] The EAM does not require the three-dimensional periodicity and is thus applicable to surfaces as well as alloys and defects. The EAM parameters employed in the present simulations were determined by Foiles *et al.*[24]

Five-layer Cu was taken into account in the NPT MC simulations. Here, two-dimensional periodic boundary condition was imposed for a $12a \times 7\sqrt{6}a = 30.6 \times 30.917$ Å^2 rectangular lattice, where a is the interatomic Cu-Cu distance of 2.55 Å. Each Cu layer contains 168 atoms, and the lowest (fifth) layer was dynamically fixed at the bulk position, although the lattice constant was allowed to vary. The MC calculations were based on the Metropolis algorithms. Initially, 20 000 MC steps were evaluated from the ideal bulk lattice, where each step contains 672 times movements of atoms and one time variation of the lattice constant. After the 20 000 MC steps, 10 000 MC steps were further calculated to get information on thermodynamical averages. The external pressure P was assumed to be 0 Pa, and the temperatures were set to be 120 and 300 K.

The second- and third-order cumulants C_2 and C_3 given by the present EAM-MC calculations are summarized in Table 4. Here, Cu1, Cu2, and Cu3 denote the Cu atoms in the first, second, and third layers, respectively. Cu1-Cu1 means the in-plane bond in the first layer, while Cu1-Cu2 the out-of-plane bond between the first and the second layer. For comparison, the experimental and previous calculation results of bulk Cu[30] are also tabulated. We included the results of quantum mechanical calculations and those of the classical calculations. For a quantitative comparison of

the present classical MC results with the experimental ones, the contribution of zero point vibrations is required, this indicating a slight underestimation of C_2 especially at low temperature and thus overestimation of ΔC_2 between 120 and 300 K.

As given in Table 4, the values of C_2 and C_3 of in-plane bonds like Cu1-Cu1 are large at the surface and decrease as they go into the bulk and converge to the bulk value at the third layer. Such increases in thermal vibrations of in-plane bonds are consistent with large ΔC_2 and ΔC_3 observed experimentally in the normal incidence spectra. As concerns the anisotropy of the thermal vibrations of the Cu-Cu bonds, C_2 of the out-of-plane bonds (Cu1-Cu2) is larger than that of in-plane bonds (Cu1-Cu1 and Cu2-Cu2). This agrees with the experimental results whereby the bonds observed experimentally at grazing incidence are softer and more anharmonic than the ones at normal incidence. We could reproduce the experimental results qualitatively, and show that the bonds between the first and second layers are especially soft.

The lattice dynamic calculations by Desjonquères and Tréglia[29] have demonstrated that C_2 of the out-of-plane bond is not very sensitive to the nature of the metal or to the crystallographic orientation of the surface. They found the relation as C_2(Cu1-Cu2)$\sim$1.14$\times C_2$(bulk Cu-Cu). In contrast, C_2 of the in-plane bond is much closer to the bulk value although it depends on metals. They obtained the relation like C_2(Cu1-Cu1)$\sim$1.03$\times C_2$(bulk Cu-Cu) for Cu(111). On the other hand, our classical MC results were ΔC_2(Cu1-Cu2)=1.16$\times\Delta C_2$(bulk Cu-Cu) and ΔC_2(Cu1-Cu1)=1.10$\times\Delta C_2$(bulk Cu-Cu). Note here that the value of ΔC_2(bulk Cu-Cu) used is the classical one to match the present MC calculations. The present results agree with the experiments and the previous lattice dynamics calculations[29] at least qualitatively. Although we obtained more enhanced surface vibrations than those by Desjonquères and Tréglia, we can conclude that thermal vibrations of the out-of-plane bonds are more enhanced than those of the in-plane ones. The quantitative differences might originate from differences of models, potentials, or quantum effects.

5.5 Discussion

Although the vibrational anisotropy has been studied for various kinds of adsorbate-substrate systems,[14, 31, 32, 33] no unified conclusions have been obtained. As mentioned in Sec. 5.1, Roubin *et al.*[14] have showed that in the Co/Cu(111) system the surface out-of-plane (Co-Cu) bond is softer than the in-plane (Co-Co) one. On the contrary, Wenzel *et al.*[31, 32] have revealed that in the N/Ni(100)-p4g(2×2) system the in-plane N-Ni bond is softer than the out-of-plane one. More recently, Yokoyama *et al.*[33] have studied systematically the thermal vibrations of the first- and second-NN bonds for S/Ni(100)-c(2×2) and S/Ni(110)-c(2×2). They have suggested a simple argument that the longer bond simply provides softer and more anharmonic vibrations than the shorter ones; in S/Ni(100), the first-NN S-Ni bond (R_1=2.19 Å) directed in the in-plane direction is stiffer than the out-of-plane second-NN one (R_2=3.12 Å), while in S/Ni(110) the first-NN out-of-plane bond (R_1=2.19 Å) is stiffer than the in-plane second-NN nearest bond (R_2=2.27 Å). Although this simple concept can explain the above vibrational anisotropy of Co/Cu(111) and N/Ni(100) systems, it is not clear whether the in-plane and out-of-plane bonds show the same vibrational properties if their bond distances are equivalent. In the present study, we have studied anisotropic vibrational properties of ultrathin films, we have revealed that the out-of-plane bond is softer than the in-plane bond even if the bond distance is not different.

Let us here estimate the vibrational amplitudes of the in-plane and out-of-plane bonds quantitatively using the present EXAFS results. We can suppose that only the in-plane bond in the first layer and the bond between the first and second layers show different vibrational amplitudes from the bulk ones, while all the other bonds are of bulk Cu. This assumption is based on the above MC results; the thermal vibrations of Cu1-Cu1 and Cu1-Cu2 are different from those of bulk ones. Let us define $C_2^{\rm si}$, $C_2^{\rm so}$, and $C_2^{\rm b}$ as the MSRD of Cu1-Cu1, Cu1-Cu2, and the other Cu-Cu bonds, respectively. The C_2 value observed experimentally can be given as

$$C_2(m,\theta) = \frac{(C_2^{\rm so} + 6C_2^{\rm si})\sin^2\theta + 4C_2^{\rm so}\cos^2\theta + 4C_2^{\rm b}(m-2)}{4m - 4 + 3\sin^2\theta}, \qquad (3)$$

where m and θ are the film thickness and x-ray incidence angle, respectively. By

using experimental results of ΔC_2 given in Table 3, we can obtain each component as $\Delta C_2^{so} = (7.0 \pm 1.4) \times 10^{-3}$ Å^2, $\Delta C_2^{si} = (4.5 \pm 0.9) \times 10^{-3}$ Å^2, and $\Delta C_2^{b} = (4.1 \pm 0.4) \times 10^{-3}$ Å^2. The corresponding Debye temperatures are Θ_D^{so}=262(25) K, Θ_D^{si}=322(30) K, and Θ_D^{b}=335(5) K, respectively, which are depicted in Fig. 8. The Debye temperature of bulk Cu is 343 K by calorimetric measurements,[27] and 338 K by EXAFS. Our present result of Θ_D^{b}=335(5) K indicates high reliability of the present model.

Moreover, we can estimate the relations as

$$\Delta C_2^{so} = 1.71 \times \Delta C_2^{b} \quad \text{and} \quad \Delta C_2^{si} = 1.10 \times \Delta C_2^{b}.$$

The lattice dynamics calculations[29] gave

$$\Delta C_2^{so} = 1.14 \times \Delta C_2^{b} \quad \text{and} \quad \Delta C_2^{si} = 1.03 \times \Delta C_2^{b},$$

while our MC results gave

$$\Delta C_2^{so} = 1.16 \times \Delta C_2^{b} \quad \text{and} \quad \Delta C_2^{si} = 1.10 \times \Delta C_2^{b}.$$

These two calculations seem to underestimate the surface vibrations and anisotropy compared to the present experimental results. Note here that the surface Debye temperature of Cu(100) determined by LEED is 235 K,[3] which is still lower than the present result of 262 K. We can suppose that the reason for larger ΔC_2 and ΔC_3 observed experimentally is that theoretical calculations treat perfects films, while the actual films contain many defects and some roughening might occur already at room temperature, as is evident from smaller N^* and larger C_2. Since the surface area becomes wider in the presence of defects, the surface Debye temperature would effectively be lowered.

We can further compare the present results with those of ultrafine particles. The thermal vibrations of metal surfaces have been studied for small metal clusters.[8, 9, 10, 11, 12, 13] The increase in the thermal vibration and anharmonicity have been

observed with a decrease in cluster size. The decrease in the Debye temperature is caused by softening of the metal-meal vibrational frequencies. Harada *et al.*[12] have studied the mean-square displacements for Au small clusters as a function of a cluster size by using x-ray diffraction. They also assumed that the particle is composed of the core and shell. They have shown that when the thickness of the shell is assumed as one atomic layer, Θ_D(core)=165 K and Θ_D(shell)=97 K are in good agreement with the reported values of Θ_D(bulk)=168 K and Θ_D(shell)=83 K, the latter of which was determined by LEED.

5.6 CONCLUSION

Angular- and temperature-dependent Cu and Ni K-edge EXAFS spectra of 4 and 8 ML Cu and 4 ML Ni grown epitaxially on HOPG have been measured and analyzed in order to investigate the dynamical properties of the surface metal-metal bonds. It was revealed that thermal vibration and local thermal expansion of metal-metal bond are larger for the films than for their corresponding bulk metals and the relative motions focused on the surface local bonds are enhanced in the surface normal direction. In the present study, by changing x-ray incidence angle and film thickness, we could separate the thermal vibrations of the surface in-plane and out-of-plane and bulk bonds, and discuss the bond character quantitatively. For further understanding of thermal vibrations, we have done classical Monte-Carlo calculations for the Cu film and revealed that the out-of-plane bond between the first and second layer is very weak.

References

[1] A. U. MacRae, Surf. Sci. **2**, 52 (1964).

[2] Y. Cao and E. Conrad, Phys. Rev. Lett. **65**, 2808 (1990).

[3] S. Müller, A. Kinne, M. Kottcke, R. Metzler, P. Bayer, L.Hammer, and K. Heinz, Phys. Rev. Lett. **75**, 2859 (1995).

[4] K. Pohl, J. H. Cho, K. Terakura, M. Scheffler, and E. W. Plummer, Phys. Rev. Lett. **80**, 2853 (1998).

[5] A. W. Denier van der Gon, R. J. Smith, J. M. Gay, D. J. O'connor, and J. F. van der Veen, Surf. Sci. **227**, 143 (1990).

[6] J. W. M. Frenken, and J. F. van der Veen, Phys. Rev. Lett. **54**, 134 (1985).

[7] E. A. Stern, P. Līviņš, and Z. Zhang, Phys. Rev. B **43**, 8850 (1991).

[8] A. Balerna, E. Bernieri, P. Picozzi, A. Reale, S. Santucci, E. Burattini, and S. Mobilio, Phys. Rev. B **31**, 5058 (1985).

[9] P. A. Montano, G. K. Shenoy, E. E. Alp, W. Schulze, and J. Urban, Phys. Rev. Lett. **56**, 2076 (1986).

[10] G. Apai, J. F. Hamilton, J. Stöhr, and A. Thompson, Phys. Rev. Lett. **43**, 165 (1979).

[11] T. Yokoyama, S. Kimoto, and T. Ohta, Jpn. J. Appl. Phys. **28**, L851 (1989).

[12] J. Harada and K. Ohshima, Sur. Sci. **106**, 51 (1981).

[13] P. Buffat and J. Borel, Phys. Rev. A **13**, 2287 (1976).

[14] P. Roubin, D. Chandesris, G. Rossi, J. Lecante, M. C. Desjonquères, and G. Tréglia, Phys. Rev. Lett. **56**, 1272 (1986).

[15] F. Patthey and W. D. Schneider, Phys. Rev. B **50**, 17560 (1994).

[16] F. Patthey and W. D. Schneider, Surf. Sci. **334**, L715 (1995).

[17] G. Neuhold and K. Horn, Phys. Rev. Lett. **78**, 1327 (1997).

[18] M. Bäumer, J. Libuda, and H. J. Freund, Sur. Sci. **327**, 321 (1995).

[19] P. Marcus and C. Hinnen, Surf. Sci. **392**, 134 (1997).

[20] M. Nomura and A. Koyama, *X-ray absorption fine structure*, edited by S. S. Hasnain, (Ellis Horwood, Chichester, 1991) p.667.

[21] M. S. Daw and M. I. Baskes, Phys. Rev. B **29**, 6443 (1984).

[22] S. M. Foiles, Phys. Rev. B **32**, 3409 (1985).

[23] S. M. Foiles, Phys. Rev. B **32**, 7685 (1985).

[24] S. M. Foiles, M. I. Baskes, and M. S. Daw, Phys. Rev. B **33**, 7983 (1986).

[25] See, for instance, *X-ray Absorption: Principles, Applications, Techniques of EXAFS, SEXAFS and XANES*, edited by D. C. Koningsberger and R. Prins (Wiley, New York, 1988).

[26] T. Yokoyama, H. Hamamatsu, and T. Ohta, EXAFSH version 2.1, The University of Tokyo, 1993.

[27] C. Kittel, *Introduction to Solid State Physics*, (Wiley, New York, 1988).

[28] G. Beni and P. M. Platzman, Phys. Rev. B **14**, 1514 (1976).

[29] M. C. Desjonquères and G. Tréglia, Phys. Rev. B **34**, 6662 (1986).

[30] T. Yokoyama, Phys. Rev. B **57**, 3423 (1998).

[31] L. Wenzel, J. Stöhr, D. Arvanitis, and K. Baberschke, Phys. Rev. Lett. **60**, 2327 (1988).

[32] L. Wenzel, D. Arvanitis, H. Rabus, T. Lederer, K. Baberschke, and G. Comelli, Phys. Rev. Lett. **64**, 1765 (1990).

[33] T. Yokoyama, H. Hamamatsu, Y. Kitajima, Y. Takata, S. Yagi, and T. Ohta, Surf. Sci. **313**, 197 (1994).

Table 1. Structural parameters determined by EXAFS for the Cu 15 ML films.

Temperature(K)	N^*	R (Å)	$\Delta C_2(10^{-3}$ Å$^2)$	$\Delta C_3(10^{-4}$ Å$^3)$
120	4.7(3)	2.52(1)	3.8(4)	5.5(7)
300	8.3(3)	2.55(1)	1.6(2)	2.3(4)
420	10.8(4)	2.55(1)	1.2(4)	2.0(4)

Table 2. The EXAFS results for the first-NN metal-metal shells in the 4ML Ni film and the 4 and 8 ML Cu films.

System	Angle	N^*	R (Å)	$C_2(10^{-3}$ Å$^2)$
Ni 4 ML	90°	9.2(7)	2.47(2)	5.8(3)
	30°	8.4(3)	2.47(1)	5.8(2)
Ni bulk		12	2.47	3.2
Cu 4ML	90°	10.2(3)	2.54(1)	5.6(3)
	30°	8.6(3)	2.53(1)	5.8(3)
Cu 8 ML	90°	10.9(3)	2.54(1)	5.2(2)
	30°	10.4(4)	2.54(1)	5.8(3)
Cu bulk		12	2.55	4.0

Table 3. The results of the temperature-dependent EXAFS analysis for the first-NN metal-metal shells in the 4 ML Ni films and the 8 ML Cu films.

System	angle	$\Delta C_2(10^{-3}$ Å$^2)$	$\Delta C_3(10^{-4}$ Å$^3)$	θ_D(K)
Ni 4 ML	90°	3.5(4)		366(20)
	30°	4.0(4)		345(15)
Ni bulk		2.6		416
Cu 4ML	90°	4.4(4)	3.1(6)	325(15)
	30°	5.0(5)	3.8(8)	307(15)
Cu 8 ML	90°	4.3(4)	2.3(4)	328'15)
	30°	4.4(4)	2.7(6)	325(15)
Cu bulk		4.0	1.4	338

Table 4. Cumulants for the Cu-Cu shell in Cu 4 ML film at 120 and 300 K estimated from the MC simulations. The experimental and calculated values for bulk Cu are also given for comparison. All the quantities of C_2 are in units of 10^{-3} Å^2 and those of C_3 are in the 10^{-4} Å^3 unit.

	ΔC_2	C_2	C_2	ΔC_3	C_3	C_3
4 ML Cu films						
Classical MC						
Cu1-Cu1	5.64	3.47	9.11	2.12	0.34	2.46
Cu2-Cu2	5.43	3.23	8.66	1.99	0.17	2.16
Cu3-Cu3	5.00	2.94	7.94	0.88	0.22	1.10
Cu1-Cu2	5.94	3.67	9.61	2.15	0.47	2.62
Cu2-Cu3	5.33	3.13	8.46	1.71	0.17	1.88
Experimental						
90°	4.4			3.1		
30°	5.0			3.8		
fcc Cu bulk						
classical	5.14	3.21	8.35	1.48	0.26	1.74
quantum	4.61	4.19	8.80	1.48	0.26	1.74
Exp.	4.03	4.00	8.03	1.4		

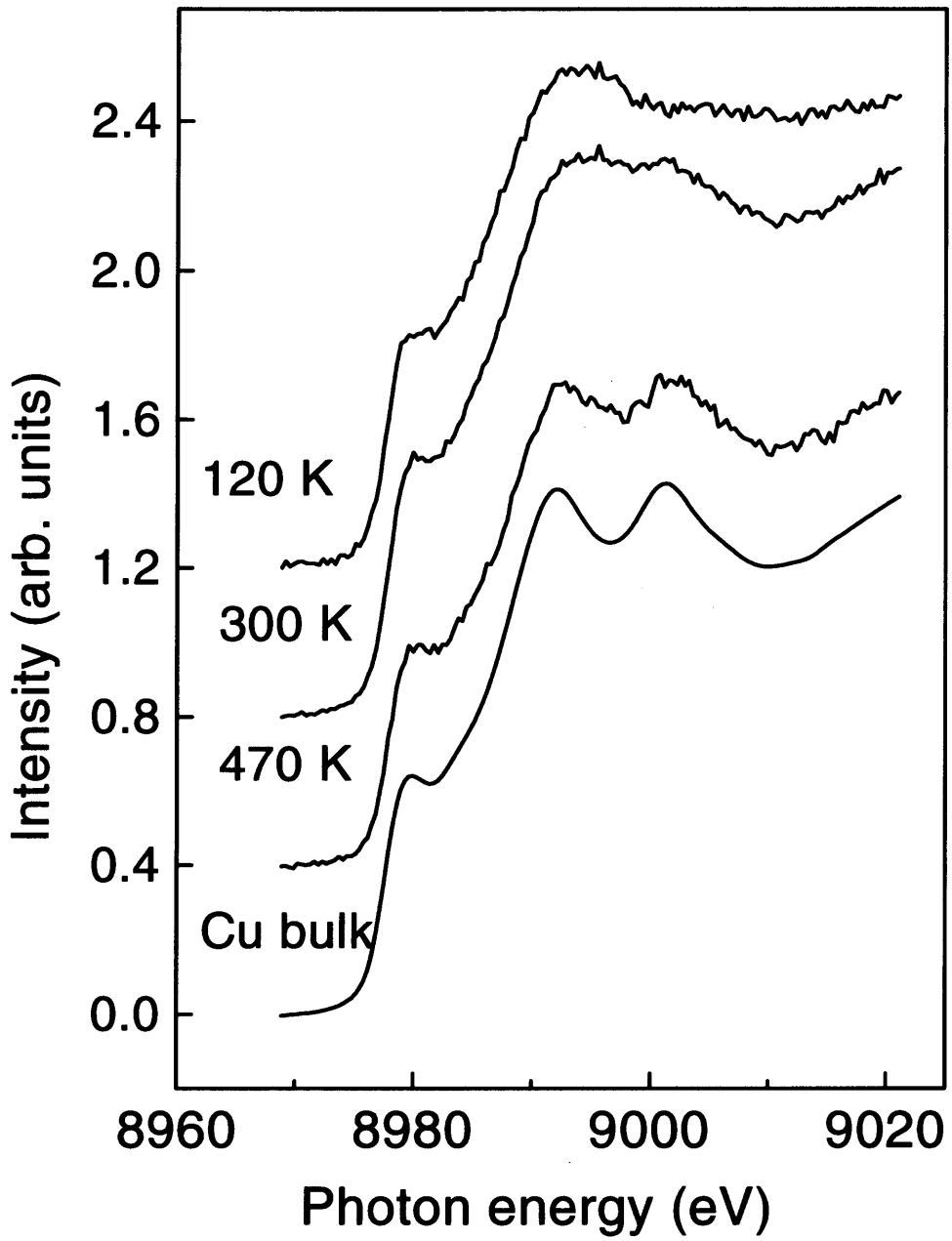

Fig.1. Cu *K*-edge XANES spectra of the Cu 15 ML film annealed at 300 K and 470 K, and a Cu foil.

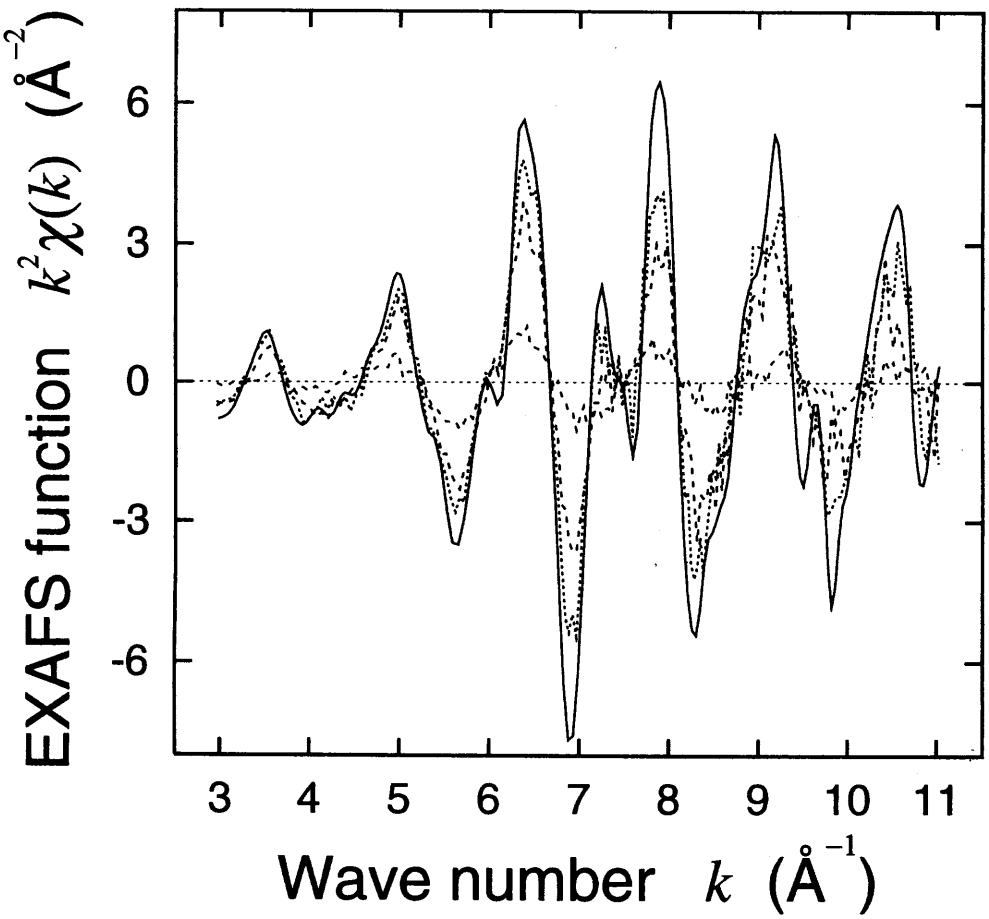

Fig. 2. Cu *K*-edge EXAFS oscillation functions $k^2\chi(k)$ of the Cu 15 ML film annealed at 120 (long-dashed line), 300(short-dashed line), 420 K (dotted line) taken at normal x-ray incidence, and of the Cu foil (solid line).

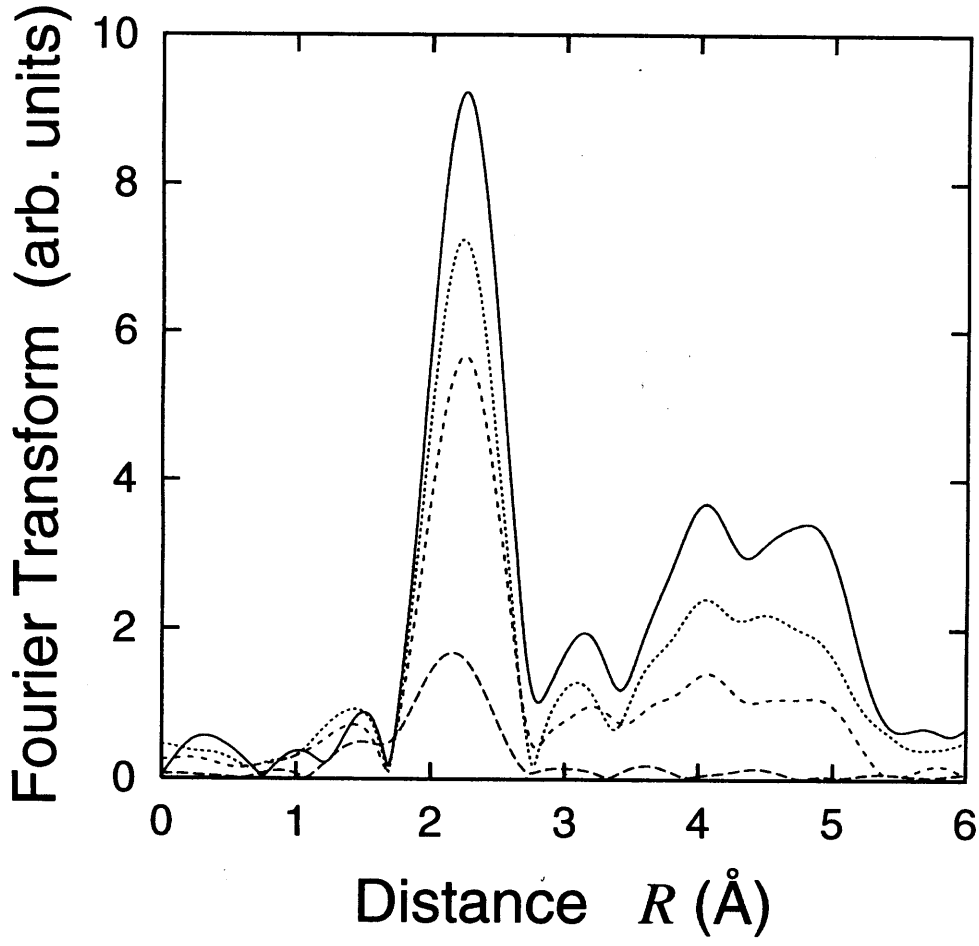

Fig. 3. Fourier transforms of $k^2\chi(k)$ of Fig. 2

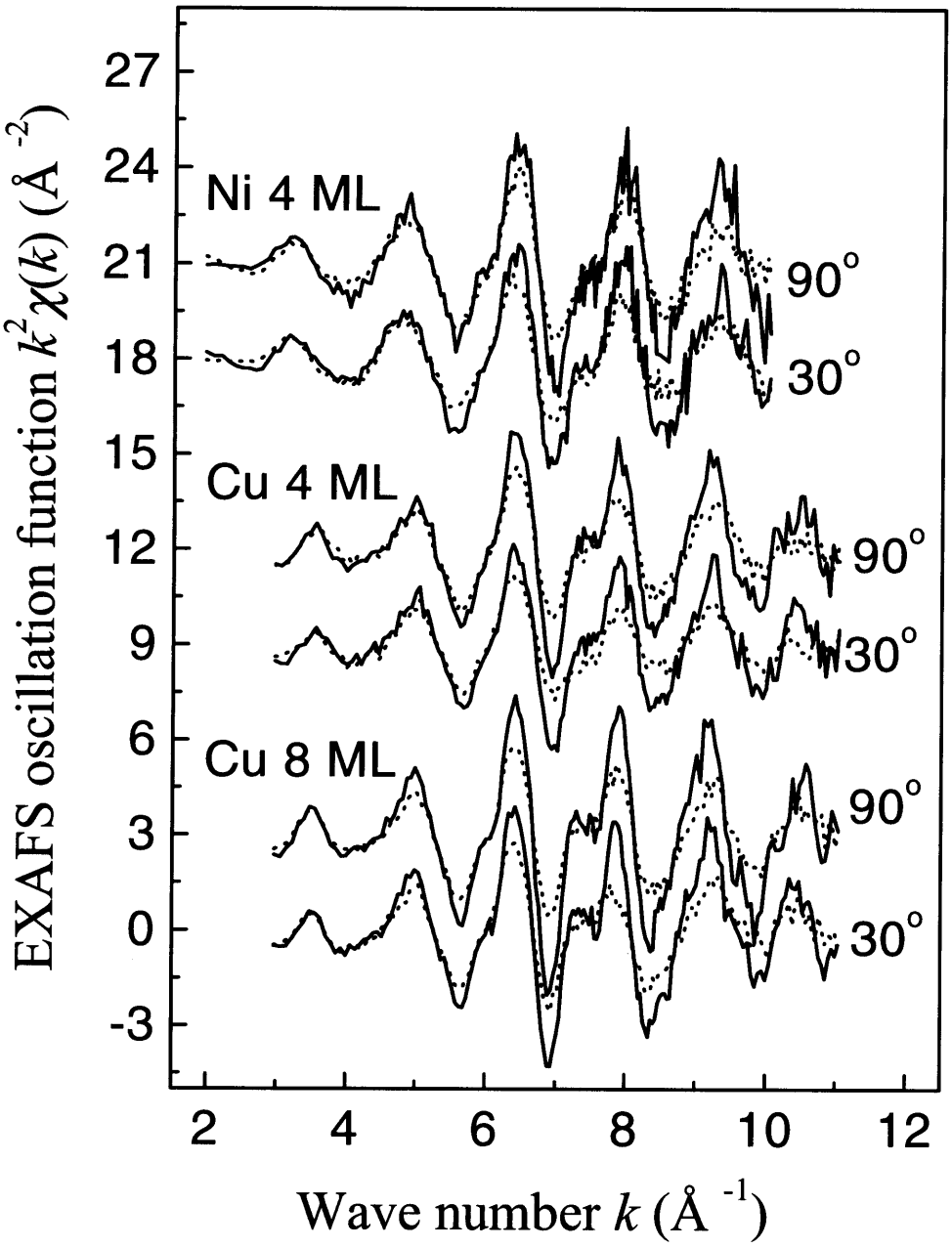

Fig. 4. Ni and Cu *K*-edge EXAFS oscillation functions $k^2\chi(k)$ of the Ni 4 ML and Cu 4 ML and 8 ML films measured at grazing (30^0) and normal (90^0) x-ray incidences at 120 (solid line) and 300 K (dotted line).

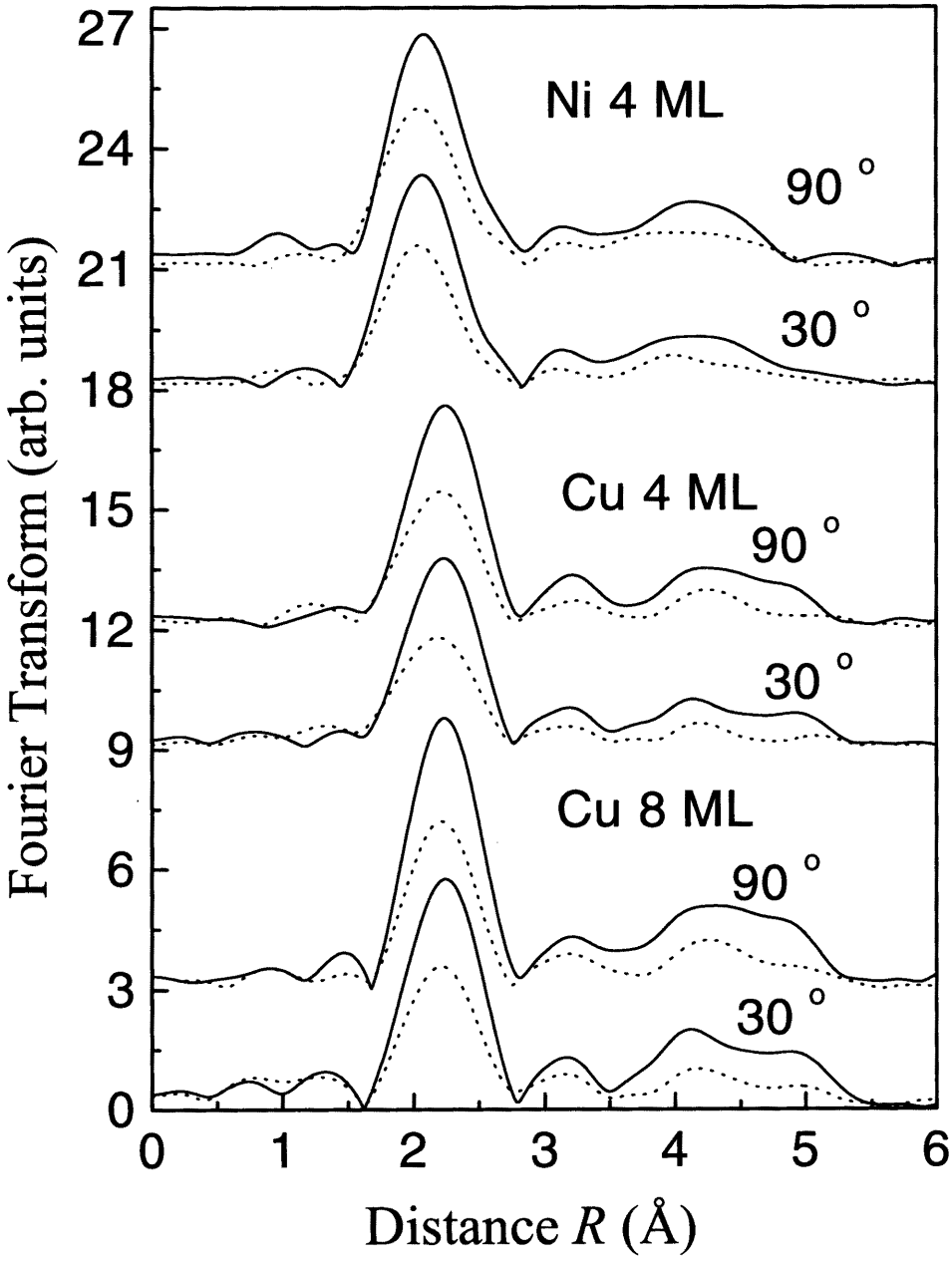

Fig. 5. Fourier transforms of $k^2\chi(k)$ of Fig. 4.

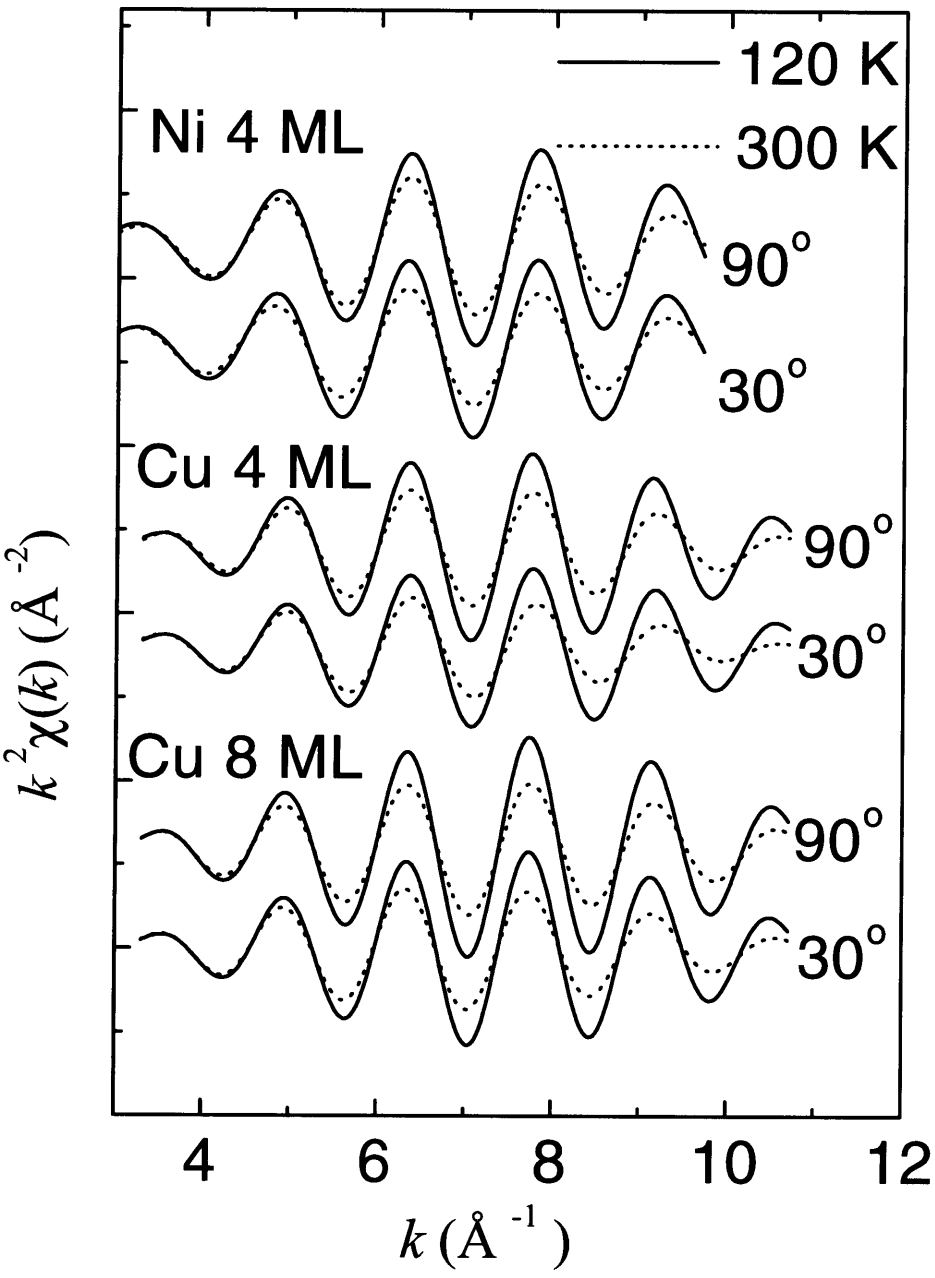

Fig. 6. Filtered EXAFS oscillation functions $k^2\chi(k)$ of the first-NN contributiuons at 120 (solid line) and 300 K (dotted line) for 30° and 90° x-ray incidences. .

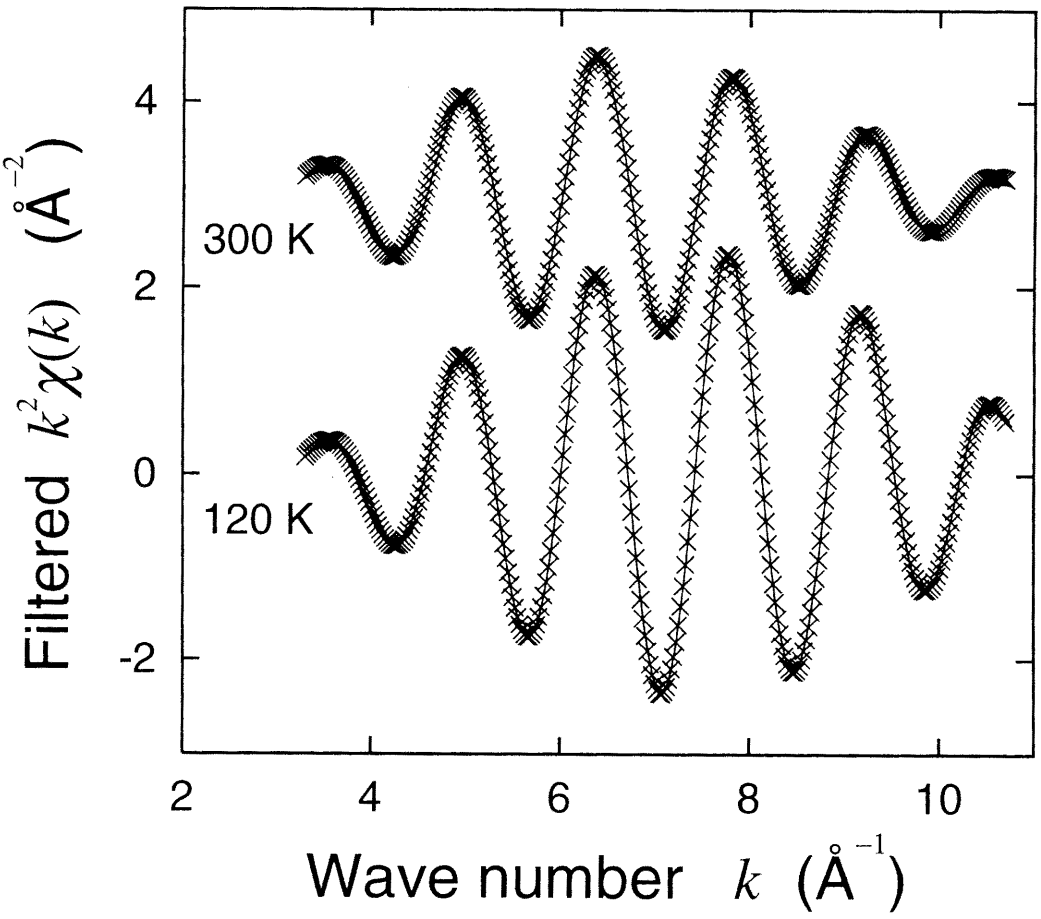

Fig. 7. Examples of the curve-fitting analysis for the first-NN Cu-Cu shells, which are obtained for the 4 ML Cu film measured at the x-ray incident angle of 30° at a temperature of 120 and 300 K. The filtered EXAFS oscillation function $k^2\chi(k)$ are given as cross, while the fitting results are as solid lines.

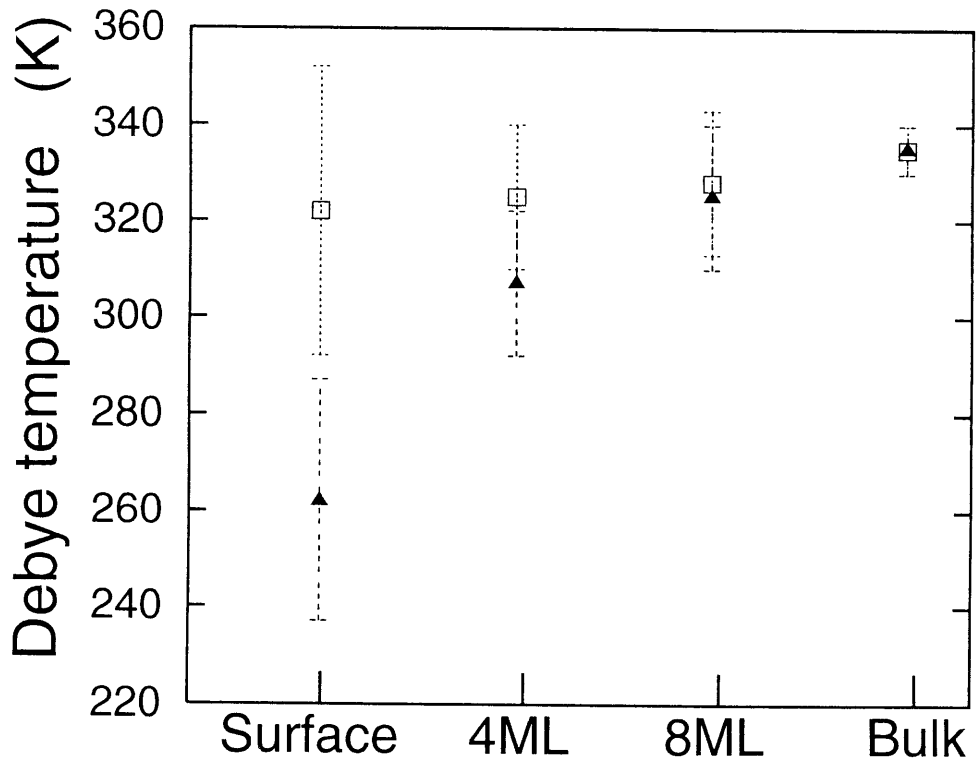

Fig. 8. Effective Debye temperature of the surface Cu atoms, 4 and 8 ML Cu films, and bulk Cu. The out-of-plane and in-plane ones are given as closed triangles and open squares, respectively.

6 Anisotropic anharmonic vibrations of the surface S-Ni and Cl-Ni bonds in c(2×2)S and Cl/Ni(100) systems studied by molecular dynamics

6. 1 Introduction

It was previously believed from diffraction studied such as low energy electron diffraction (LEED) that the surface vibrations and anharmonicity are enhanced in the vertical direction because of the absence of upper atoms leaving the lateral interaction less modified [1]. The diffraction technique, however, give information only in absolute displacements of surface atoms with respect to a certain fixed coordinate, and it is thus difficult or in general impossible to discuss the anisotropic vibrational properties of the surface chemical bonds such as adsorbate-substrate interactions.

In contrast, surface extended X-ray-absorption fine structure (SEXAFS) provides information on relative displacements between X-ray-absorbing and scattering atoms, and is more suitable to investigate dynamical properties of local bondings. SEXAFS studies [2-7] have reveled interesting properties of anisotropic and anharmonic vibrations of surface chemical bond. Recently we investigated the dynamical properties of the surface S-Ni bonds in the c(2×2)S/Ni(100) and Ni(110) systems [6], and found that in the S/Ni(110) system where S is coordinated by five Ni atoms (four surface Ni and one second layer Ni), the lateral S-Ni bond (surface layer Ni) is significantly softer and more anharmonic than the vertical S-Ni bond (second layer Ni). On the other hand, in the case of c(2×2)S/Ni(100) the lateral S-Ni (surface Ni) interaction was found to be stiffer than the vertical one (second layer Ni). By comparing other SEXAFS findings for p4g(2×2)N/Ni(100) [4] and $\sqrt{2}\times 2\sqrt{2}$ R45°O/Cu(100) [5], it was concluded that the strength of surface chemical bonds does not depend on the bond direction and that more distant bond simply provide softer and more anharmonic vibration than the closer ones.

The next step for more detailed understanding of anisotropy in the surface chemical

bonds is to clarify the relationship between absolute and relative displacements which are, respectively, given by LEED and SEXAFS. These quantities are different from each other in the presence of chemical bondings because of correlated motions. Recently, Yang *et. al.* [8] investigated anisotropy of surface bonds in the c(2×2)O and S/Ni(100) by means of lattice dynamics calculations within the harmonic approximation and found that the O atom vibrates more freely in the vertical direction while the S atom moves more significantly along the lateral direction. They ascribed such a different anisotropic property to a geometric factor and an adsorbate-adsorbate interaction.

Although the lattice dynamics calculation is a powerful technique in which the qunatum-mechanical effect is included, it is rather complicated to apply this method to anharmonic vibrations. For such a purpose, computer simulation seems to be more convenient by means of the molecular dynamics (MD) calculation. Some applications of MD simulations to EXAFS have been performed so far; experimental EXAFS spectra for liquid Hg and Ga were found to be successfully reproduced within the classical MD method when the multiple-scattering contributions were taken into account [9, 10].

In the present study, we have carried out classical MD simulations of tthe c(2×2)S/Ni(100) and Cl/Ni(100) systems in order to obtain information on anisotropic and anharmonic vibration of surface chemical bonds. The obtained results have been compared to those given by our previous SEXAFS studies [6, 7] and by high-resolution electron energy loss spectroscopy (HREELS) [11]. Anisotropic behaviors of the absolute and relative displacements including anharmonicity are consequently discussed in detail.

6. 2 Calculational procedures

6. 2. 1 Interatomic potential

Prior to classical MD calculations, the interatomic potential should be at first determined. The potential energy was assumed as a sum of pairwise interatomic interactions, which depend only on the distance r_{ij} between atoms i and j, and higher-order interactions were neglected. For a Ni-Ni potential the literature data [12] were used, while S-S and Cl-Cl interactions were determined by the *ab initio* SCF/MP2 MO

(molecular orbital theory based on the self-consistent field and the second order Moller Plesset perturbation) calculations using Gaussian92. The Gaussian basis sets of S and Cl were, respectively, of triple- and double-zeta qualities [13].

The adsorbate-substrate interactions of S-Ni and Cl-Ni were obtained by the first-principle quantum-mechanical calculations, which was based on the density functional theory (DFT) for the cluster model. The calculations were done by employing the DFT qunatum mechanical code DMOL version 950 of Biosym/MSI using the double numerical basis functions with polarization and local spin density functions as the atomic basis set. All the inner core levels were frozen in these calculations.

The cluster models used for the Ni(100) surface were composed of 25 Ni atoms, among which 16 atoms were in the top atomic layer and nine were in the second layer. The coordination of the atoms and all the Ni-Ni distances were taken to be the same as in the bulk metal, this implying the assumptions of unrelaxed and unreconstructed surfaces. In the calculations for the adsorbate-deposited surface, one S or Cl atoms was placed on the central fourfold hollow site, as shown in Fig.1. By fixing tthe positions of the metal atoms, we calculated the total energies of the cluster as a function of the height of the adsorbate atom. The S(Cl)-Ni layer spacing Z was varied between 0.2 and 9.0 Å.

In order to express the pairwise potential between S(Cl) and Ni, we assumed that the total energy which contains not only the first-nearest neighbor (NN) S(Cl)-Ni interactions but all the other higher-NN ones can be fitted by a linear combination of Morse potential $V(r)$ (r is the S, Cl-Ni distance) given as

$$V(r) = D_e\left\{\exp\left[-\frac{2(r-r_e)}{a}\right] - 2\exp\left[-\frac{(r-r_e)}{a}\right]\right\} \qquad (1)$$

where D_e is the dissociation energy, a the potential stiffness, and r_e the equilibrium distance. Figure 1 shows total energy plot of the $Ni_{25}S$ cluster against the Ni-S distance Z. A fitted curve is also shown in the figure. The three Morse parameters listed in Table 1 are used in the following MD calculations. Similar results were obtained for the $Ni_{25}Cl$ cluster, the Morse parameter being also given in Table 1.

6. 2. 2 Molecular dynamics

In simulating the equilibrium structural and thermodynamic properties of the system at a desired temperature T and a pressure P, we used the combined methods of the constant-temperature MD proposed by Nose [14] and Martyna *et al.* [15] and the constant-pressure MD by Parrinello and Rahman [16] for anisotropic crystals with any spatial symmetry. The Verlet algorithm was used for the calculation of the atomic motion. T and P were controlled by scaling atom velocities and a basic cell parameter under the periodic boundary condition. In the present case, only the directions parallel to the surface were assumed to be periodic. Since the pressure was taken into consideration, this calculation could treat thermal expansion of the system, which is essentially important for vibrational anharmonicity.

The MD basic cell was assumed to consider five layer of Ni (45 atoms) and one layer of S or Cl (10 atoms) on both sides of the surface, as shown in Fig. 2. After reaching the equilibrium, we sampled the simulated data for 20000 fs with a time step of 0.4 fs. The temperatures examined T_1 and T_2 were T_1=120 K and T_2=295 K for the S/Ni(100) system and T_1=100 K and T_2=300 K for Cl/Ni(100). The pressure P was fixed at 0. These values correspond to the experimental conditions.

6. 3 Results and Discussion

6. 3. 1 Comparison with the SEXAFS cumulants

Let us first recall the structural parameters obtained by the EXAFS analysis. In the case of weakly anharmonic systems, the EXAFS function $\chi(k)$ (k is the photoelectron wavenumber) for a single shell can be given as

$$\chi(k) = A_0(k)\exp\left[-2C_2k^2\right]\sin\left[2kR_{av} + \phi(k) - \frac{4}{3}C_3k^3\right] \qquad (2)$$

where $A_0(k)$ and $\phi(k)$ are, respectively, the amplitude function and the phase shift. R_{av} is the average interatomic distance C_2 and C_3 are, respectively, the second- and third-order cumulants, which are defined as $C_2 = \left\langle\left\langle (R - R_{av})^2 \right\rangle\right\rangle$ and $C_3 = \left\langle\left\langle (R - R_{av})^3 \right\rangle\right\rangle$, where

implies thermal and static averages and R is the instantaneous distance C_2 and C_3 correspond to mean square and cubic relative displacements, respectively. Once $A_0(k)$ and $\phi(k)$ are given theoretically or empirically, R, C_2 and C_3 are obtained by the curve fitting of the experimental $\chi(k)$ with eq. (2). Although the absolute values of C_2 and C_3 are difficult to obtain from experimental data directly because of some uncertainly in $A_0(k)$ and $\phi(k)$, the temperature difference of these quantities, ΔC_2 and ΔC_3, are given with high accuracy since temperature dependence of $A_0(k)$ and $\phi(k)$ should usually be by far smaller than those of C_2 and C_3. C_3 should vanish in the case of entirely harmonic vibration. According to the ergodic theory, the thermal average is assumed to be equivalent to the time average, and the cumulants calculated in the present MD calculations can directly be compared with those given by EXAFS.

Let us next discuss the MD results. Figures 3 and 4 show the simulated time evolutions of the interatomic distances between the central adsorbate atom A (A=S, Cl) and the first-NN (Ni1) and second-NN (Ni2) atoms, respectively, for the c(2×2)S and c(2×2)Cl/Ni(100) systems at $T= T_1$ and T_2. In both figures, it is clear that the vibrational amplitude of the A-Ni2 pair is larger and its frequency is lower than those of the A-Ni1 one due to the absence of a direct chemical bond between atom A and the second-NN Ni2. With a temperature rise, the vibrational amplitudes for both the A-Ni1 and A-Ni2 pairs are found to get larger. It is also found that the difference between the A-Ni1 and A-Ni2 vibrations is more significant in the S/Ni(100) case than in the Cl/Ni(100) one.

The temperature difference of the cumulants ΔC_2 and ΔC_3 given by the present MD and the previous SEXAFS studies are tabulated in Table 2, together with the average distance R_{av} at $T=T_1$. In the MD calculations the cumulants for the A-Ni1 pair were evaluated by taking time averages amongst four equivalent first-NN A-Ni1 bonds. In both systems, the calculated results are found to agree excellently with the experimental results. We can thus recognize that the present results of the MD simulations can approximately be applied to the following discussions.

It is rather surprising to obtain such good agreement in spite of the fact that the present MD calculations were based on the classical mechanics assuming simple two-

body interatomic potentials. This may be because of ionic or metallic natures of the chemical bonds examined (S-Ni, Cl-Ni, and Ni-Ni). These chemical bonds provide less angular dependence in contrast to covalent bonds, leading to less importance of many-body interactions. In the case of covalent material such as Si ad H_2O, the bond angle defined by a three-body force is known to be important, and the present simple two-body model could not be applied and should essentially be modified.

6. 3. 2 Absolute and relative displacements

Let us next separate the absolute and relative motions in surface normal and parallel directions using the present MD results. The projected mean-square (absolute) displacements $<<\Delta u^2>>$ of the S, Cl, Ni1 and Ni2 atoms at T= T_2 are listed in Table 3. Here higher temperature data employed in order to reduce the qunatum effect, Δu_X is defined as the X component (parallel; X//[110]) of the displacement with respect to the equilibrium position, while Δu_Z correspond to the Z component (normal; Z//[001]). Both the S and Cl atoms exhibit enhanced vibrational amplitudes in the Z direction, this being consistent with LEED concept. It is also noted that the vibrational amplitudes of adsorbates S and Cl are more significant than those of Ni mainly due to lighter atomic weights of S and Cl.

Table 3 also gives the projected mean-square relative displacement $<<\Delta R^2_X>>$, $<<\Delta R^2_Z>>$, $<<\Delta R_X \Delta R_Z>>$ and C_2 of the A-Ni1 bonds at T= T_2. These quantities are defined as

$$\left\langle\left\langle \Delta R_X \Delta R_Z \right\rangle\right\rangle = \left\langle\left\langle \left(\Delta R_X \overline{R_0}\right)\left(\Delta R_Z \overline{R_0}\right) \right\rangle\right\rangle$$

$$C_2 = \left\langle\left\langle \left(\Delta R \overline{R_0}\right)^2 \right\rangle\right\rangle \quad \Delta R=\Delta R_X+\Delta R_Y+\Delta R_Z \qquad (3)$$

and so forth. Here, $\overline{R}_0$ implies the unit vector directed from A to a certain Ni atom. In Fig. 5, $<<\Delta R^2_X>>$ and $<<\Delta R^2_Z>>$ are schematically depicted assuming that atom A is located at the origin. In contrast to the above $<<\Delta u^2>>$ results, the relative motion of the Cl-Ni1 bond is more enhanced in the X direction, while that of the S-Ni1 one is larger in

the Z direction. Larger negative values of $<<\Delta R_x \Delta R_Z>>$ imply a negative correlation between the lateral and vertical motions, as indicated above. In both S and Cl cases, sums of the mean-square absolute displacements $<<\Delta u^2_A>>+<<\Delta u^2_{Ni}>>$ (A-S, Cl) are significantly larger than the mean-square relative displacements $<<\Delta R^2_{A\text{-}Ni}>>$, implying noticeable correlated motions of the adsorbate-substrate bonds.

It is thus found in Table 3 and Fig. 5 that in the case of S the vertical motion $<\Delta R^2_Z>$ is significantly larger than the parallel one $<\Delta R^2_X>$, while in the Cl case the vertical motion is as large as the parallel one. This can be understood from a simple geometrical consideration. Because of the distance difference, the S-Ni1 bond is more flat than the Cl-Ni1 bond; using the local geometries obtained in the MD calculations, the polar angles ω with respect to surface normal are 53° and 49° for S-Ni1 and Cl-Ni1, respectively. When certain adsorbate-Ni bond is elongated from R to $R+\Delta R$ leaving the bond direction unchanged the parallel and vertical components of the displacement should be given as $\Delta R \cos\omega$ and $\Delta R \sin\omega$, respectively. This implies that the vertical motion is enhanced more easily for the S-Ni1 bond than for the Cl-Ni1 one. It is conclusively remarked that the direction of the adsorbate-substrate vibration is dependent on local geometrical structure, although there have been conflicting discussion on whether the vertical displacement of the surface adsorbate-substrate bond is larger than the parallel one as in the case of mean-square absolute displacements of surface atoms.

Yang *et. al* [8] concluded by means of the lattice dynamics calculations on c(2×2)O and S/Ni(100) that S(O) moves more freely in the parallel (vertical) direction. These findings are inconsistent with our present results for S/Ni(100). This discrepancy should originate from the different potential parameters employed. They introduce a number of potential parameters so that the surface phonon dispersion could be reproduced well. They compared the evaluated C_2 of c(2×2)S/Ni(100) with those of the SEXAFS results given by Sette *et. al* [3]. The C_2 values for the first- and second-NN S-Ni shell given by Sette *et. al* are, however, discrepant noticeably from ours. Systematic comparison of the C_2 values with our other systems [7] indicates that our results are more reasonable than

those by Sette *et. al.* These experimental discrepancies should affect the different potential parameters since Yang *et. al.* [8] determined those values semiempirically. In contrast, our potential parameters employed were given nonempirically. We can thus recognize that our values are more reliable since the present MD calculations explain the experimental SEXAFS results satisfactorily. It should be, however noted that the qualitative trend proposed by Yang is consistent with the present one whereby the larger polar angle of the adsorbate-substrate bond indicates the larger vibrational amplitude in the vertical direction.

6. 3. 3 Fourier analysis of the time evolution

Vibrational frequencies corresponding to the adsorbate-substrate bonding are obtainable by performing Fourier transformation of the time evolution for adsorbate-substrate distance. Figure 6 and 7 show the Fourier transforms for the A-Ni1 and A-Ni2 interatomic distances at $T = T_1$ (given in Figs. 3 and 4), together with those of the X and components for the A-Ni1 pairs. Here the lower temperature data were chosen because of higher resolution in the Fourier transform. The resonance frequencies of Cl/Ni(100) are in general shifted to a lower frequencies than those of S/Ni(100) because of weaker adsorbate-substrate bonds. When one compares the X and Z components between S and Cl/Ni(100), the X motion compared to the Z one is found to be more enhanced in Cl/Ni(100), as obtained in Fig. 5 and Table 3.

The HREELS study for the c(2×2)S/Ni(100) system was previously carried out and the resonance frequencies were known including their dispersions. The total symmetric S-Ni stretching mode was observed at 350 cm^{-1} (Γ point), and the two low-frequency mode were found at 110 cm^{-1} (S_4 mode) and 150 cm^{-1} (so-called "surface resonance" mode) in the vicinity of the X point. In the present MD simulations for the S/Ni(100) system (Fig. 6) the corresponding resonances are seen at 105, 150, and 350 cm^{-1} for the total S-Ni1 and S-Ni2 spectra, implying excellent agreement with the HREELS spectra. On the other hand, in the case of the c(2×2)Cl/Ni(100) system, only the total symmetric Cl-Ni stretching frequency is known as 282 cm^{-1}, which corresponds to the resonances

appearing around 280 cm^{-1} in Fig. 7, though the Fourier transforms show complicated dispersions.

Table 5 gives the resultant phase for the three vibrational modes (105, 150 and 350 cm^{-1}) in S/Ni(100). The 105 cm^{-1} mode shows the antiphase between the X and Z components of the S-Ni1 motion. Correspondingly, as shown in Fig. 6, the 105 cm^{-1} feature appears noticeably for both the X and Z components, while it is suppressed in the total motion. This implies that the vibrations is ascribed to the bending mode leaving the S-Ni1 bond length unchanged, which looks like an opening and closing motion of an umbrella. This is also the case for 150 cm^{-1} mode, where the S-Ni2 motion coincides the Z component of the S-Ni1 motion. On the other hand, the 350 cm^{-1} resonance in Fig. 6 is found in all the spectra including the total one of the S-Ni1 motion. The phases of the total and the X and Z components for the S-Ni1 pair coincide, as found in Table 5. The 350 cm^{-1} mode can be thus be ascribed to the symmetric stretching vibration. These assignments for the three resonances are consistent with the previous ones [11]. Similar discussion can be adopted to the Cl/Ni(100) case. The higher-frequency resonances were found to consist of the Cl-Ni1 stretching motion, while the low-frequency ones can be assigned to the bending modes.

The HREELS study [11] has clarified the phonon dispersions of the c(2×2)S/Ni(100) system. The S_4 mode exhibits a dispersion of acoustic phonons in the range of 0-110 cm^{-1} (from Γ to X), and the S-Ni stretching mode gives dispersions in 350-315 cm^{-1} (Γ to X) for the parallel motion and in 350-380 cm^{-1} (Γ to X) for the vertical motion. In the present MD simulations, however, it is difficult to discuss the dispersions especially for low frequency phonons because the basic cell of the present MD simulations was too small. Several frequencies concerning the S-Ni stretching motions were nevertheless found in the range of 350-410 cm^{-1} in Fig. 6. This might correspond to the observed dispersion, though the moment of the phonons were not obtained quantitatively.

6. 4. Conclusion

Using simple pairwise potentials and the classical MD, the vibrational properties concerning the surface adsorbate-substrate bonds were reproduced well in the c(2×2)S and Cl/Ni(100) system; the second- and third-order cumulants agree with those given by SEXAFS, and the vibrational frequencies are also consistent with the HREELS data. It should be emphasized that no empirical parameters were used in the present simulations. Although LEED and SEXAFS provide information on mean-square absolute and relative displacements, respectively, the whole surface vibrational properties cannot be described with either methods.

The MD calculations give both quantities separately and moreover the anisotropic properties. The present study has demonstrated the usefulness of the MD methods for the discussion on surface vibrations including anharmonicity. In both systems, the mean-square absolute displacements of the adsorbates are found to be noticeably greater in the normal direction than in the lateral ones. It is, on the contrary, revealed that concerning the adsorbate-substrate bonds the parallel motion of Cl-Ni1 pair in the Cl/Ni(100) system is as large as the vertical one, while the parallel motion of the S-Ni one is more suppressed in S/Ni(100). Such a difference is ascribed to the difference of the local surface geometries.

The present success of the MD simulations is owed to satisfactory estimations of the two-body interatomic potentials by means of the qunatum-mechanical calculations. When the system is not covalent like S and H_2O only two body interactions can describe the dynamical properties rather appropriately, indicating that the determination of the pairwise potentials might be exclusively potentials. In the present case, the cluster size was found to be essential to obtain appropriate potentials; when smaller clusters such as ANi_5 or ANi (A=S, Cl) were assumed in the qunatum-mechanical calculations, the potential stiffness and/or the equilibrium distance were erroneously estimated and the resultant physical quantities disagreed with the experimental findings.

References

[1] See, for instance, J. B. Pendry: Low Energy Electron Diffraction (Academic, London, 1974).

[2] P. Roubin, D. Chandesris, G. Rossi. J. Lecante, M. C. Desjonquères and G. Tréglia, Phys. Rev. Lett. **56**, 1272(1986).

[3] F. Sette, C. T. Chen, J. E. Rowe and P. H. Citrin, Phys. Rev. Lett. **59**, 311 (1987).

[4] L. Wenzel, J. Stöhr, D. Arvanitis and K. Baberschke, Phys. Rev. Lett. **60**, 2327 (1988).

[5] T. Lederer, D. Arvanitis. G. Comelli, L. Tröger and K. Baberschke, Phys. Rev. B **48**, 15390 (1993).

[6] T. Yokoyama, H. Hamamatsu, Y. Kitajima, Y. Takata, S. Yagi, and T. Ohta, Surf. Sci. **313**, 197 (1994).

[7] M. Tischer, P. Srivastava, H. Wende, K. Baberschke, T. Yokoyama, S. Terada, M. Sakano, Y. Kitajima, and T. Ohta, Surf. Sci. **371**, 409 (1997).

[8] L. Yang, T. S. Rahman, and D. L. Mills, Phys. Rev. B **42**, 2864 (1990).

[9] A. Di Cicco and A. Filipponi, J. Non-Cryst. Solids **156-158**, 102 (1993).

[10] L. Ottaviano, A. Filipponi, A. Di Cicco, S. Santucci and P. Picozzi, J. Non-Cryst. Solids **156-158**, 112 (1993).

[11] S. Lehwald, M. Rocca, H. Ibach and T. S. Rahman, Phys. Rev. B **31**, 3477 (1985).

[12] F. Milstein, J. Appl. Phys. **44**, 3825 (1973)

[13] H. Horn, R. Ahlrichs and H. Ehring, Chem. Phys. Lett. **183**, 227 (1991).

[14] S. Nose, J. Chem. Phys. **81**, 511 (1984).

[15] G. J. Martyna, D. J. Tobias and M. L. Klein, J. Chem. Phys. **101**, 4177 (1994).

[16] M. Parrinello and A. Rahman, Phys. Rev. Lett. **45**, 1196 (1984).

Table 1. Morse parameters of interatomic potentials of S-Ni, Cl-Ni, Ni-Ni, S-S and Cl-Cl pairs. The Ni-Ni one was taken from the literature [12], while the other ones were obtained in the present *ab initio* calculations.

Pair	D_e (eV)	R_e (Å)	a (Å)
S-Ni	1.31	2.22	0.67
Cl-Ni	0.867	2.35	0.674
Ni-Ni	0.219	2.53	0.402
S-S	10.1	2.05	0.873
Cl-Cl	5.75	2.19	0.727

Table 2. Results of $R_{av}(T_1)$ and $\Delta C_2(T_1, T_2)$ and $\Delta C_3(T_1, T_2)$ obtained by the MD simulations (this work) and the previous SEXAFS experiments for the c(2×2)S/Ni(100) [6] and Cl/Ni(100) [7] surfaces.

		R_{av} (Å)		ΔC_2 (10^{-3} Å^2)		ΔC_3 (10^{-4} Å^3)	
Surface	Pair	MD	SEXAFS	MD	SEXAFS	MD	SEXAFS
S/Ni(100)	S-Ni1	2.20	2.19(2)	2.9	3.0(3)	0.9	1.2(2)
	S-Ni2	3.07	3.13(3)	9.8	9.0(5)	7.4	8.0(5)
Cl/Ni(100)	Cl-Ni1	2.32	2.35(2)	3.7	4.4(3)	1.9	2.6(3)
	Cl-Ni2	3.27	3.13(3)	5.1	5.2(12)	4.1	5.3(15)

Table 3. Components of mean-square displacements Δu^2(A), Δu^2(Ni1) and Δu^2(Ni2) and mean-square relative displacements ΔR^2(A-Ni1) for c(2×2)A/Ni(100) (A=S, Cl) at $T=T_2$, obtained by the MD simulations. "X.Z" and "Total" for ΔR^2 (A-Ni1) represent $<\Delta R_X \Delta R_Z>$ and C_2, respectively. All the quantities are in units of 10^{-3} Å^2.

Surface		Δu^2(A)	Δu^2(Ni1)	Δu^2(Ni2)	ΔR^2(A-Ni1)
S/Ni(100)	X	4.9	2.3	3.5	4.5
	Z	10.72	7.7	6.8	12.4
	X.Z				-3.4
	Total	20.4	12.3	13.8	5.5
Cl/Ni(100)	X	9.4	4.4	4.5	8.6
	Z	11.8	7.4	5.9	8.8
	X.Z				-1.2
	Total	30.6	16.2	14.9	5.76

Table 4. Phase of the vibrational motions of the S-Ni1 and S-Ni2 pairs and of the X and Z components of the S-Ni1 pair. The MD calculations were carried out at T_1=120 K.

Resonance	S-Ni1	S-Ni1(X)	S-Ni1(Z)	S-Ni2
105 cm^{-1}	73	75	-105	56
150 cm^{-1}	127	-62	122	122
350 cm^{-1}	44	45	40	45

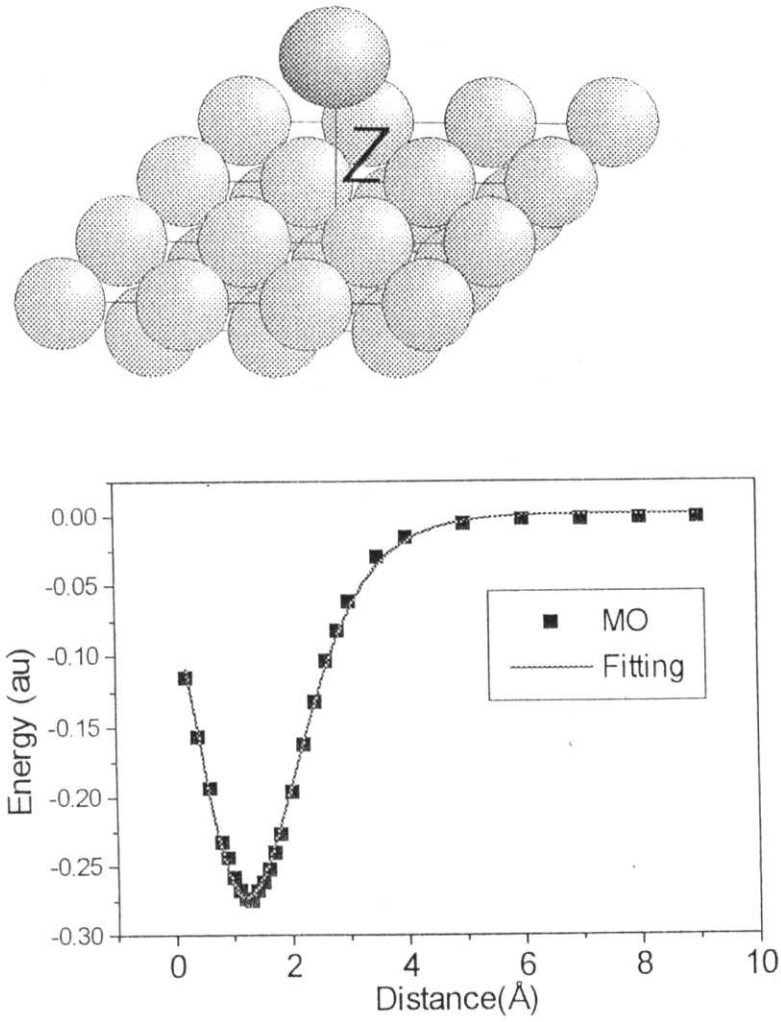

Fig. 1. The potential energy (atomic unit) curve of the SNi_{25} cluster as a function of ***Z***. ***Z*** is defined as the vertical spacing between S and the surface Ni plane. The calculated data are given as squares, while the line is the fitted result using the Morse potential (see text).

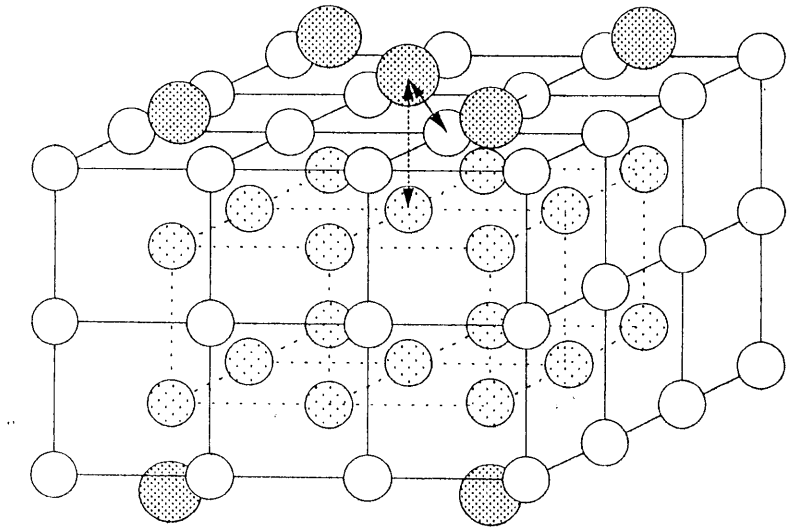

Fig. 2. A surface cluster cell used in the MD calculations. Open and lightly-hutched circles corresponds to Ni atoms, while darker clusters to S or Cl. Periodicity was taken into account for the lateral directions, and the adsorbate atoms were put in both top and bottom faces. Solid and dotted arrows imply the first- (Ni1) and second-NN (Ni2) coordinations, respectively.

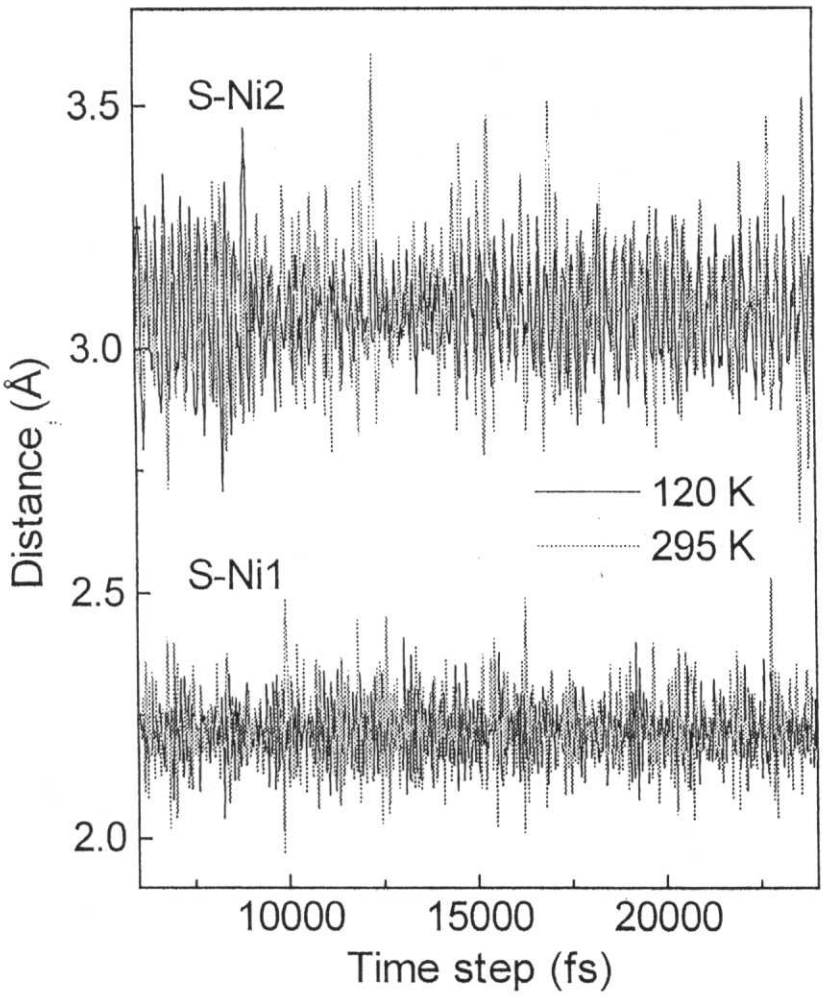

Fig. 3. Time evolutions of the interatomic distances of S-Ni1 and S-Ni2 pairs at T_1=120 K and T_2=295 K for the c(2×2)S/Ni(100) system.

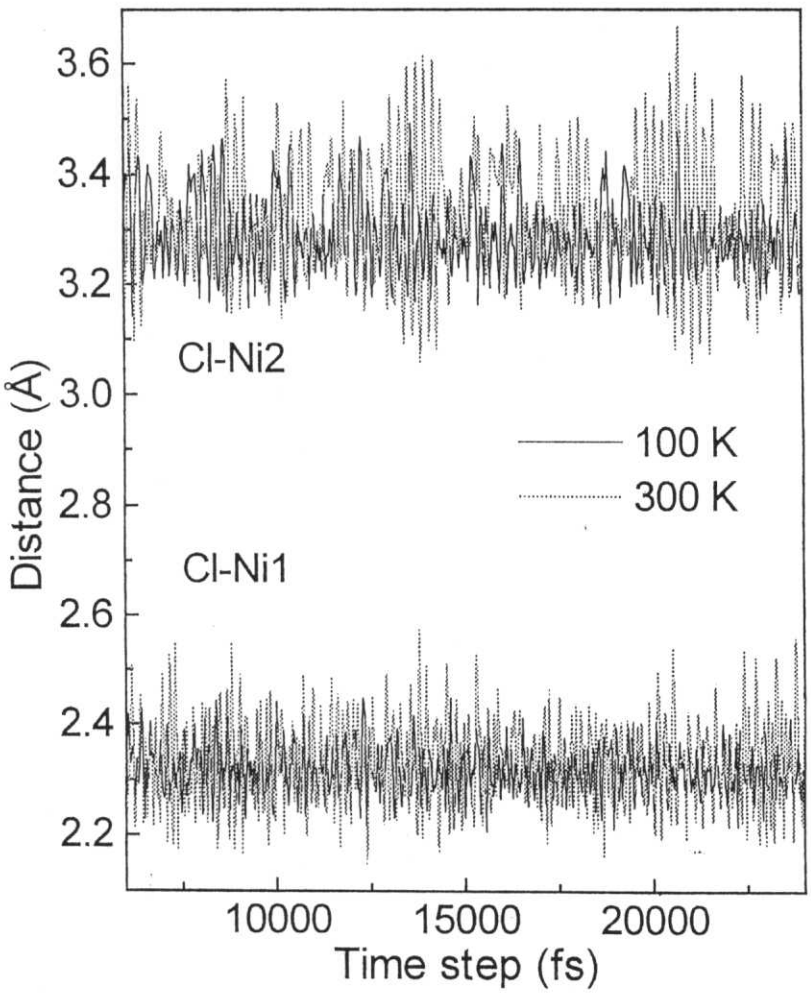

Fig. 4. Time evolutions of the interatomic distances of Cl-Ni1 and Cl-Ni2 pairs at T_1=120 K and T_2=300 K for the c(2×2)Cl/Ni(100) system.

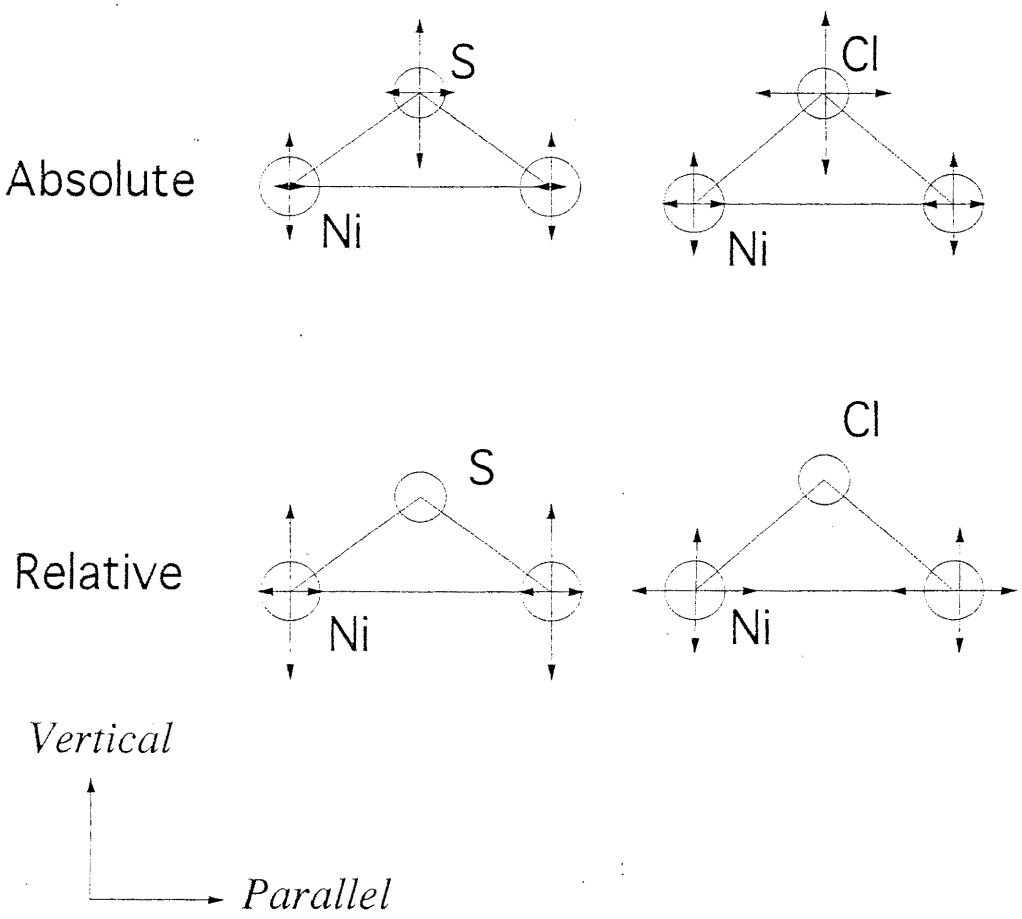

Fig. 5. Schematic views of the directional vibrational amplitudes at $T=T_2$. The components of the mean-square displacements Δu_2 (A) and Δu^2(Ni1) and of the mean-square relative displacements ΔR^2 (A-Ni1) (A=S, Cl) are depicted, which were obtained by the MD simulations. For ΔR^2, atom A is assumed to locate at the origin.

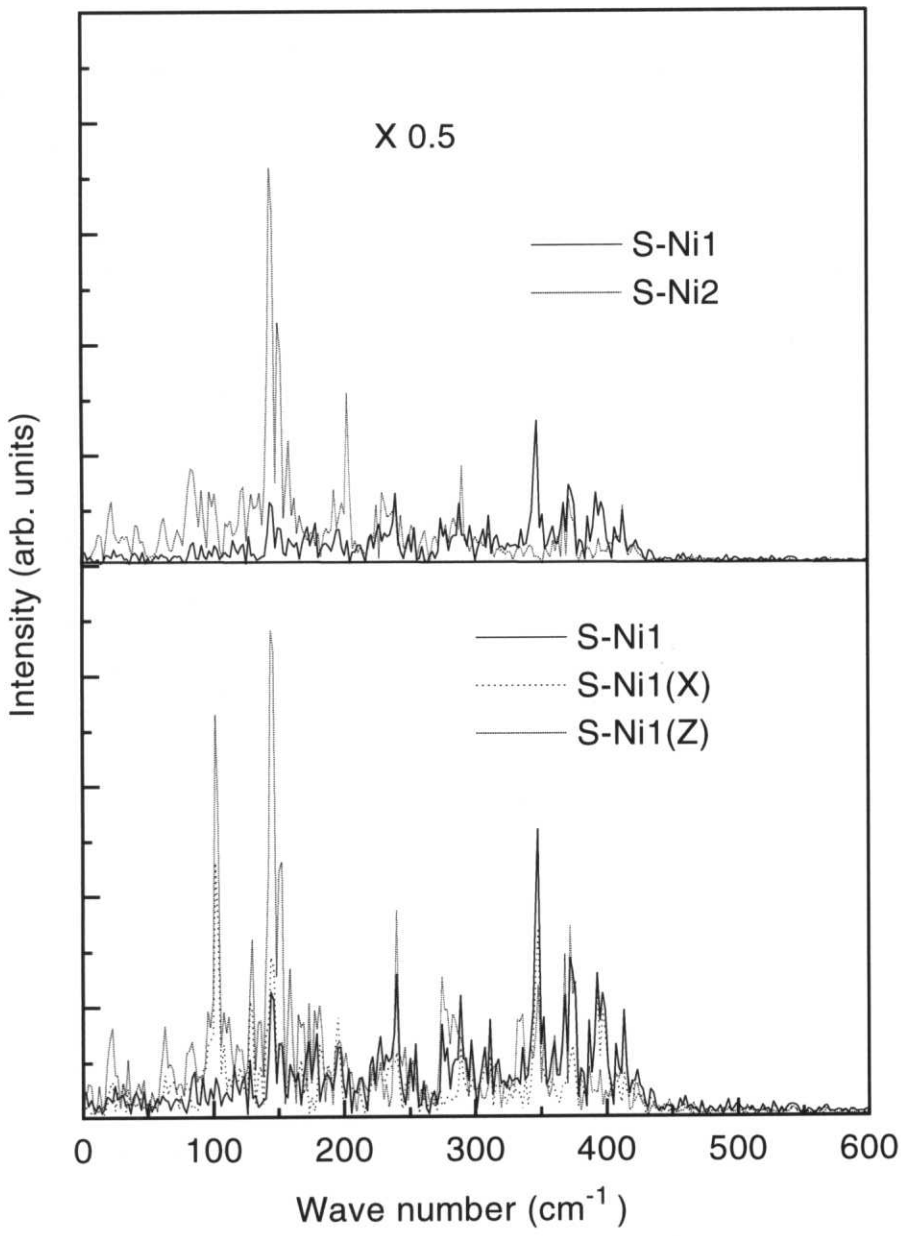

Fig. 6. Fourier transforms of the time evolutions of the S-Ni1 and S-Ni2 distances and of the lateral(X) and vertical(Z) components of the S-Ni1 bond vector at T_1=120 K.

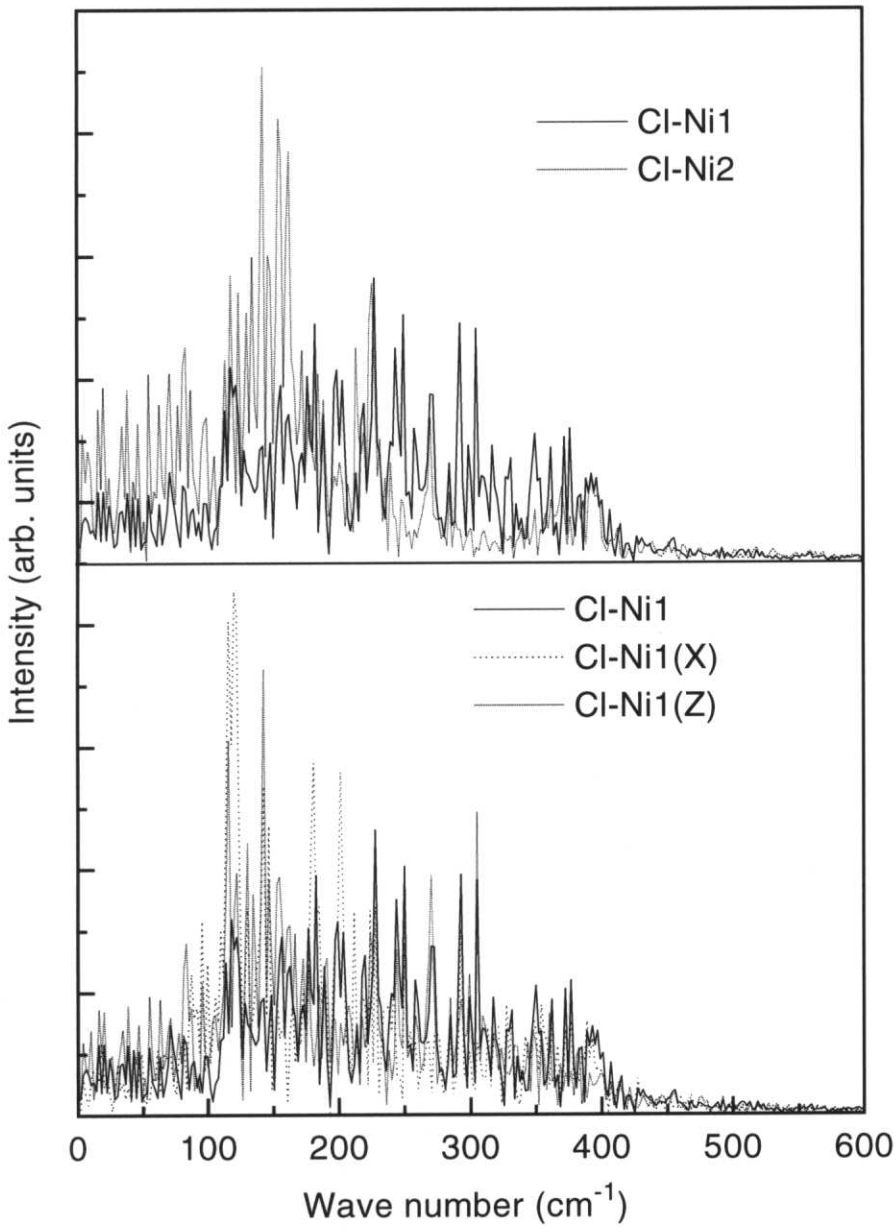

Fig. 7. Fourier transforms of the time evolutions of the Cl-Ni1 and Cl-Ni2 distances and of the lateral(X) and vertical(Z) components of the Cl-Ni1 bond vector at T_1=100 K.

7 Coverage dependence of surface structure and vibration of Cl/Cu(100) compared to Cl/Ni(100)

7. 1 Introduction

Static and dynamical properties of atoms adsorbed on single crystal surfaces often show interesting coverage dependence. Anderson, Karlsson, and Persson [1] studied the coverage dependence of O and S/Ni(100) with the high resolution electron-energy-loss spectroscopy methods. They found that in the O/Ni(100) system the O-Ni vibrational frequency is significantly reduced with increased O coverage, while in the S/Ni(100) case the S-Ni frequency shift is much smaller than the upper case. Bauschlicher and co-workers [2, 3] treated the same systems theoretically using a cluster model. They succeed in explaining vibrational softening of the O-Ni bond with the O coverage, and also found slight stiffening of the S-Ni bond with S coverage. They ascribed such a different nature between O and S to the different coverage dependence of charge transfer from Ni to adsorbate atoms. In the structural studies based on LEED (low-energy electron diffraction) and SEXAFS (surface-extended x-ray-absorption fine structure) of p(2×2) and c(2×2) states; however, neither O nor S adsorbates give any meaningful difference in the adsorbate-substrate bond distance [4-6].

Very recently, we examined the coverage dependence of the surface structures and vibrational properties of Cl/Ni(100) by means of temperature-dependent Cl *K*-edge SEXAFS, and found that the Cl-Ni vibration is softer and more anharmonic in the 0.50-ML case than in the 0.25-ML one, associated with the elongation of the Cl-Ni bond distance at higher coverage [7]. These findings were explained by the enhancement of the adsorbate-adsorbate repulsive interaction with Cl coverage, as in the case of O/Ni(100). In order to obtain deeper insight into adsorbate-metal substrate bonding, it should be of particular interest to investigate the coverage dependence of Cl/Cu(100) and to compare with the results from Cl/Ni(100), since the surface structures are quite similar to each other.

Thus, in the present study, we have measured and analyzed temperature-dependent Cl *K*-edge SEXAFS spectra of Cl/Cu(100) with 0.12- and 0.50-ML Cl coverage. The surface structure of 0.50 ML Cl/Cu(100) with a c(2×2) LEED pattern has already been investigated [8-10], while that of a lower coverage has not been reported yet. The Cl-Cu bond distance, the vibrational amplitude and anharmonicity were obtained for these two samples, and the two-body interatomic potentials were consequently estimated. The present results of Cl/Cu(100) are compared to those of Cl/Ni(100). Density-functional quantum-mechanical calculations were also carried out by employing a metal cluster with different number of adsorbate Cl. Origins of the observed coverage-dependent nature of the Cl-metal bonds in Cl/Ni(100) and Cl/Cu(100) are discussed using the calculated electronic properties.

7. 2 SEXAFS

7. 2. 1 Experiment

A mechanically and electrochemically polished Cu(100) crystal was cleaned in an UHV (ultrahigh vacuum) chamber (the base pressure was less than1×10^{-8} Pa) by repeated cycles of Ar^+ sputtering and annealing at 900 K [11, 12]. A clear (1×1) LEED pattern was observed and both S and Cl contamination were found to be less than 0.01 ML. The clean Cu(100) crystal was dosed with Cl_2 given by the electrolysis of AgCl in a manner similar to that described previously [7, 13]. Two samples were prepared by Cl dosage at room temperature, and subsequent annealing to 573 K. One correspond to a saturation coverage (0.50 ML), which gave a clear c(2×2) LEED pattern. The other gave a lower overage (0.12-ML Cl), and exhibited only rather a diffuse (1×1) pattern. Here the Cl coverage was estimated from the normalized Cl-*K* fluorescence yield (edge jump), by assuming the Cl coverage of the former sample of 0.50 ML.

Cl *K*-edge SEXAFS measurements were carried out at the soft x-ray double-crystal monochromator station BL-11B of the Photon Factory in National Laboratory for High Energy Physics [14-16]. The factor of linear polarization was estimated to be larger than 0.97 for the monochromatized photons and the energy resolution of the Ge(111)

monochromator was about 1.5 eV around the Cl *K*-edge region. The fluorescence yield detection method was employed to obtain Cl *K*-edge SEXAFS data by using an UHV-compatible gas-flow proportional counter with p10 gas (10 % CH_4 in Ar) as a detector [17]. The SEXAFS spectra of 0.12 and 0.50 ML Cl/Cu(100) were taken at normal (θ=90°) and grazing (θ=15°) x-ray incident angles. For the normalization of the fluorescence yield spectra with the intensity of the incident x-rays, we measured a drain current from a Cu mesh in the upstream of the sample crystal. The measurements were done at 100 and 300 K. For the measurement at 100 K, the sample crystal was cooled down using a liquid N_2 cryostat. The sample temperature was monitored with a chromel-alumel thermocouple, which was spot-welded on a Ta sheet attached to the sample surface. The temperature fluctuations were less than +3 K during the SEXAFS measurements.

7. 2. 2 Static surface structures

Extraction of the EXAFS function $\chi(k)$ (k is the photoelectron wave number) was carried out according to the well-established procedures: pre- and post-edge background subtractions and subsequent normalization with the atomic absorption coefficients [18, 19]. The edge energy E_0 was tentatively chosen as an inflection point of the Cl *K* edge of the 15° spectrum for each sample. Figure 1 and 2 show $k\chi(k)$ functions and corresponding Fourier transforms, respectively. The assignments of the Fourier peaks can be performed according to the literature [6-9]. The most noticeable difference between 0.12 and 0.50 ML is found at ~3.3 Å in the Fourier transforms for 90° incidence [compare Fig. 2(c) with Fig 2(d)]. This peak in Fig. 2(c) is attributed to the Cl-Cl shell. In the 0.50 ML coverage the c(2×2) overlayer is completed, this leading to an intense Cl-Cl contribution. On the other hand, in the 0.12 ML one [Fig. 2(d)] this peak is not observed, implying that no noticeable formation of the c(2×2) islands occurs. Another difference between 0.12 and 0.50 ML is observed in the first-nearest neighbor (NN) Cl-Cu shells appearing at ~2.1 Å. When we compare the low-temperature data at 15° incidence, which give the most intense first-NN contribution [see solid lines of Figs. 2(a)

and 2(b)], we find that the 0.50 ML coverage provides a little shorter Cl-Cu distance than in the 0.12 ML one, this being quantitatively clarified by the following curve-fitting analysis.

The curve fitting analysis of the first-NN Cl-Cu shells for the 100 K data in the k space was subsequently performed after the Fourier filtering and inverse Fourier transformation, using theoretical standards given by FEFF6 [20]. Fitting parameters employed were NS_0^2 (effective coordination number N^* multiplied by the intrinsic loss factor S_0^2), R (interatomic distance), ΔE_0 (edge energy shift) and C_2 (mean square relative displacement). C_2 for the 90° incidence data was consequently fixed to be the same as that for the 15° incidence one to give meaningful value of $N^*S_0^2$.

The results are summarized in Table 1, together with the fitting ranges. The first-NN Cl-Cu distance was determined to be 2.42±0.02 Å for 0.12 ML and 2.39±0.02 Å for 0.50 ML, respectively. The Cl-Cu distance of 2.39 Å in the 0.50-ML state is in good agreement with the result of 2.37±0.02 Å (at 80 K) given by the previous SEXAFS [6, 8, 9], and 2.38±0.05 Å (at 110 K) given by the photoelectron diffraction (PhD) measurements [21], but is slightly smaller than the value of 2.41±0.02 Å by LEED [22]. Although the distance difference between the 0.12- and 0.50-ML states is within the errors, a higher coverage state provides a slightly shorter bond distance, as found in the Fourier transforms in Fig. 2. For better understanding of the distance difference we show the filtered $k\chi(k)$ functions for the first-NN Cl-Cu shells at 15° x-ray incidence in Fig. 3, which includes temperature dependence discussed below. When the $k\chi(k)$ function at 100 K for the 0.50-ML coverage [the solid curve in Fig. 3(a)] is compared to that for the 0.12-ML one [the solid curve in Fig. 3(b)], the phase for the former is gradually delayed more than that for the latter, implying a shorter Cl-Cu distance in the 0.50-ML coverage.

On the other hand, from the ratios of the effective coordination numbers $N^*(90°)/N^*(15°)$ of 0.62±0.10 for 0.12 ML and 0.66±0.07 for 0.50 ML, adsorption of Cl on the fourfold hollow site can be confirmed in both the states since the expected values of $N^*(90°)/N^*(15°)$ for the hollow site are 0.66 and 0.68, respectively.

7. 2. 3. Vibrational properties of the surface Cl-Cu bonds

Temperature dependence of the EXAFS spectra for the first-NN Cl-Cu shells was subsequently analyzed. The Δk_{FT} and ΔR ranges were the same as the above structural analysis given in Table 1. Figure 3 also shows the temperature dependence of the filtered $k\chi(k)$ functions for the first-NN Cl-Cu shells. It is clearly found in both the 0.12- and 0.50-ML states that as the temperature increases the EXAFS amplitude is reduced and the phase is gradually delayed at higher k regions. The amplitude reduction at higher temperature is the consequence of increase in the mean-square relative displacement C_2 (EXAFS Debye-Waller factor). The phase delay is not caused by the shortening of the Cl-Cu distance at higher temperature but by increase in the mean-cubic relative displacement C_3 [23]. One can clearly find that the phase delay at higher k region is more enhanced in the 0.12-ML state than in 0.50-ML one, and correspondingly the amplitude reduction is found to be slightly more significant in the 0.12-ML state. This indicates that temperature differences of the cumulants ΔC_2 (T_1, T_2) and ΔC_3 (T_1, T_2) (T_1=100 K and T_2=300 K) are greater in the 0.12 ML state.

The numerical values of ΔC_2 and ΔC_3 were obtained by the amplitude ratio and phase difference methods and also the curve-fitting method [19], where Δk employed were 3.2-8.9 Å^{-1}. The results are tabulated in Table 2, together with the previous results on Cl/Ni(100) for comparison [7], which provides more quantitative and detailed information. ΔC_2 (100 K, 300 K) for the 0.50 ML state was obtained as 6.2(6)×10^{-3} Å^2, which agree with ΔC_2 (80 K, 280 K) of 5.5(5)×10^{-3} Å^2 by the previous SEXAFS experiments [6, 9] within the errors and slightly deviated from ΔC_2 (110 K, 300 K) of 4.5(4)×10^{-3} Å^2 by PhD [21].

In order to describe the interatomic potentials of the Cl-Cu atom pair, one can simply assume a third-order polynomial within the two-body Einstein approximation as

$$V(r) = \frac{1}{2}\alpha(r - r_0)^2 - \beta(r - r_0)^3$$

where α and β are the second- and third-order force constants, respectively, and r_0 the equilibrium distance (potential minimum). The relationship between the EXAFS cumulants and the force constants in the case of the two-body system have been clarified

using the first-order quantum statistical perturbation theory of thermal averages [24-27]. The evaluated results of α and β using ΔC_2 and ΔC_3 are also given in Table 2. The second-order force constant α is found to be slightly larger in the 0.50 ML state, while the third order force constant β is larger in 0.12 ML, implying stiffer vibration and smaller anharmonicity at higher Cl coverage. Although the difference is again not so significantly for each value, all the results of R, α and β consistently indicate the Cl-Cu bond strength is greater at higher Cl coverage.

Figure 4 shows ΔC_2 and ΔC_3 variations as a function of the Cl-metal (Cu and Ni) distance. It is apparently found that with an elongation of the Cl-metal distance ΔC_2 and ΔC_3 increase monotonically, this implying that the longer bond is the softer and more anharmonic. The most important finding is the difference of the coverage dependence. As noted in Section 1, in the previous Cl/Ni(100) system the Cl-Ni bond is noticeably weakened as the Cl coverage increase, while in the present Cl/Cu(100) case the Cl-Cu bond is found to be tightened with the Cl coverage. Although each difference is the bond distance, ΔC_2 and ΔC_3 is within the error bars in the case of Cl/Cu(100), all the results suggest the tightening of the Cl-Cu bond with the coverage, which sounds physically significant.

7. 3 Density functional calculation

7. 3. 1 Methods

In order to understand the different coverage dependence between the Cl/Ni(100) and Cl/Cu(100) system, we performed first-principle qunatum-mechanical calculations on the cluster models of those surfaces. The method used was an *ab initio* calculation based on the density functional theory (DFT). The calculations were done by use of the DFT quantum-mechanical code DMOL ver. 950 of Biosym/MSI, by using the double numerical basis functions with polarization function [28-30] as the atomic basis set and the local spin density functional derived by Vosko, Wilk, and Nusair [31]. All inner core levels were frozen in the present calculations.

The cluster model used for the M(100) (M=Ni, Cu) surface was composed of 25

metal atoms, among which 16 M atoms were in the top atomic layer and nine atoms were in the second layer [2, 3, 32]. The coordination of atoms and all the M-M distance were taken to be the same as in the bulk metal crystal, implying the assumption of unrelaxed and unreconstructed surfaces. In the calculations for the low coverage state (0.12 ML), one Cl atom was placed on the fourfold hollow site at the center of the top atomic layer of the above metal cluster (see Fig. 5). Hereafter we denote this model as the Cl_1M_{25} cluster. Fixing the position of the metal atoms in the Cl_1M_{25} cluster, we calculated the total bonding energy as a function of the height of the Cl atom, Z, measured from the top metal atom plane.

For the higher coverage c(2×2) state, five Cl atoms were put on the five fourfold hollow sites of the top metal atom plane as shown in Fig. 5. This cluster model is denoted as the Cl_5M_{25} cluster. In this case, the height of the Cl atoms except that of the one at the center were taken at first taken to be equal to the value found for the most stable state from the calculations on the Cl_1M_{25} cluster. Fixing the positions of metal atoms and four Cl atoms at the surrounding sites, we calculated the total binding energy of the cluster as a function of the height of the central Cl atom. After obtaining the equilibrium distance the surrounding four Cl atoms were replaced at the optimized positions and the total energy calculations were performed once again to verify the equilibrium distance. The distance was found to be completely identical and one does not have to care the slight change of the heights of the surrounding Cl atoms.

7. 3. 2 Results

Let us first discuss the theoretical equilibrium Cl-atom distance. To determine the Cl-metal distances, the total energy curve was calculated as a function of the Cl height Z in the vicinity of the potential minimum, the results being plotted in Fig. 6. Using parabolic fits the equilibrium distances were finally obtained, and the results are summarized in Table 3. The interatomic distance between the central Cl and the first-NN Ni was found to be 2.288 Å for Cl_1Ni_{25} and 2.301 Å for Cl_5Ni_{25}, respectively, while that was 2.371 Å for Cl_1Cu_{25} and 2.358 Å for Cl_5Cu_{25}. These values are close to the experimentally

obtained distance of 2.31-2.41 Å, this implying a high reliability of the present density-functional calculations. The sequence of the Cl-metal bond length was well reproduced. The Cl-Ni distance is noticeably shorter (by ~0.07 Å) than the Cl-Cu one, this being consistent with the experimental tendency (~0.07 Å). For the coverage dependence as well, the calculated results indicate that in the case of Cu the Cl-Cu distance is getting shorter with the Cl coverage, while on Ni the Cl-Ni distance is the longer. This consequence is fully consistent with the experimental findings.

Figure 7 shows that the calculated density of states (DOS) of these clusters, where each discrete level has been artificially broadened with the width of 0.2 eV. The energy is the one measured from the vacuum level. In the total DOS, chlorine-derived peaks appear around ~9.7 eV for Cl_5Ni_{25} and ~10.7 eV for Cl_5Cu_{25}, which can be ascribed to the Cl 3p components interacting with metal 3d bands. Although ultraviolet photoemission spectra (UPS) of Cl/Ni(100) has not been reported to our knowledge, the UPS of Cl/Cu(100) has been studied in detail [33-36], and shows a Cl 3p peak at ~5 eV below the Fermi level E_f. Since the present calculations gave a work function of 5.2 eV for Cl_5Cu_{25}, the theoretical energy level of Cl 3p (5.5 eV in regard to E_f) is found to provide good agreement with the experiment. The overall features of the calculated spectrum of Cl_5Cu_{25} are also consistent with the experiment, this indicating that our cluster model has picked up the surface state properly.

Figure 7 also shows the partial DOS of Cl 3p (only for central Cl) and metal 3d bands. A clear difference in the coverage dependence between Cl_xNi_{25} and Cl_xCu_{25} can be detected. On the Cu substrate, the components of both Cl 3p and Cu 3d as well as the total DOS are found to shift to a higher-binding-energy side as the Cl coverage increases. On the other hand, on the Ni substrate, no significant coverage dependence can be found in the partial DOS of Ni 3d or the total DOS. In the Cl 3p levels, a single dominant contribution is seen at ~10 eV for Cl_1Ni_{25}, while for Cl_5Ni_{25} this contribution is spread into several peaks. It should be noted that one of the Cl 3p levels for Cl_5Ni_{25} is located at a low-binding-energy side of ~9.1 eV, yielding the lower-energy shift of the whole Cl 3p levels. This indicates that the increase in the Cl coverage induces the weakening of the

Cl-Ni bonds.

Table 3 gives the Mulliken charges of the central Cl atom. One can find that by comparing the results of Cl_1Ni_{25} and Cl_1Cu_{25}, the ionicity of Cl does not change at a low Cl coverage between Ni and Cu. This is reasonable, since the electronegativities of Ni and Cu are almost equal to each other. The coverage dependence is, however, significantly different. The Cl ionicity is enhanced on Ni with the coverage, while on Cu the ionicity is reduced. As mentioned in Section 1, similar findings have been reported by Bauschlicher and co-workers [2, 3] on the O/Ni and S/Ni systems. According to their molecular-orbital calculations of model clusters, charges on O and S on Ni(100) are almost the same at low coverage. On increasing the coverage, however, O becomes more negatively charged, while S becomes less ionic though the effect on S is small. The trend resembles the present findings.

7. 4 Discussion

As a consequence of the previous experimental and theoretical sections, the observed coverage dependence of the interatomic distance $R_{Cl\text{-}M}$, the second order force constant α, and the third-order constant (anharmonicity) β in the Cl/Ni(100) and Cl/Cu(100) systems could be ascribed to the variation of the Cl charge q_{Cl} obtained theoretically. Let us consider two different chemical interactions of ionic and covalent bonds. The decrease in ionicity implies the enhancement of the covalent nature, as long as the chemical bond is preserved. In general, since the ionic and covalent attractive interactions are long- and short-range forces, respectively, the curvature of the ionic potential should be looser than that of the covalent one. This leads to smaller α and β in more ionic interaction, being consistent with the present experimental findings. For the Cl-metal distance as well, it can be remarked that the more covalent the interaction, the shorter the bond length, because the covalent interaction requires more significant overlap between the atomic orbitals than the ionic one (in other word, covalent radii are smaller than ionic radii). This is also consistent with the experimental and theoretical results.

A remaining question might be why the Cl charge exhibits such a drastic difference in

the coverage dependence between Ni and Cu. This should originate form the different chemical interactions between Cl-Ni and Cl-Cu bonds. Since Ni is a transition-metal element, Ni 3d orbitals dominantly participate in the Cl-Ni bond formation. On the other hand, Cu 3d orbitals located at higher bonding energies are fully occupied and are less important for the Cl-Cu bond. Instead the Cu 4s level interacts with Cl 3p. Since the 3d orbital is much more localized than the 4s orbital, the chemical bond for the Cl-Ni pair is stronger than that for the Cl-Cu pair. This was clearly demonstrated by the present SEXAFS results (see Table 2).

For discussion the coverage dependence, it might be complicated to consider the interaction between the neutral Cl and the metal surface, since Cl plays significant roles of both electron donor and acceptor. Thus let us here consider the interaction between Cl^- anion and the cationic metal surface. As the Cl coverage increase, the electron of Cl^- is donated to the Cu 4s band in the Cl/Cu system, while that is donated mainly to the Ni 3d band in Cl/Ni. Since the Cu 4s band is broadened and is of less density in the vicinity of the Fermi level, the increase in electrons should shift the Fermi level (work function) of the Cu metal significantly. On the other hand, because of a higher density of the Ni 3d band, the Fermi level does not change so much for the Ni metal. These remarks are actually found in Fig. 7.

These should be two competing repulsive forces in the case of higher-coverage Cl adsorption. One is the Cl-Cl repulsive Coulomb force, and the other is the electron-electron repulsion in the metal band. In the case of Cu, the electrons of Cl^- are transferred into the Cu 4s band and the electron-electron repulsion is less important because of the free electron-like nature of the 4s band, implying that the Cl-Cl Coulomb interaction should be a dominant repulsive force. Consequently, so as to reduce the Cl-Cl repulsion, the charge transfer from Cl^- to the Cu 4s band is more enhanced with increase in the Cl coverage. On the other hand, in the case of Ni, the electrons from Cl^- should be localized in the Ni 3d band, and the electron-electron repulsion might play a more significant role upon the charge transfer from Cl^- to Ni metal. Accordingly, inspire of the increase in the Cl^- coverage, the Ni 3d band could not accept the electrons from

Cl^- to any great degree. The charge of the Cl anions resultantly remained more with the coverage increase, as given in Table 3. The difference of the coverage dependence of Cl between Ni and Cu metal surfaces has thus been recognized.

7. 5 Conclusion

We have measured and analyzed temperature dependence of Cl *K*-edge SEXAFS spectra of the 0.12- and 0.50- ML Cl/Cu(100) states. Local surface structures have been found to be almost identical with each other, except for the presence of the Cl-Cl coordination in the 0.50 ML c(2×2) state. The first-NN Cl-Cu bond distance is, however, slightly different 2.42±0.02 Å for 0.12 ML and 2.39±0.02 Å for 0.50 ML. The harmonic force constant is smaller and the anharmonicity is greater in the 0.12-ML state than in the 0.50-ML state. These experimental results clearly demonstrate that the Cl-Cu bond is tightened with the Cl coverage, such a coverage dependence being opposite to that in the Cl/Ni(100) system. Density-functional calculations have been carried out using finite cluster models of Cl_xNi_{25} and Cl_xCu_{25} (x=1 and 5). The tendency of the coverage dependence was reproduced well from the viewpoint of the Cl-metal equilibrium distance. Different coverage dependence was also clearly found in the DOS.

The observed coverage dependence of the distance, vibrational amplitude, and anharmonicity for the Cl-metal bonds ion Cl/Ni(100) and Cl/Cu(100) was consequently ascribed to the variation of the Cl atom. As the Cl coverage increase, the Cl ionicity is enhanced in the case of Ni, while it is reduced in the Cu case. The latter implies anenhancement of the covalency for the Cl-Cu bond, leading to a shorter bond distance and a larger force constant with the Cl coverage. The drastic difference between Ni and Cu was also explained by the different nature of the chemical interactions between Cl-Ni and Cl-Cu pairs; upon the formation of the Cl-meal bonds, the Cl 3p-Ni 3d interaction plays a dominant role for the Cl-Ni bond, while for the Cl-Cu one the Cl 3p-Cu 4s is important. This yields a different ionicity of Cl between Ni and Cu at saturation coverage. The present Cl/Ni and Cl/Cu systems have provided excellent examples for the coverage dependence of the adsorbate-substrate bond.

References

[1] S. Andersson, P. A. Karlsson, and M. Persson, Phys. Rev. Lett. **51**, 2378 (1983).

[2] P. A. Bagus, H. F. Schaefer, and C. W. Bauschlicher, Jr., J. Chem. Phys. **78**, 1390 (1983).

[3] C. W. Bauschlicher and P. S Bagus, Phys. Rev. Lett. **54**, 349 (1985).

[4] J. Stöhr, R. Jaeger, and T. K. Kendelewicz, Phys. Rev. Lett. **49**, 142 (1982).

[5] M. Van Hove and S. Y. Tong, J. Vac. Sci. Technol. **12**. 230 (1975).

[6] F. Sette, T. Hashizume, F. Comin, A. A. MacDowell, and P. H. Citrin, Phys. Rev. Lett. **61**, 1384 (1988).

[7] T. Yokoyama, S. Terada, Y. Okamoto, M. Sakano, T. Ohta, Y. Kitajima, M. Tischer and K. Baberschke. Surf. Sci. **374**, 243 (1997).

[8] P. H. Citrin, D. R. Hamann, L. H. Mattheis, and J. E. Rowe, Phys. Rev. Lett. **49**, 1712 (1982).

[9] F. Sette, C. T. Chen, J. E. Rowe, and P. H. Citrin, Phys. Rev. Lett. **20**, 311 (1987).

[10] J. R. Patel, D. W. Berreman, F. Sette, P. H. Citrin, J. E. Rowe, P. L. Cowan, T. Jach and B. Karlin, Phys. Rev. B. **40**, 1330 (1989).

[11] J. R. Patel, D. W. Berreman, F. Sette, P. H. Citrin, J. E. Rowe, P. L. Cowan, T. Jach and B. Karlin, Phys. Rev. B. **40**, 1330 (1989).

[12] S. Yagi. T. Yokoyama, Y. Kitajima, T. Takata, T. Kanazawa, A. Imanishi, and T. Ohta, Surf. Sci. **311**, 72 (1994).

[13] S. Yagi, S. Takenaka, T. Yokoyama, Y. Kitajima, A. Imanishi, and T. Ohta, Surf. Sci. **325**, 68 (1995).

[14] N. D. Spencer, P. J. Goddard, P. W. Davies. M. Kiston, and R. M. Lambert, J. Vac. Sci. Technol. A **1**, 1554 (1983).

[15] T. Ohta, P. M. Stefan, M. Nomura and H, Sekiyama, Nucl. Instrum. Methods Phys. Res. A **246**, 373 (1986).

[16] M. Funabashi, M. Nomura, Y. Kitajima, T. Yokoyama, T. Ohta and H. Kuroda, Rev. Sci. Instrum. **60**, 1983 (1989).

[17] Y. Kitajima, J. Electron Spectrosc. Relat. Phenom. **80**, 405 (1996).

[18] M. Funabashi, T. Ohta, T. Yokoyama, Y, Kitajima, and H. Kuroda, Rev. Sci. Instrum, **60**, 2505 (1989).

[19] See, for instance, X-ray Absorption: Principles, Applications, Techniques of EXAFS, SEXAFS and XANES, edited by D. C. Koningsberger and R. Prins (Wiley, New York, 1988).

[20] T. Yokoyama, H. Hamamatsu, and T. Ohta, EXAFSH version 2.1, The University of Tokyo, 1993.

[21] S. I. Zabinsky, J. J. Rehr, A. Ankdinov, R. C. Albers, and M. J. Eller, Phys. Rev. B **52**, 2995 (1995).

[22] D. Arvanitis and K. Baberschke, J. Electron Spectrosc. Relat. Phenom. **75**, 149 (1995).

[23] F. Jona, D. Westphal. A. Goldmann, and P. M. Marcus, J. Phys. C **16**, 3001 (1983).

[24] G. Bunker, Nucl. Instrum. Methods Phys. Res. **207**, 437 (1983).

[25] H. Rabus, Ph. D. thesis, Department of Physics, Freie Universität Berlin, 1991 (unpublished).

[26] A. I. Frenkel and J. J. Rehr, Phys. Rev. B **48**, 585 (1993).

[27] T. Yokoyama, K. Kobayashi, T. Ohta and A. Ugawa, Phys. Rev. B **53**, 6111 (1996).

[28] T. Yokoyama, H. Hamamatsu, Y. Kitajima, T. Tanaka, S. Yagi, and T. Ohta, Surf. Sci. **313**, 197 (1994).

[29] B. Delley. J. Chem. Phys. **92**, 508 (1990).

[30] B. Delley, J. Chem. Phys. **94**, 7245 (1991).

[31] B. Delley, D. E. Ellis, A. J. Freeman, E. J. Baerends, and D. Post, Phys. Rev. B **27**, 2132 (1983).

[32] S. J. Vosko, L. Wilk, and M. Nausair, Can. J. Phys. **58**, 1200 (1980).

[33] B. C. Laskowski and P. S. Bagus, Surf. Sci. **138**, L142 (1984).

[34] D. Westphal and A. Goldmann, Surf. Sci. **131**, 91 (1983).

[35] D. Westphal and A. Goldmann, Surf. Sci. **131**, 113 (1983).

[36] D. Westphal and A. Goldmann, Surf. Sci. **133**, 38 (1983).

[37] D. Westphal and A. Goldmann, Solid State Commun. **35**, 437 (1981).

Table 1. The results of the SEXAFS analysis for the first-NN Cl-Cu shells in the 0.12- and 0.50-ML Cl/Cu(100) states at 100 K. All the fitting k ranges Δk_{fit} are 3.2-8.9 Å^{-1}, $N^*S_o^2$, R, ΔE_0, and C_2 are the parameters given by the EXAFS experiments and the FEFF6 standards, while N^* was evaluated from the consequently determined structures.

Coverage (ML)	ϑ (°)	Δk_{FT} (Å^{-1})	ΔR (Å)	$N^*S_o^2$	R (Å)	ΔE_0 (eV)	C_2 (10^{-2} Å^2)	N^*
0.12	15	2.85-9.20	1.50-2.80	3.8(5)	2.413(20)	4.3	0.86(9)	5.10
	90	2.85-9.20	1.70-2.80	2.3(4)	2.429(20)	4.3	0.86(9)	2.71
0.50	15	2.80-9.20	1.55-2.70	3.7(5)	2.392(20)	4.3	0.76(8)	5.00
	90	2.80-9.20	1.40-2.70	2.4(4)	2.395(20)	4.3	0.76(8)	3.31

Table 2. Results of $\Delta C_2(T_1, T_2)$ and $\Delta C_3(T_1, T_2)$ (T_1=100 K, T_2=300 K) for the first-NN Cl-Cu shells in 0.12- and 0.50-ML Cl/Cu(100), together with the previous results for the first-NN Cl-Ni bond in Cl/Ni(100) (Ref. 7). The two-body effective potential parameters α, β, and r_0 are also given.

System	Coverage (ML)	ΔC_2 (10^{-3} Å^2)	ΔC_3 (10^{-4} Å^3)	α (mdyn/Å)	β (mdyn/Å^2)	r_0 (Å)
Cl/Cu(100)	0.12	6.8(6)	13.6(27)	0.35(4)	0.65(13)	2.41(2)
	0.50	6.2(6)	7.4(15)	0.38(4)	0.46(10)	2.39(2)
Cl/Ni(100)	0.25	3.7(3)	1.0(2)	0.58(4)	0.21(5)	2.31(2)
	0.50	4.4(3)	2.6(3)	0.51(3)	0.38(6)	2.34(2)

Table 3. The equilibrium Cl-M (M=Ni, Cu) distance $R_{Cl\text{-}M}$ and the Mulliken charge q_{Cl} of Cl, obtained by the density-functional calculations of the Cl_1M_{25} and Cl_5M_{25} clusters.

System	$R_{Cl\text{-}M}$ (Å)	q_{cl}
Cl_1Ni_{25}	2.371	-0.25
Cl_5Ni_{25}	2.358	-0.13
Cl_1Cu_{25}	2.288	-0.23
Cl_5Cu_{25}	2.301	-0.33

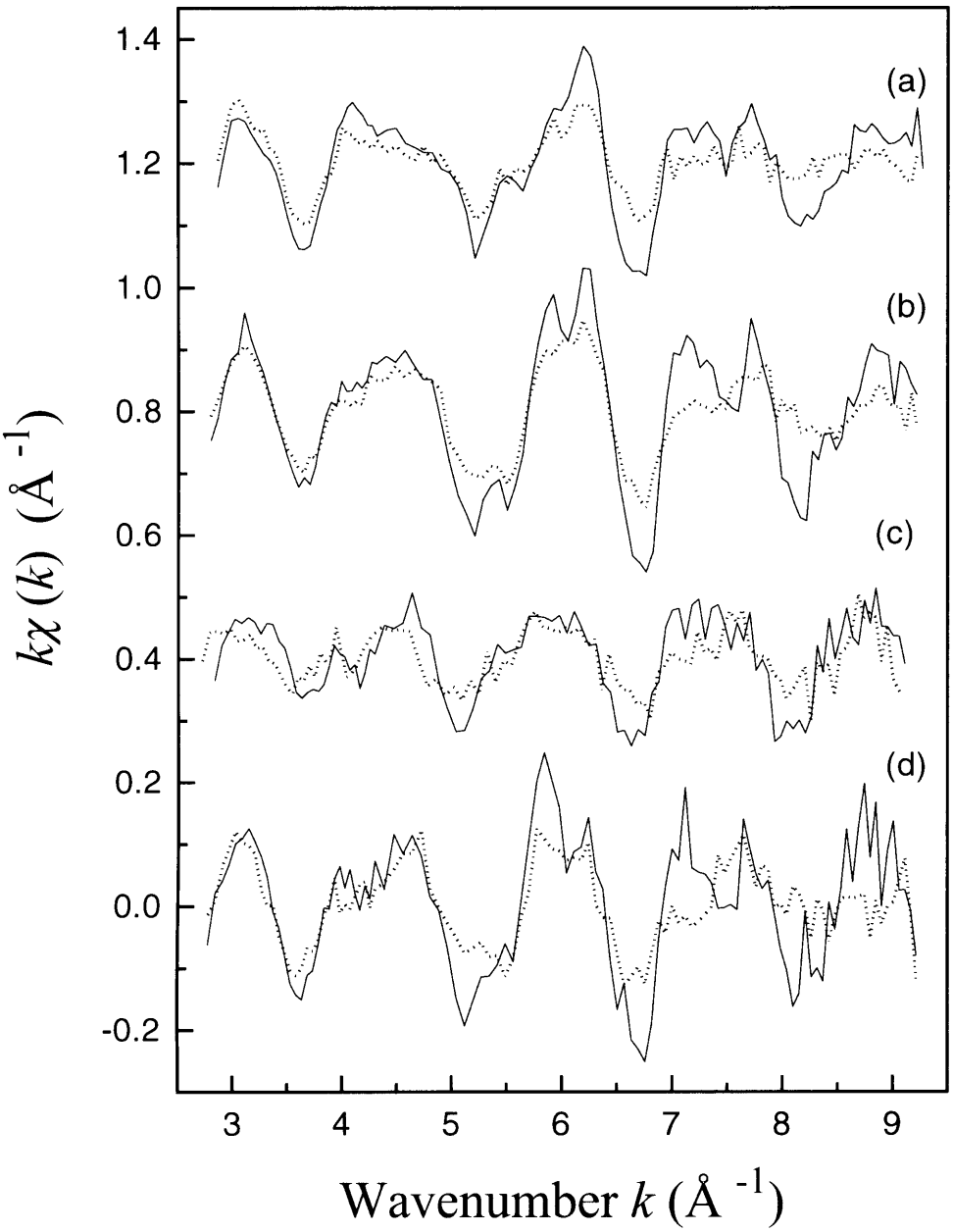

Fig. 1. Cl *K*-edge EXAFS oscillation functions $k\chi(k)$: (a) 0.50 ML, 15°; (b) 0.12 ML, 15°; (c) 0.50 ML, 90°; (d) 0.12 ML, 90°. The measurement temperatures are 100 K(solid line) and 300 K (dotted line).

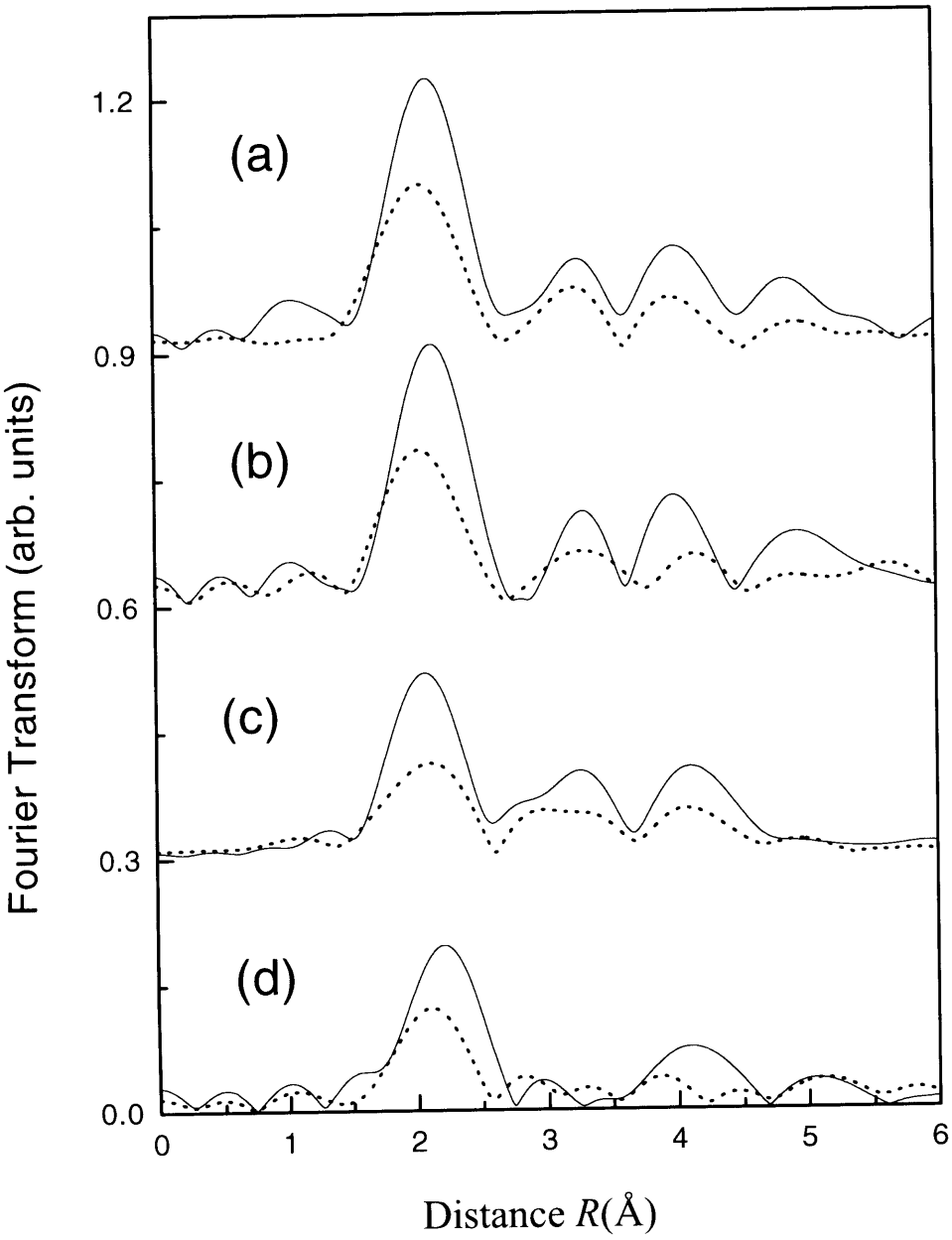

Fig. 2. Fourier transforms of $k\chi(k)$ of Cl/Cu(100): (a) 0.50 ML, 15°; (b) 0.12 ML, 15°;(c) 0.50 ML, 90°; (d) 0.12 ML, 90°. The measurement temperatures are 100 K (solid line) and 300 K (dotted line).

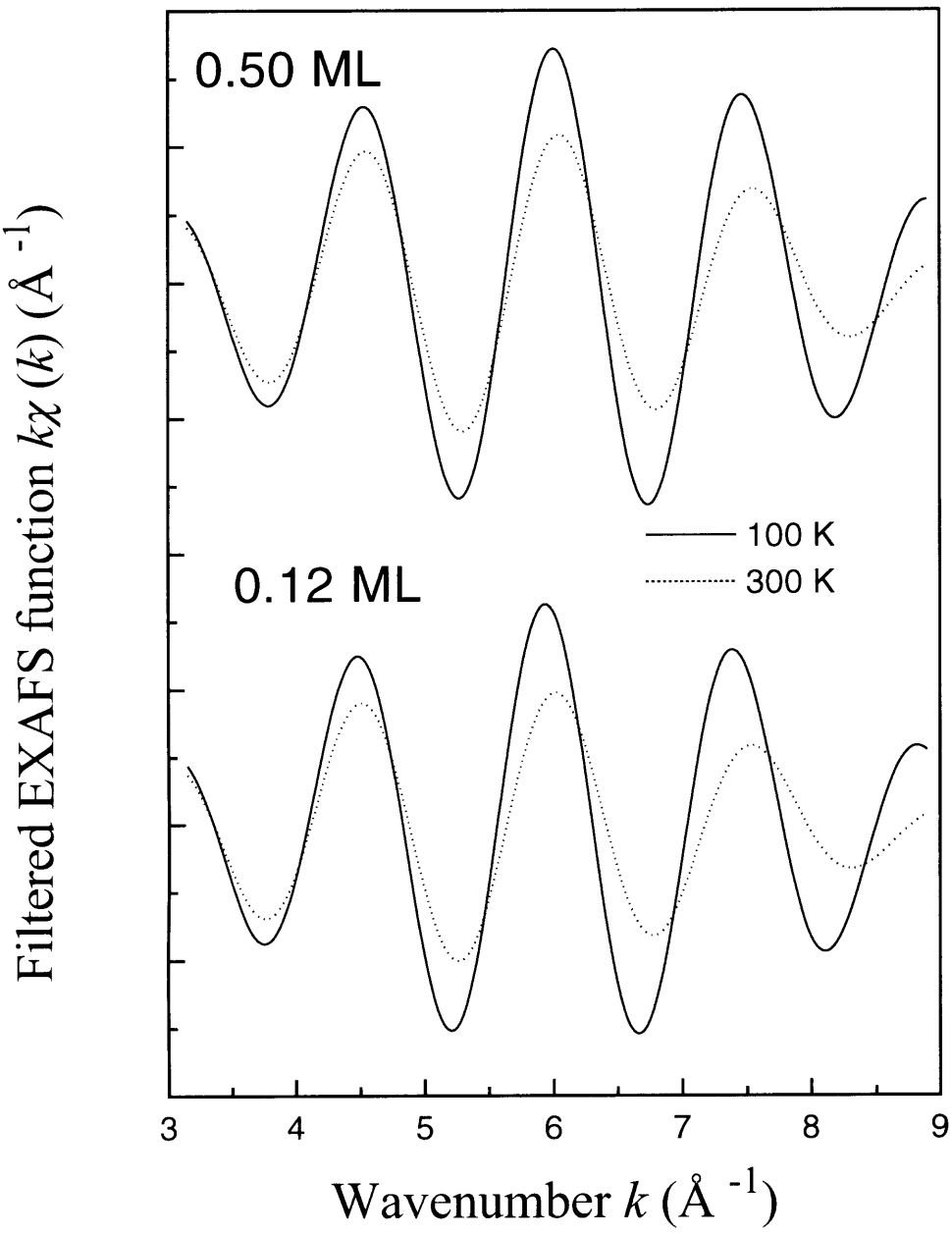

Fig. 3 Filtered $k\chi(k)$ of the first-NN Cl-Cu shells in the 15° incidence data of 0.50 ML and 0.12 ML Cl/Cu(100) taken at the temperatures of 100 K (solid line) and 300 K (dotted line).

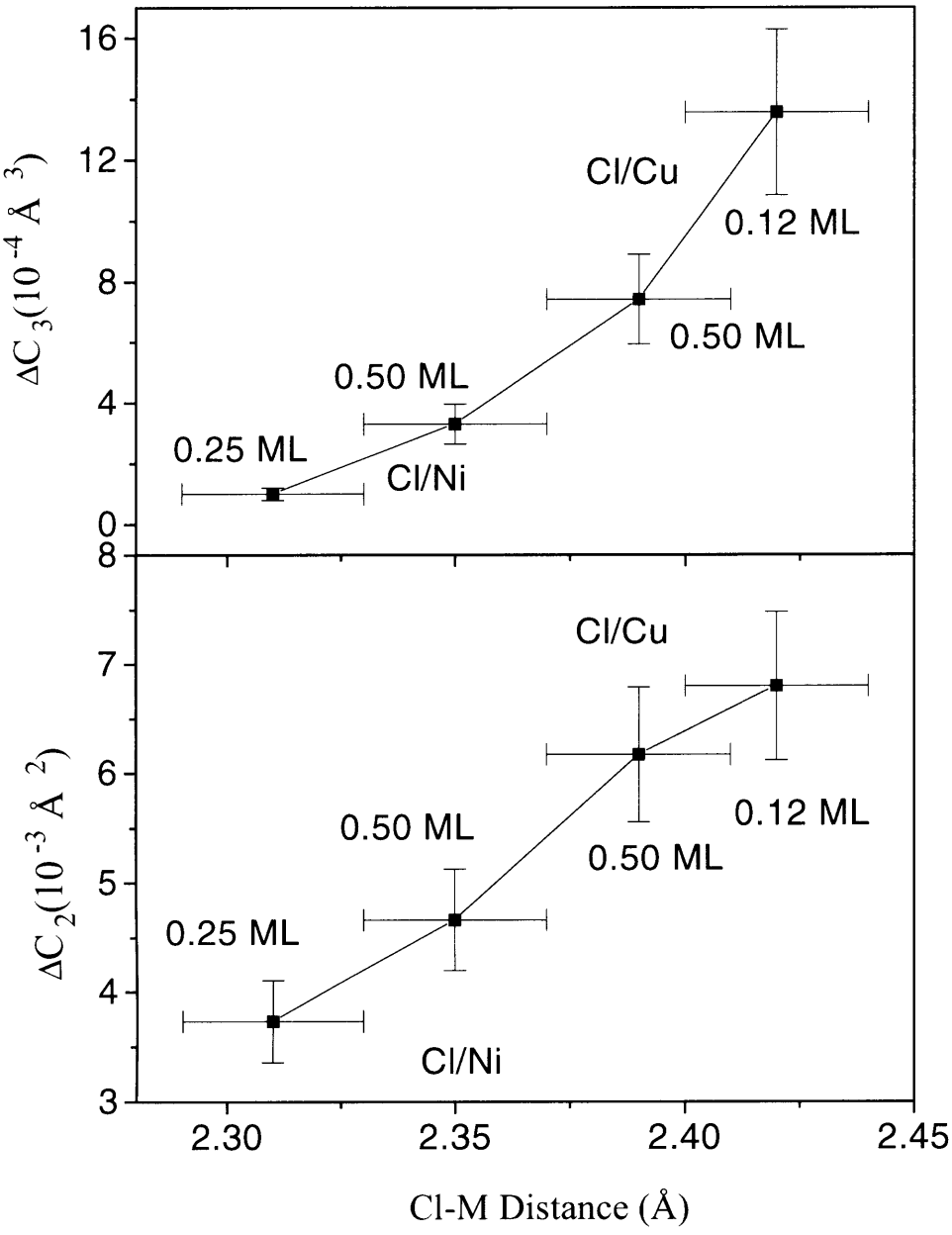

Fig. 4. $\Delta C_2(T_1, T_2)$ and $\Delta C_3(T_1, T_2)$ (T_1=100 K and T_2=300 K) of Cl/M(100) (M=Ni, Cu) as a function of Cl-M distance.

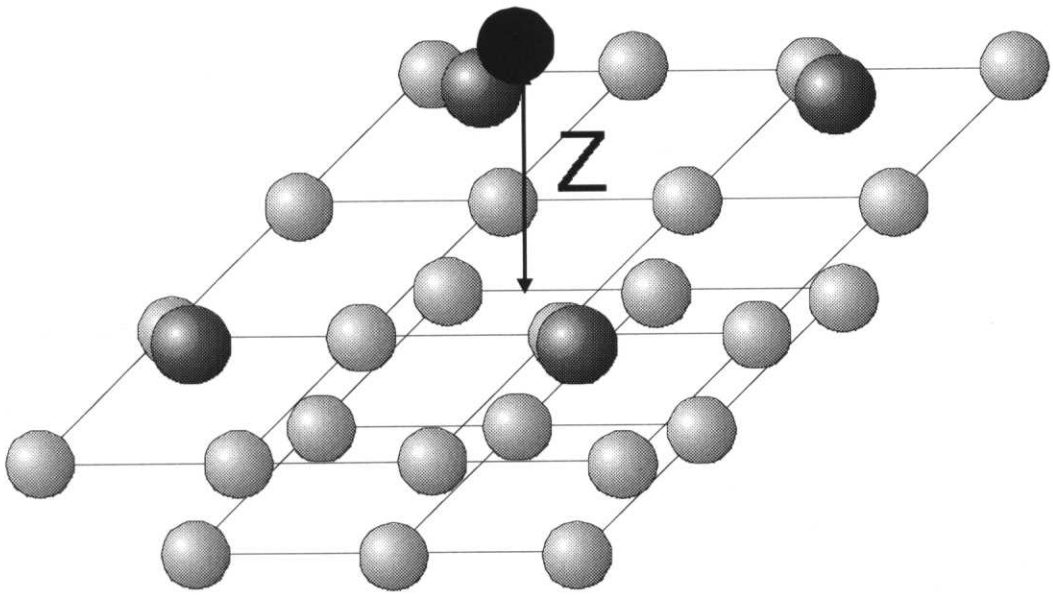

Fig. 5. Schematic view of the Cl_5M_{25} (M=Ni, Cu) cluster. Only the central Cl atom was used for the description of lower coverage, while all the five Cl atoms were included to model the c(2×2) coverage.

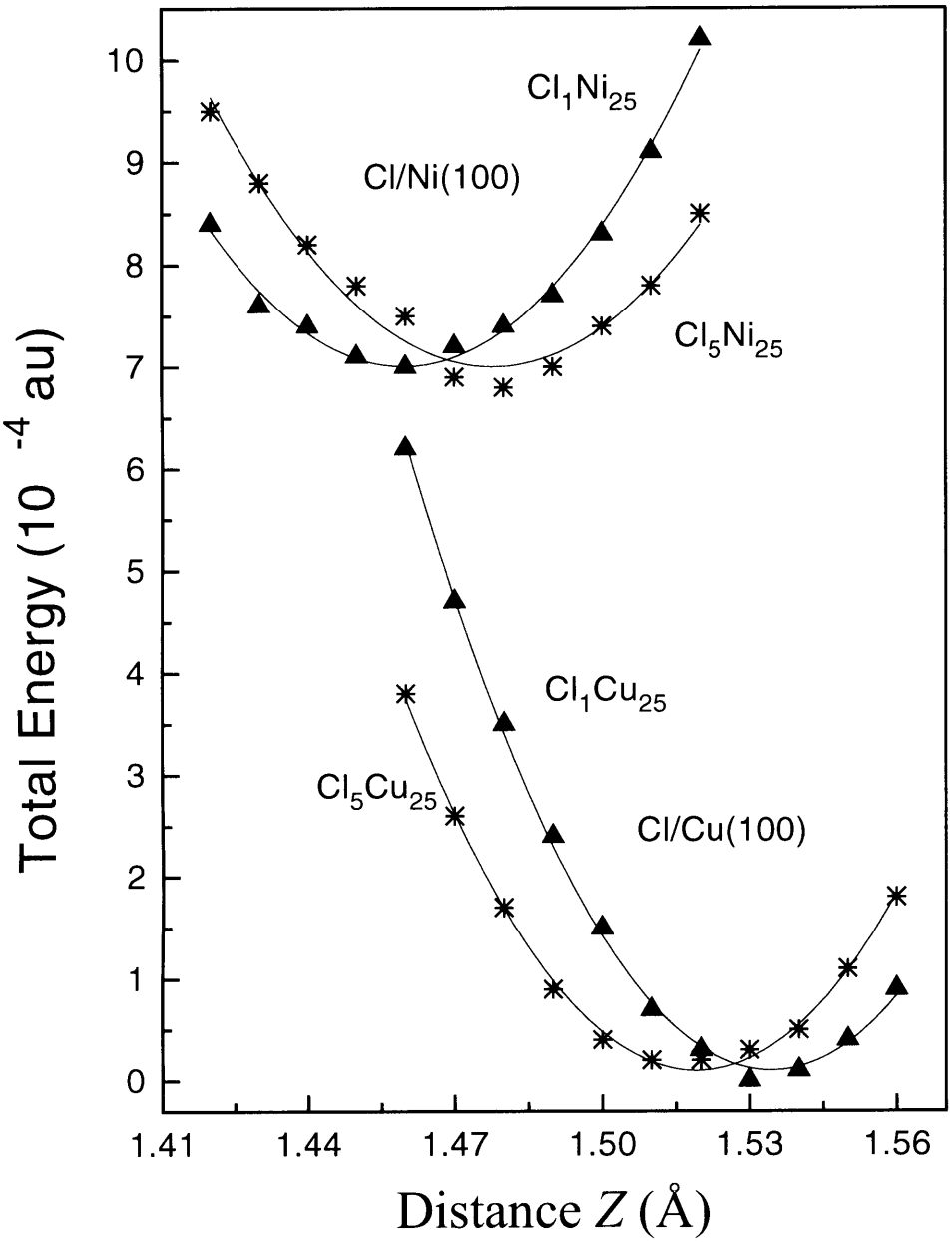

Fig. 6. Potential-energy curves of the Cl_xM_{25} clusters (x=1, 5; M=Ni, Cu) in the vicinity of the equilibrium distance. The minimum of each potential curve was assumed to be the origin of the energy.

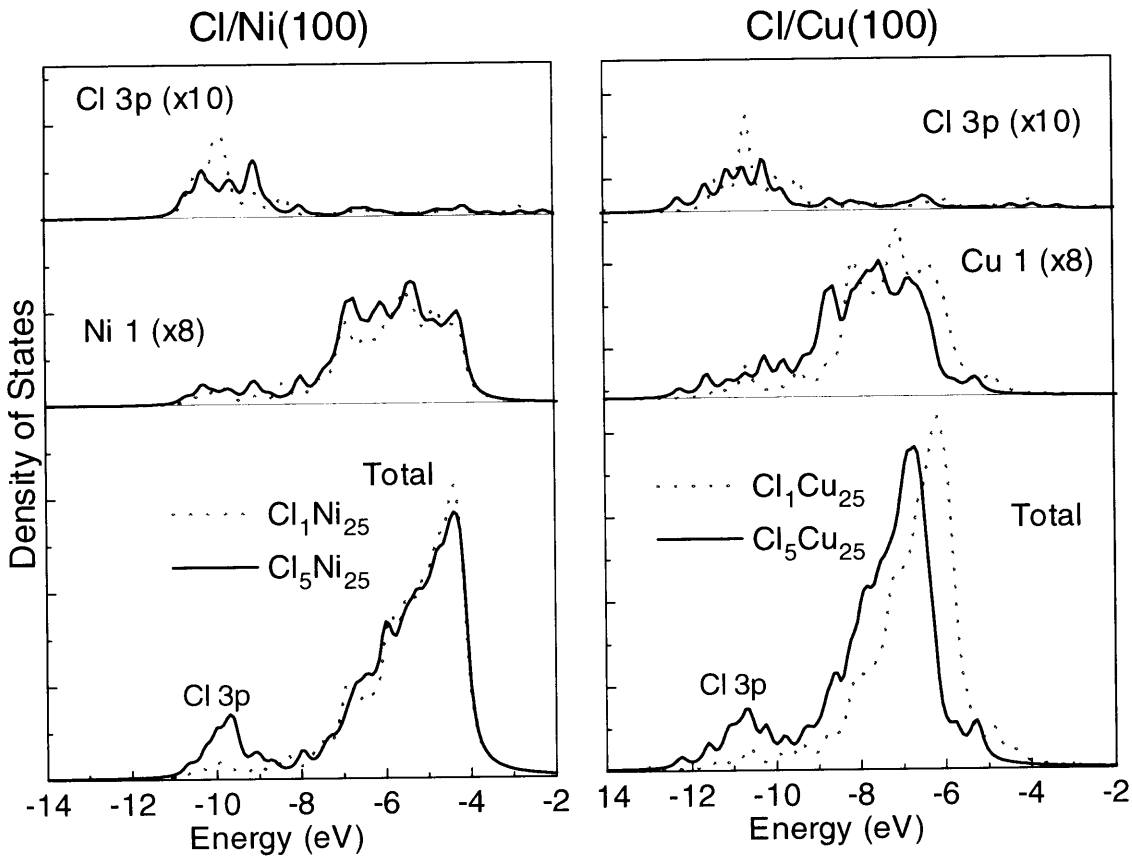

Fig. 7. The total DOS and the partial DOS of metal 3d and Cl 3p for the Cl_xM_{25} clusters (x=1, 5; M=Ni, Cu). The partial DOS of Cl 3p includes only the one for the central Cl atom, and those of metal 3d are derived only from the four first-NN metal atoms which directly interact with the central Cl. The energy is referred to the vacuum level.

8 Concluding remarks

In this thesis, chemical bond at surface and interface were studied by EXAFS for thin films.

To study the chemical bond at the interface, I have studied alkali halide hetero epitaxial thin films. Therefore, we have measured and analyzed Cl *K*-edge EXAFS spectra of epitaxially grown KCl films on KBr(001). In the initial stage of crystal growth, the in-plane K-Cl bond distance is elongated due to the substrate effect. The K-Cl bond distance is, however, rather close to the bulk KCl distance (not to the KBr distance), this contradicting with the previous idea of coherent bonding at the interface. As film thickness increases the K-Cl bond distance is shortened and the 7 ML film shows the K-Cl natural distance for bulk KCl. Because there is no distortion in the normal direction, the out-of-plane K-Cl bond distance is equal to the natural distance from the beginning of the epitaxial growth.

We have also measured Cl *K*-edge XAFS spectra to study thickness dependence of local structures of KCl and NaCl thin films grown on NaBr(100). It was suggested from XANES of the KCl/NaBr system that mixed crystal were not formed and but a KCl like film was formed at the interface. Thickness dependence of the bond distance was characterized by EXAFS. The thick KCl and NaCl films show the bulk distance, while in case of thin films the bond distance was slightly shortened for KCl and elongated for NaCl due to some influence of the substrate. As is the case of KCl/KBr system, however, these films did not grow coherently to the substrate. To analyze the structure of the top layer of the substrate, we have also carried out the MC calculation. The experimental results were reproduced within the simple pair-potential approximation and it was elucidated that the bond length of the substrate surface does not change. The local structure does not always correspond to long-range order. It is exemplified that the XAFS technique is useful for studying structures of thin films and interfaces formed of different chemical species.

For analyzing the surface bond, we have studied the metal thin films grown HOPG. Angular- and temperature-dependent Cu and Ni *K*-edge EXAFS spectra of 4 and 8 ML Cu and 4 ML Ni grown epitaxially on HOPG have been measured and analyzed in order to investigate the dynamical properties of the surface metal-metal bonds. It was revealed that thermal vibration and local thermal expansion of metal-metal bond are larger for the films than for their corresponding bulk metals and the relative motions focused on the surface local bonds are enhanced in the surface normal direction. In the present study, by changing x-ray incidence angle and film thickness, we could separate the thermal vibrations of the surface in-plane and out-of-plane and bulk bonds separately, and discuss the bond character quantitatively. For further understanding of thermal vibrations, we have done classical Monte-Carlo calculations for the Cu film and revealed that the out-of-plane bond between the first and second layer is very weak.

I have also studied the surface chemical bonds on adsorbate-substrate systems.

Using simple pairwise potentials and the classical MD, the vibrational properties concerning the surface adsorbate-substrate bonds were reproduced well in the c(2×2)S and Cl/Ni(100) system. In both systems, the mean-square absolute displacements of the adsorbates are found to be noticeably greater in the normal direction than in the lateral ones. It is, on the contrary, revealed that concerning the adsorbate-substrate bonds the parallel motion of Cl-Ni1 pair in the Cl/Ni(100) system is as large as the vertical one, while the parallel motion of the S-Ni one is more suppressed in S/Ni(100). Such a difference is ascribed to the difference of the local surface geometries.

We have measured and analyzed temperature dependence of Cl *K*-edge SEXAFS spectra of the 0.12- and 0.50- ML Cl/Cu(100) states. The experimental results clearly demonstrate that the Cl-Cu bond is tightened with the Cl coverage, such a coverage dependence being opposite to that in the Cl/Ni(100) system. The different coverage dependence can be ascribed to the different Cl ionicity at the saturation coverage, which originates from the different roles of metal 3d bands.